Astrophysical Dynamics of Self-Gravitating Quantum Condensates

Yourong Frank Wang

A thesis submitted in fulfilment of the requirements for the degree of
Doctor of Philosophy in Physics,
The University of Auckland, December 2023.

Abstract

The nature of dark matter is an enigma for physics and astronomy. Ultra-light dark matter (ULDM) is an axion-like dark matter candidate whose tiny mass leads to an elegant resolution to a range of small-scale problems encountered by the standard cold dark matter (CDM) model, while reproducing large-scale results that agree with observations. ULDM is predicted to exist as a non-relativistic quantum matter described by the Schrödinger-Poisson equation (SPE).

Recent developments in cosmological simulation have provided powerful tools to model and constrain the properties and behaviours of dark matter, as epitomised by simulation software that constantly advance in scale, precision, and ease of access. My doctoral work contributed to such advancements for ULDM cosmology. I extend and test $\mathrm{PyUltraLight}$, a set of numerical pipelines that simulate the behaviour of ULDM. I further modified $\mathrm{AxioNyx}$, a state-of-the-art computational cosmology package for ULDM utilising adaptive mesh refinement (AMR) and hydrodynamical code for baryonic physics.

The nonlinear SPE system, alongside the Madelung formalism of quantum mechanics and SP solitons, is immensely interesting in its own right as an abstract mathematical system. This thesis provides an overview of the underlying theory and describes original investigations into dynamical friction from ULDM and multifield ULDM. It also outlines directions of future research. In the context of cosmological dark matter simulations, bridges to astronomically observable quantities are critical. This motivates simulations where ULDM interact with models of supermassive black holes (SMBHs), stars, and baryons.

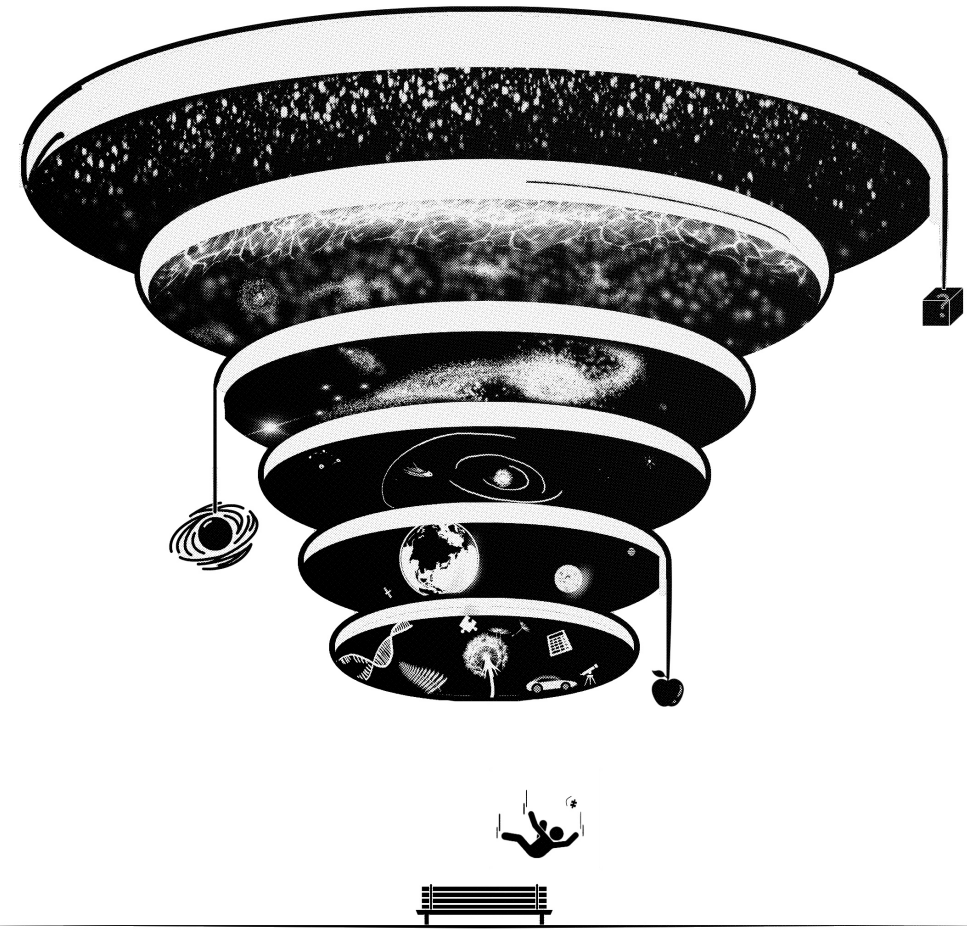

TO TIME:

stories before
and
adventures ahead

[●●◎○○○○○○○○○◎●●●●●●●]

Acknowledgements

Thank you for opening this document. You are witnessing the end of the beginning of a life dedicated to understanding and exploring nature. I too am eager to discover how far I can go.

My motivations for pursuing physics often puzzle me, almost as much as the questions of physics themselves. Over the past decade as a student in this field, I have sought to compile answers. While I do not think I have sufficient data yet, I firmly hold one truth: my heart harbours a profound unwillingness to shuffle off this mortal coil still ignorant – more ignorant – of the fundamental laws of nature, still unfamiliar – more unfamiliar – with the mechanisms supporting our world, and still distant – more distant – from the wonder that is our existence.

On this journey, I found a home at Auckland Cosmology, a vibrant and pragmatic group of researchers who sparked my passion for research and empowered me to turn existential dread into a strong drive for progress.

I am deeply grateful to my advisor, Professor Richard Easther, for his guidance and support. His office, and the hallway leading to it, have become an oasis of peace and encouragement.

I wish to thank Dr. Emily Kendall, Dr. Mateja Gosenca, Prof. Jens Niemeyer, Dr. Benedikt Eggemeier, Dr. Luna Zagorac, Dr. Peter Hayman, and Dr. Nathan Musoke for their invaluable discussions and patience.

I would also like to thank Dr. Mark Mueller for his lectures and mentorship, which fostered pride and focus in my research and creative projects.

My heartfelt appreciation goes to the other members of the research group, past and present. Your enthusiasm created a positive atmosphere that I cherish.

Many thanks to the support staff and lab organisers at the Auckland Advanced Physics Laboratory, where I taught for ten semesters. The error bars, the nuts and bolts, and the occasionally blown fuses all added a unique dimension to my time in the department.

To the scientists with whom I shared workspace, Caitlin, Craig, Gero, Jordan, Lerh-Feng, and Xiaoyu, thank you for making my time in the office productive and enjoyable.

My doctoral work began during the COVID-19 pandemic, through lockdowns and isolation. I am indebted to my friends, near and far, for their guidance, support, and camaraderie. Here is a subset in alphabetical order: Borong An, Imogen Bunting, Kevin Carley, Teresa Davenport, Abedennour Dib, Maxwell Finan-Jenkin, Samuel French, Doron Grossman-Naples, Jamie Gleave, Doug Goodman, Tim Guo, Caroline Jones, Tim Koorey, Katie Latimer, Miriam Leonhardt, Yinrui Liu, Sarah Marais, Sherkhan Mazari, Jacob Ngaha, Jane Orchard, Liam Quinn, Linus Richter, Nicholas Rui, Sophie Shamailov, Frank Shi, Youqi Song, Jerry Sun, Julie Taylor, Seán Thomson, Caleb Todd, Emma Tyson, Pei Wang, Anna Wolfenberger, Angela Xue, Xinyue Yu, Lanqing Yuan, Lauren Zhao, and Xianghan Zhu.

I am eternally grateful to my parents for their support. Thank you for raising me to be optimistic and upstanding; thank you for providing for my curiosity and (sometimes destructive) tinkering desires; thank you for putting a coat over my shoulders that Sunday night I spent too long looking through my new telescope instead of summoning me back to bed.

The computational aspects of this thesis were made possible by advances in computational physics and semiconductor technologies. I thank the authors and communities of the following open-source software: Python, Numpy, Matplotlib, Scipy, yt, Numba, Blender 3D, FFTW, and Chapel. My gratitude also goes to the developers of Space Engine, Celestia, and ESA Gaia Sky. Some simulations were run on resources provided by Australian Data Research Commons (ARDC) and New Zealand National eScience Infrastructure (NeSI).

The main body of the thesis is prepared with the Lato typeface designed by Łukasz Dziedzic. I additionally thank the Shandong Provincial Museum, whose Ming-Qing Dynasty pottery display inspired the colour palettes[1] used in parts of this thesis.

This section took its final shape during my relocation drive across New Zealand in April 2024, ahead of my oral defence. I thank my external examiners for their in-depth remarks and suggestions which aided immensely in the final revision of this thesis, and bridging it with my future work.

I dedicate this work to time: to the times past that shaped the Cosmos I grew up in, to the times ahead where people manipulate galactic materials like cement and communicate with gravitational waves, and to all the time in between.

We haven't met, and yet we have tried. Saycet, "We Walk Fast"

[1] Colour definitions may be found at `https://FWPhys.com/PhDC`.

Units and Conventions

We refer to “all that is or was or ever will be” (quote due to Carl Sagan) as the “Universe” or “Cosmos”, which includes ourselves, debating what to call it. In contrast, particular models of the Universe will be in lower case “universe” or “cosmos”.

Unless otherwise marked, we work in natural units where $\hbar = c = k_B = 1$. Further, we adopt the following conventions.

- The indices in various variables usually start counting from 0;
- Vectors in 3-dimensional space are denoted as $\mathbf{x} := [x, y, z]^T$;
- Vectors in 4-dimensional space-time are denoted as $x^\mu := [t, x, y, z]^T$, with metric signature $(-, +, +, +)$ where relevant;
- The Einstein summation convention is assumed for repeated indices occurring inside a term, $x_\mu y^\mu := \sum_{j=0}^{3} x_j y^j$;
- Simulation state vectors for the N body system, etc., where relevant, are denoted as $\bar{x} := [x_0, y_0, z_0, \dot{x}_0, \dot{y}_0, \dot{z}_0, ...]^T$;
- Fourier-transformed variables are distinguished by a hat, e.g. $\hat{\psi} := \mathcal{F}(\psi)$;
- The standard Numpy Fourier transform convention is adopted, where the normalising factors appear in the inverse Fourier transform;
- Where physical quantities are presented with units missing, they represent the internal code units as defined in Section 4.1.2.

Contents

日月安属？列星安陈？

What hierarchy do the sun and moon hold?

How are stars arranged?

Qu Yuan, *Tianwen (Heavenly Questions)*

1

Introduction

We find ourselves surrounded by a void of infinite, mysterious space. The story of cosmology is a story of efforts to understand this place. To some, progress in physics and astronomy instigated unappetising losses in the certainty of the future human condition. But curiosity and exploration have inspired wisdom far surpassing what were thought possible: wisdom to know the place we call home, and to cherish the wonders around us.

Humanity has not only charted the stars and galaxies in the night sky, but also found evidence for the existence of what we cannot see. Dark matter, dark energy, and certain relics of the early universe constitute what is sometimes referred to as the *Dark Side* of the universe.

1.1 The Golden Age of Cosmology

We emerged onto the Cosmic stage, opening our eyes beneath the night sky, during the golden age of the Universe, an almost ten-billion-year long period during which sufficient generations of stars have been born and extinguished to forge the heavy chemical elements that surround and constitute us. At the same time, the Universe is still not too old, with distant galaxy clusters, though eternally out of reach, remaining visible, enabling us to probe the large scale structures. Additionally, the cosmic microwave background (CMB) has not yet red-shifted into absolute obscurity. In 1964, its accidental first detection as an odd noise signal in Bell Lab's Holmdel Horn Antenna [5] was one of the sparks that ignited the field of modern cosmology.

On the human scale, the golden age of (observational) cosmology started in the early 1990s, marked by the launch of satellites such as the Cosmic Background Explorer (COBE, 1989 - 1994) and Hubble Space Telescope (HST, 1990 -). They dramatically increased our ability to reach far into space and back in time, and to test theories of the universe like never before. Missions such as the Wilkinson Microwave Anisotropy Probe (WMAP, 2001 - 2010) and Planck (2009 - 2013) made profound progress on constraining the properties of the early Universe and the origin of structures. In more recent times, the launch of the James Webb Space Telescope (JWST, 2021 -) and Euclid (2023 -) further extended our vision. These developments took place alongside the onset of gravitational-wave astronomy, through grand projects such as the Laser Interference Gravitational Waves Observatory (LIGO, 2015 -) and the European Advanced Virgo detector (2017 -).

In the standard framework of cosmology, the universe is regarded as homogeneous and isotropic at large scales. The geometry of spacetime can hence be captured by the the Friedmann-Lemaître-Robertson-Walker (FLRW) metric, which is used throughout this thesis,

$$\mathrm{d}s^2 = -c^2\mathrm{d}t^2 + a^2(t)\left(\frac{\mathrm{d}r^2}{1-Kr^2} + r^2\mathrm{d}\theta^2 + r^2\sin^2\theta\mathrm{d}\phi^2\right), \tag{1.1}$$

where $a(t)$ is the cosmic scale factor and $K \in \{0, \pm 1\}$ is linked to the overall curvature of the universe, discussed later. The scale factor can be used to determine the proper distance from the origin to a comoving object at radial coordinate r and time t,

$$d(r,t) = a(t)\int_0^r \frac{\mathrm{d}r'}{\sqrt{1-kr'^2}} \tag{1.2}$$

From Equation 1.2, it can be shown that the rate of change of the distance between any two comoving observers anywhere in such a universe is

$$\dot{d} = d\frac{\dot{a}(t)}{a(t)}, \tag{1.3}$$

where dots represent derivatives with respect to time. From this we define the Hubble Parameter,

$$H(t) \equiv \frac{\dot{a}(t)}{a(t)}, \tag{1.4}$$

and its current observed value is denoted as H_0.

Since $a(t)$ seems to always increase with time for our universe, it is sometimes more practical to work with the cosmic redshift, z. The redshift between times t_0 and t_1 is

$$z = \frac{a(t_0)}{a(t_1)} - 1. \tag{1.5}$$

By substituting the FLRW metric into the Einstein field equations,

$$G_{\mu\nu} + \Lambda g_{\mu\nu} = 8\pi T_{\mu\nu}, \tag{1.6}$$

we obtain the equation of motion for $a(t)$, or the Friedmann equations:

$$\left(\frac{\dot{a}}{a}\right)^2 + \frac{K}{a^2} = \frac{8\pi}{3}\rho \tag{1.7a}$$

$$\frac{3\ddot{a}}{a} = -4\pi(3p + \rho), \tag{1.7b}$$

where p and ρ are the pressure and density of the matter-energy contents. Some special equations of state are

$$p = \begin{cases} 0: & \text{Dust / Non-relativistic (Cold) Matter,} \\ \rho/3: & \text{Radiation / Relativistic (Hot) Matter,} \\ -\rho: & \text{Dark Energy.} \end{cases}$$

The critical density, ρ_{Crit}, is the density of matter required to halt the expansion of a matter only universe as $t \to +\infty$,

$$\rho_{\text{crit}} = \frac{3H_0^2}{8\pi}. \tag{1.8}$$

The comparison between the true mean matter density and ρ_{Crit} determines the spatial geometry of the universe.

1.2 The Dark Side of the Universe

To further set the stage, we briefly discuss what we know and do not know about dark matter, dark energy, and several forms of cosmic *horizons*. This thesis mainly focusses on the first topic, dark matter, while some references will be made to the latter two, which each play a unique and important role in the evolution of spacetime.

1.2.1 Dark Matter

The light-producing components of galaxies are participants in a complex environment dominated by dark matter halos. Overall, dark matter makes

up about 27% of the matter-energy content of the universe, 5 times more than all baryonic matter combined.

While many competing theories on the origin of dark matter exist within particle physics, the Cold Dark Matter (CDM) hypothesis is the most studied and simulated phenomological dark matter model to date. Chapter 2 features a discussion on this topic.

1.2.2 Dark Energy

The bulk motion of distant galaxies shows us that Cosmic expansion is not only continuing, but accelerating. This phenomenon implies the existence of an enigmatic component of our universe with negative pressure, often referred to as dark energy. It contributes about 70% of the matter-energy content of the universe.

A cosmological constant, denoted by Λ (Equation 1.6), is the most widely accepted representation of dark energy. The ΛCDM model is currently a baseline for cosmological studies. It has demonstrated remarkable alignment with observations across various aspects of the structure and behaviour of the Universe[1].

1.2.3 Cosmological Horizons

As we look farther out, we also rewind the Universe farther back in time. A "horizon" refers to a boundary or limit beyond which we cannot directly receive information.

[1]The value of H_0 has been successfully measured within the cosmic neighbourhood using Type-Ia supernovae using distances and redshifts. This method has no dependence on cosmological models, but the resulting value is currently at great odds with H_0 obtained from CMB measurements and the ΛCDM model. This difference, which is greater than 5σ, is known as the Hubble Tension [4].

Cosmological horizons are critical for the understanding the limitations of our observations and theories. It is thus helpful to define and distinguish the following kinds of horizons.

- **Particle Horizon** is the boundary of the observable universe, it is the farthest point from which light could have travelled to us within the current age of the universe.
- **Hubble Horizon,** or Hubble sphere, is the present distance at which objects seem to recede from us at the speed of light.
- **Optical Horizon** is as far as we are allowed to directly probe through electromagnetic means. It corresponds to the time the universe first cooled enough to permit the existence of neutral atoms. The light that shone through became the CMB that we observe today.

1.3 Outline of this Thesis

Chapter 2 begins with a review of the CDM paradigm and its challenges, motivating the ULDM model of dark matter. It then goes on to discuss the properties of ULDM, its possible origins, as well as some interesting ways to extend the model.

Chapter 3 touches on the relevant physical processes in galactic baryons and black holes that we consider in models that trace the evolution of ULDM. It serves as a review of the key concepts and results that our investigations utilise down the line.

Chapter 4 is a unified technical documentation on modelling ULDM-containing systems using the libraries $\mathrm{PyUltraLight}$ and $\mathrm{AxioNyx}$. It also features convergence and stability tests on our numerical routines.

Chapters 5 and 6 are primarily constructed using our published journal articles, where we discuss ULDM-containing systems across a range of distance and time scales, and provide prospects for astrophysical signatures with a potential for indirect ULDM detection.

Finally, discussions and potential future directions are presented in Chapter 7. We also talk about some of the assumptions made in previous chapters and future ways to relax them in order to explore bigger parameter spaces and model more complex systems.

1.4 Cosmological Parameters

Unless otherwise noted, we adopt the nominal values for the following constants from the Planck 2018 dataset [6].

Symbol	Meaning	Nominal Value
H_0	Hubble parameter	67.4 km/s/Mpc
Ω_{m0}	matter density parameter	0.315
ρ_{crit}	critical density	9×10^{-27} kg/m^3

Table 1.1: Planck 2018 Parameters used in this thesis

... in the presence of total Darkness, the mind finds it absolutely necessary to create light.

Isaac Asimov, *Nightfall*

2

Ultralight Axions as Dark Matter Candidate

First coined by Fritz Zwicky in 1933, the concept of dark matter developed with our understanding of the structure and evolution of galaxies, and our ability to measure properties of the Universe over larger and larger scales. This chapter introduces the quantitative language with which dark matter is described. In doing so, we offer a walk-through of some observational results that motivated the current models of dark matter.

2.1 The Case for Dark Matter

At the turn of the twentieth century, innovations in photography and spectrography gave researchers the first hints of a profound cosmic imbalance, that is, *what we see* cannot explain what we see – a lot of mass seems to be missing in the Universe, and the visible matter alone is insufficient to hold cosmic structures together.

In 1922, Jacobus Kapteyn proposed that any invisible matter in the Universe can be detected through its gravitational effects. In the 1930s, Fritz Zwicky found that galaxy clusters had dramatically more mass than suggested by their luminous material. Jan Oort reported similar anomalies in stellar motion within the Milky Way galactic plane. Since the 1970s, Vera Rubin and others used galaxy rotational curves, velocities plotted against their radial separation from galactic core, and published a widely accepted estimate of the extent of the missing mass problem – galaxy clusters contain about five times more mass than what we directly observe in stars and gas. A typical rotation curve from a later work for the galaxy Messier 33 is presented in Figure 2.1.

Around the new millennium, the Bullet Cluster (1E 0657-558) was discovered and studied by both the Hubble Space Telescope and the Chandra X-ray Observatory [8]. 1.14Gpc away from Earth, it is the aftermath of a collision between two galaxy clusters, during which their hot gas interacted to produce a shock wave similar to that produced by a bullet through an object. As Figure 2.2 shows, a smaller group of galaxies crashed through the larger one. Clowe et al. found that in this structure, the majority of the mass, as determined using weak gravitational lensing over the background,

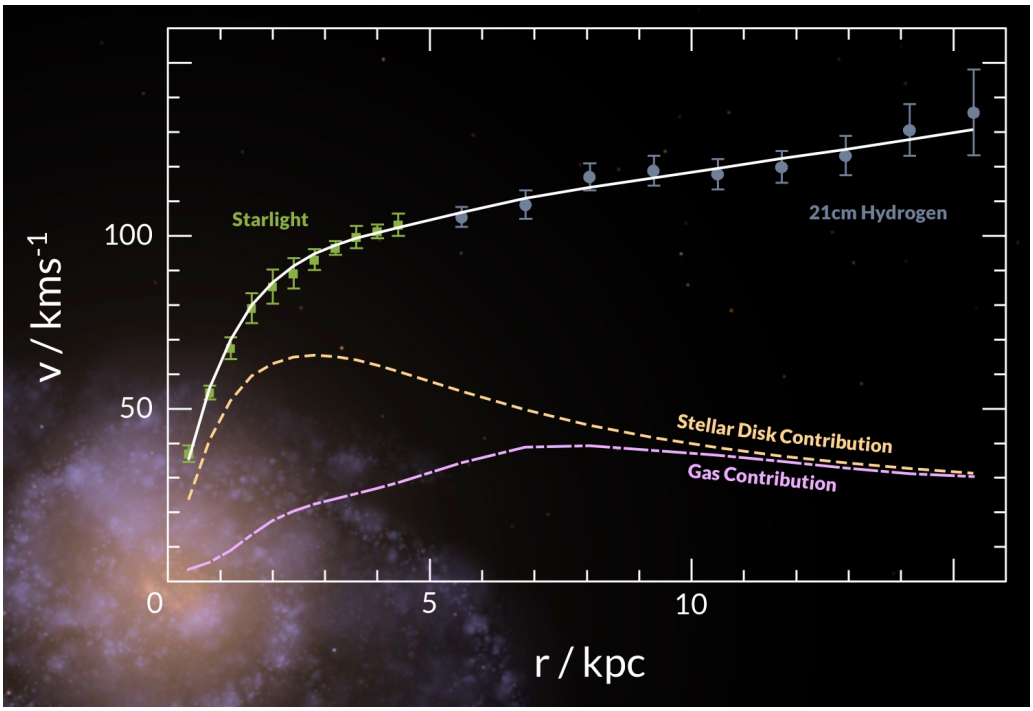

Figure 2.1: The rotation curve of M 33, adapted from [7], superimposed with a to-scale render of the galaxy using Celestia.

actually separated from the visible matter. This is seen as direct evidence for the existence of dark matter [9].

On the other hand, since the discovery of CMB, studies on the large scale features of the universe also suggests the existence of missing mass. Sky surveys showed that the distribution of galaxies resembles a "cosmic web", with filaments and sheets enclosing large void regions. From the 1980s, it has been demonstrated that such structures in the universe could not form with the gravitational contributions of visible matter alone [10].

Dark matter was proposed as a potential answer to these anomalous observations, that a lot of mass is inside galaxies which neither produces nor absorbs light. The field of dark matter is rife with creativity and ideas. Figure 2.3 lists some of the salient ideas in the field today, and some of dark matter's key properties are summarised on the next page.

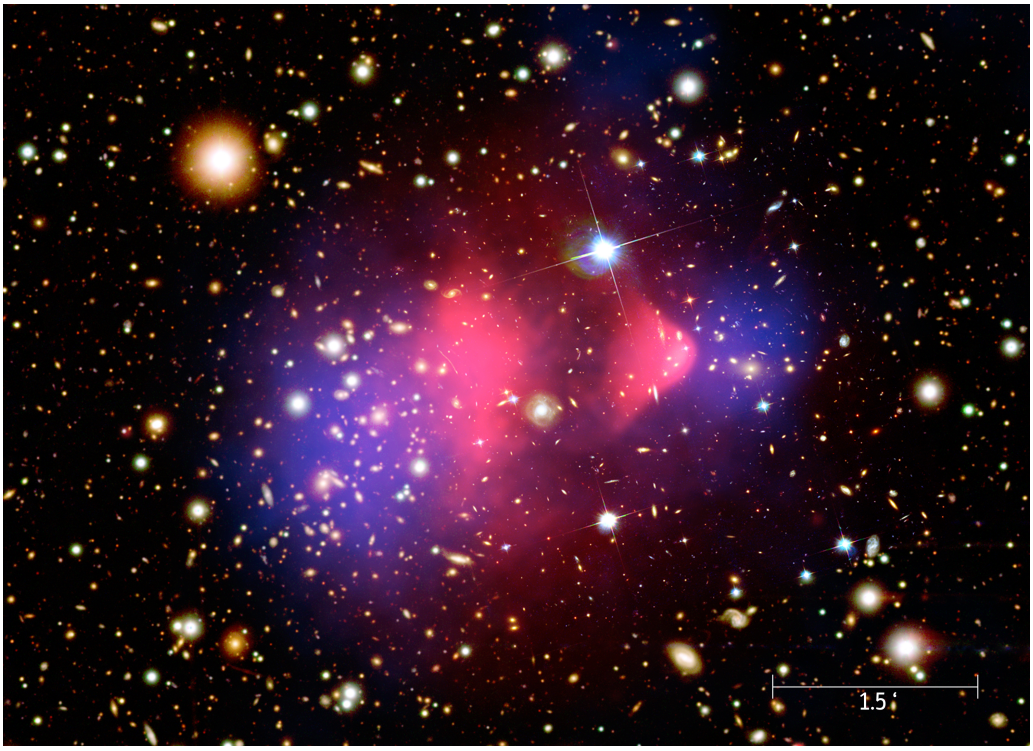

Figure 2.2: A composite photograph of the Bullet Cluster. The blue overlay shows the distribution of total mass, obtained via weak lensing, while the red overlay shows the concentration of hot gas, traced using their X-Ray emission. Image Credit: NASA.

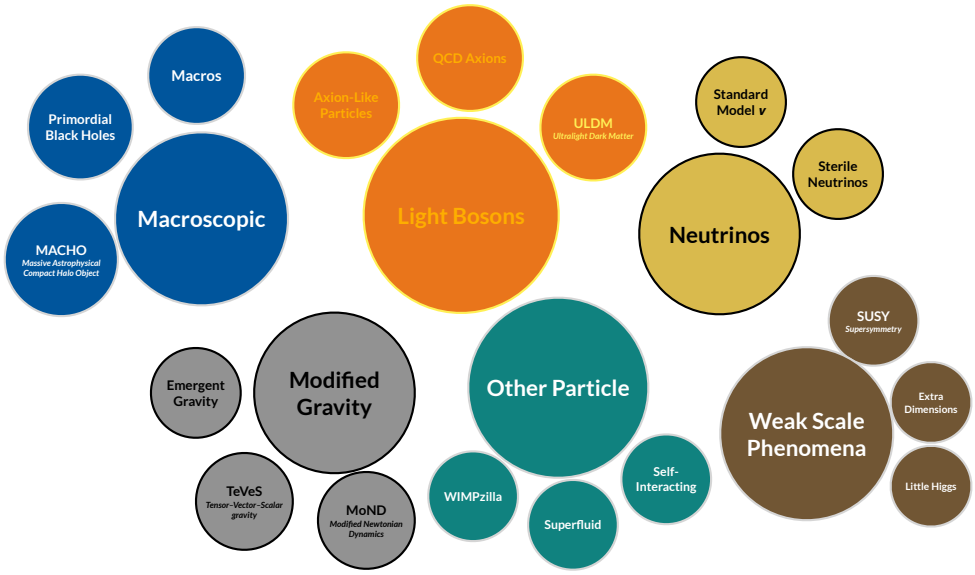

Figure 2.3: A mind-map of some theories in the general dark matter landscape, adapted from [11]

- **Dark:** Dark matter does not emit or absorb electromagnetic radiation like visible light. This not only means we cannot see it, but also points to the lack of means for dark matter to lose energy through thermal radiation, precluding its coagulation inside galactic planes.
- **Cold:** The particles that make up dark matter are expected to move non-relativistically so as to confine them inside galactic halos and not disrupt already formed structures. This distinguishes it from hot dark matter, which moves at relativistic speeds and cannot contribute to structure formation as well.
- **Stable:** The effects of dark matter on both the early Universe and galaxies today suggest that it has persisted over the history of the Universe. During this time, its fundamental properties, such as the mass and interaction strengths of the constituent particles, whatever they may be, have remained constant.

2.2 The ΛCDM Paradigm and its Challenges

The ΛCDM (Lambda-Cold Dark Matter) model combines two essential components: Lambda (Λ), the cosmological constant, and CDM, Cold Dark Matter. CDM is usually modelled as a collisionless ensemble of smooth particles that gravitate towards each other. We reproduce the relevant Friedmann equations,

$$H^2 = \frac{8\pi}{3}\rho - \frac{K}{a^2} + \frac{\Lambda}{3}, \tag{2.1a}$$

$$\dot{H} = -4\pi(\rho + 3p) + \Lambda. \tag{2.1b}$$

In this model, the Universe began in an almost uniform state, with tiny fluctuations. These fluctuations underwent gravitational collapse on the expanding spacetime background, and seeded all structures that we see in the sky. The ΛCDM model has been successful in explaining a wide range of cosmological observations, including characteristics of the CMB [12], to baryonic acoustic oscillations (BAO) in the early galaxies [13], and properties of the Lyman-α forest [14]. It provides a largely coherent framework for understanding the evolution of our Cosmos.

Cold Dark Matter obeys the collisionless Boltzmann Equation, also called the Vlasov equation [15]. In expanding space, it has the form

$$\frac{\partial f}{\partial t} + \frac{1}{ma^2}\mathbf{p}\cdot\boldsymbol{\nabla} f - m\boldsymbol{\nabla}\Phi\cdot\frac{\partial f}{\partial \mathbf{p}} = 0, \tag{2.2}$$

where $f(\mathbf{x}, \mathbf{p}, t)$ is the phase space distribution function, a is the cosmic scale factor, m stands for mass, $\mathbf{p}$ for momentum, and Φ the gravitational potential.

2.2.1 Small-Scale Challenges

Though CDM makes successful predictions that agree with observations across a range of cosmic features, it tends to work best on length scales above 10kpc or so, and may deviate from observed astrophysical reality on smaller scales. Key issues include:

No Direct Detection. There has been no direct detection of any dark matter particle in colliders or detectors, including those expressly built to look for dark matter particles.

Core-Cusp Problem. CDM, lacking any means to radiate excess energy away, is predicted to concentrate in galactic nuclei in a "cuspy", or divergent, density distribution, usually modelled as a Navarro-Frenk-White (hereafter NFW) profile [16],

$$\rho(r) = \rho_0 \frac{r_c}{r(1 + r/r_c)^2}, \tag{2.3}$$

where ρ_0 , the characteristic density, and r_c , the scale radius, vary from halo to halo. While this profile is in good agreement with observations of the outer regions of galaxies, observations also suggest that the central densities of galaxies should be cored, or flat [17]. These different density profiles are illustrated in Figure 2.4.

Satellite Plane Problem. The distributions of satellite galaxies around the Milky Way and Andromeda Galaxies seem have a bias away from the galactic disk, which is different from the prediction from ΛCDM that they should be uniformly distributed across the spherical dark matter halo.

Missing Satellite Problem. The CDM model predicts more small satellite galaxies around large Milky Way-like galaxies than observed.

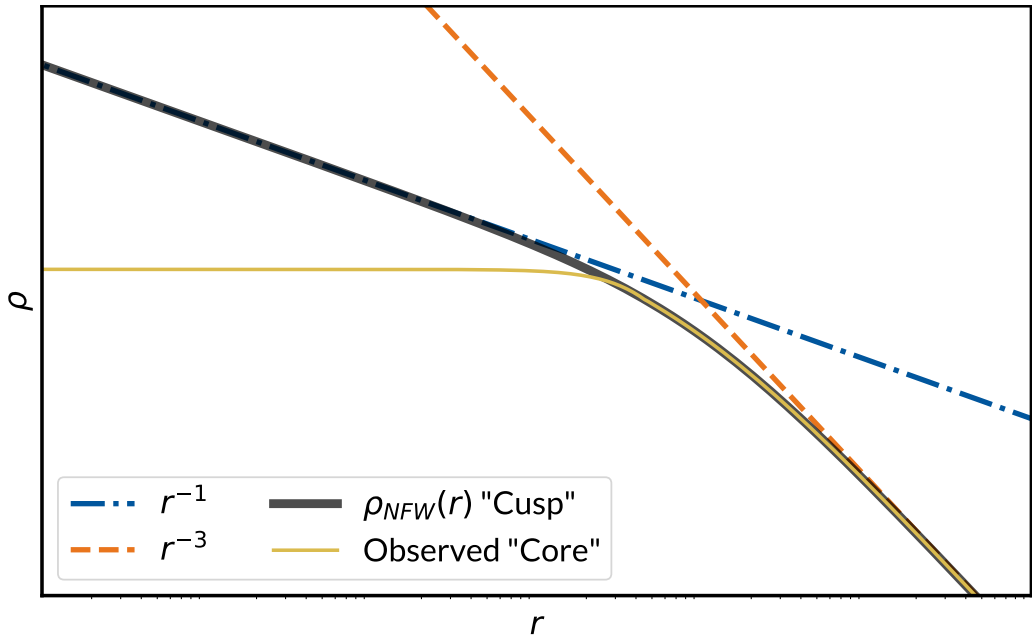

Figure 2.4: A log-log plot of the cuspy NFW and core density profiles. The parameter values were arbitrarily chosen for illustrative purposes.

Age of the First Galaxies: The current ΛCDM model favours formation times of the first large galaxies later than the high-redshift galaxies observed by JWST, such as the object GLASS-z12, which formed merely 350 million years after the Big Bang [18].

2.2.2 Alleviation of the Small-Scale Challenges

The challenges outlined above represent limitations in our knowledge, both observational and theoretical. It is possible that these inconsistencies will be resolved over time with better survey sensitivity, better modelling of baryonic physics or even the breakdown of Newtonian dynamics at galactic scales (MOND). Figure 2.5 serves as a summary of the various scales we have discussed, both where CDM has been successful and where CDM is less constrained and subject to challenges.

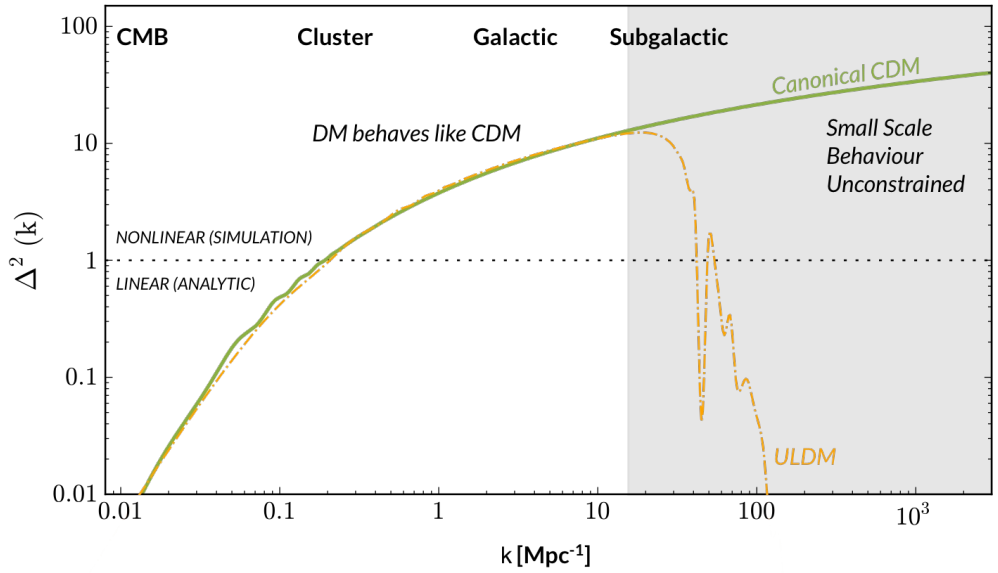

Figure 2.5: The power spectra of CDM [19] and ULDM in the current universe. The FDM curve was produced in AxionCamb [20] using the fiducial particle mass of 10^{-21} eV.

Another option is that the dark matter has more complicated small-scale dynamics than described by CDM – collisionless clumps – alone. To this end, Ultralight Dark Matter (ULDM) has become a widely-studied dark matter candidate, and we are finally ready to introduce it into the picture.

2.3 Ultralight Dark Matter

2.3.1 The Axion

The axion particle was first proposed as a solution to a problem in quantum chromodynamics (QCD), the theory of how quarks interact via gluons. The problem is called the strong CP (Charge-Parity) problem [21, 22]. If CP is conserved in a physical process, a left-hand positively charged particle should be treated no differently than the corresponding right-hand negatively charged antiparticle. Indeed, experimental observations have shown

that such a symmetry is remarkably well-conserved in strong nuclear interactions. Without an explicit mechanism to enforce this, it seems to be an instance of *fine-tuning*. As such, resolving the strong CP problem is crucial not only for the internal consistency of the Standard Model, but for understanding the dominance of matter over antimatter in the universe [23, 24].

By far the most famous solution to this problem is the Peccei-Quinn mechanism, named after Roberto Peccei and Helen Quinn. This mechanism introduces a new scalar field, called the axion, which dynamically adjusts to make the symmetry violations vanish, thereby preserving CP symmetry. We start with the minimal form of the action of a spinless, massless real scalar field,

$$S_\phi = \int \mathrm{d}^4x\sqrt{-g}\left(\frac{1}{2}g^{\mu\nu}\partial_\mu\phi\partial_\nu\phi\right). \tag{2.4}$$

This action permits the shift symmetry $\phi \rightarrow \phi + C$, where C is some constant that does not contribute to the Lagrangian. For very small (but nonzero) particle mass m, the symmetry becomes approximate. Spin-zero fields with nonzero mass arise in models with an additional potential function $V(\phi)$ that is periodic in ϕ. A natural example of such a potential is

$$S_\phi = \int \mathrm{d}^4x\sqrt{-g}\left(\frac{1}{2}g^{\mu\nu}\partial_\mu\phi\partial_\nu\phi - \mu^4\left(1-\cos\left(\frac{\phi}{F}\right)\right)\right), \tag{2.5}$$

where μ describes the coupling strength and F controls the shift symmetry (for example, $\phi \rightarrow \phi + 2\pi F$). The choices of the periodic potential in Equation 2.5 and the relevant interaction strengths can vary depending on the specific motivations. Scalar fields described by this simple action are collectively are known as “axion-like fields”, with the corresponding particles, of course, called “axion-like particles” (ALPs).

In general, any (pseudo)scalar particle whose dominant interaction is through gravity, it satisfies the Klein-Gordon equation,

$$-\Box\phi + m^2\phi = 0, \tag{2.6}$$

where $\Box\phi = \partial^\mu\partial_\mu\phi = g^{\mu\nu}\partial_\nu\partial_\mu\phi$ is the d'Alembertian, and m^2 is the leading term in the Taylor expansion of the full self-interaction potential as we will see in Section 2.3.3

2.3.2 Mass of the Ultralight Axion

The mass of the ultralight axion, m_{A}, shapes the cosmological effects of ULDM, and is consequently the main focus of observational tests and constraints. The most commonly considered values for the mass of the ULDM axion are between 10^{-21} and 10^{-22} eV. Some observational and theoretical bounds are presented in Figure 2.6. We also frequently make use of the short-hand m_{22},

$$m_{22} \equiv \frac{m_{\mathsf{A}}}{10^{-22}\mathsf{eV}}. \tag{2.7}$$

On the face of it, most of the parameter space is excluded. That said, many constraints rely on observations of a small number of systems, which are potentially atypical. Furthermore, these constraints apply to the case of a single, non-interacting axion field, but there are good reasons to relax both assumptions, producing much more leeway for the underlying hypothesis.

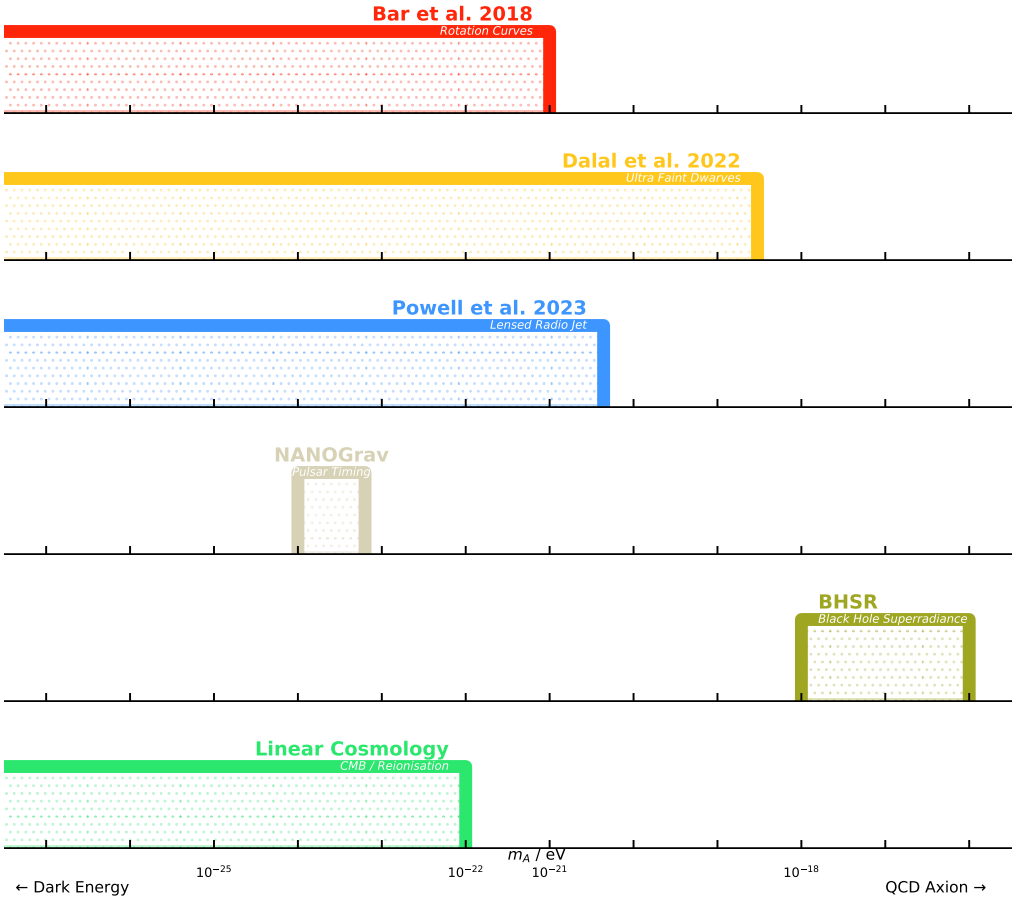

Figure 2.6: Some recent constraints on the ULDM axion mass. Shaded areas are excluded.

2.3.3 A Quantum Condensate

The astrophysical scenarios we discuss all involve sub-horizon scales and nonrelativistic bulk motion. Our regime of interest requires that F is large, and under this assumption we can transform the cosine term in Equation 2.5 into a purely quadratic minimum, around which our field oscillates,

$$S_\phi = \frac{1}{2}\int \mathrm{d}^4x\sqrt{-g}\left(g^{\mu\nu}\partial_\mu\phi\partial_\nu\phi - \frac{\mu^4}{F^2}\phi^2\right). \tag{2.8}$$

Varying this action yields an equation of motion of the field,

$$\frac{1}{\sqrt{-g}}\partial_\mu\left(\sqrt{-g}g^{\mu\nu}\partial_\nu\phi\right) = m_{\mathrm{A}}^2\phi, \tag{2.9}$$

where we have identified m_{A} with the quantity μ^4/F^2. Regarding the choice of $g^{\mu\nu}$, recall the FLRW metric, Equation 1.1. Our discussion at hand regarding non-relativistic dark matter permits the introduction of the Newtonian Gauge,

$$\mathrm{d}s^2 = -(1+2\Phi)\mathrm{d}t^2 + a^2(t)(1-2\Phi)\delta_{ab}dx^a dx^b. \tag{2.10}$$

Substituting this into Equation 2.9, we obtain, to leading order in Φ,

$$\ddot{\phi} - (1+4\Phi)\nabla^2\phi - 4\dot{\Phi}\dot{\phi} + (1+2\Phi)m_{\mathsf{A}}^2\psi = 0. \tag{2.11}$$

In doing so, we have assumed that the structures of interest have decoupled from the Hubble flow, and the overall expansion of the universe can be cancelled away. Further simplifications are made through a process reminiscent of the Wentzel - Kramers - Brillouin (WKB) approximation. We write down an ansatz,

$$\phi = \frac{1}{\sqrt{2}m_{\mathsf{A}}}\left(\psi e^{-im_{\mathsf{A}}t} + \psi^* e^{im_{\mathsf{A}}t}\right), \tag{2.12}$$

and we assume the field's dynamics on the timescale of the condensate oscillations can be safely ignored, i.e. $m \gg \left|\dot{\psi}/\psi\right|$. Now, we have

$$i\hbar\dot{\psi} = \left[-\frac{\hbar^2}{2m_{\mathsf{A}}}\nabla^2 + m_{\mathsf{A}}\Phi\right]\psi, \tag{2.13a}$$

$$\nabla^2\Phi = 4\pi G\rho. \tag{2.13b}$$

This describes a quantum wavefunction, ψ. We are also able to assign a "mass density" to the probability cloud resulting from ψ, namely,

$$\rho \equiv m_{\mathsf{A}}|\psi|^2 - \langle\rho\rangle, \tag{2.14}$$

where $\langle\rho\rangle$ is the mean density.

Equations 2.13a and 2.13b are referred to as the Schrödinger-Poisson equations (SPE), and are a non-linear modifications to the Schrödinger equation where the wavefunction itself sources a gravitational field. This

setup has also been used to model (in a phenomenological sense) other forms of collisionless fluid not motivated by the axion setup, such as in Refs [25, 26]. For completeness, the full version of Equation 2.13 with cosmic expansion, $a(t)$, restored is

$$i\hbar\partial_t\left(a^{3/2}\psi\right) = a^{3/2}\left[-\frac{1}{2m}\nabla^2 + m\Phi\right]\psi, \tag{2.15a}$$

$$\nabla^2\Phi = 4\pi a^2(m_{\mathsf{A}}|\psi|^2 - \langle\rho\rangle). \tag{2.15b}$$

In the Madelung picture of quantum mechanics, which we sometimes reference, the probability density of the wavefunction gives rise to a mass density, while the condensate's velocity field is the gradient of the phase,

$$\psi(\mathbf{r}) = \sqrt{\rho(\mathbf{r})}e^{i\theta}, \tag{2.16a}$$

$$\mathbf{v}(\mathbf{r}) = \boldsymbol{\nabla}\theta(\mathbf{r}). \tag{2.16b}$$

The minuscule mass of the ULDM axion means that its de Broglie wavelengths can often be on the order of kiloparsecs [27]:

$$\frac{\lambda_{\mathsf{dB}}}{2\pi} = \frac{1}{m_{\mathsf{A}}v} = 1.92\mathsf{kpc}\left(\frac{10^{-22}\mathsf{eV}}{m_{\mathsf{A}}}\right)\left(\frac{10\mathsf{kms}^{-1}}{v}\right). \tag{2.17}$$

Intuitively, this suppresses structure formation on smaller scales, and as we shall see soon, allows for core-like galaxy density profiles. The characteristics of ULDM are illustrated in Figure 2.7.

The Jeans length is the scale at which the gravitational stability of a system bifurcates. At lengths smaller than the Jeans length, structures are pressure-supported: a small perturbation from equilibrium will initiate oscillations; scales larger than the Jeans length are unstable: gravitational attraction is stronger than the supporting pressure so a small perturbation will trigger a collapse.

The Jeans length of canonical CDM is vanishing since it is pressureless. For ULDM, however, any attempt to localise a particle past a certain threshold will lead to an increase in the system's energy. This is what we mean when we say ULDM structures are "supported by the quantum uncertainty principle". An estimate of the Jeans scale for ULDM is given by [27]

$$\lambda_J \approx 55 \left(\frac{10^{-22}\text{eV}}{m_\text{A}} \right)^{1/2} \text{kpc}. \tag{2.18}$$

2.4 ULDM Solitons

ULDM solitons are the lowest-energy bound states of a ULDM system. They are generally assumed to be spherically symmetric. To obtain the radial density profile of a soliton, we start by making the time derivatives of ψ vanish,

$$\psi(\mathbf{x}, t) = e^{i\beta t} f(r), \tag{2.19a}$$

$$\Phi(\mathbf{x}, t) = \varphi(r) \tag{2.19b}$$

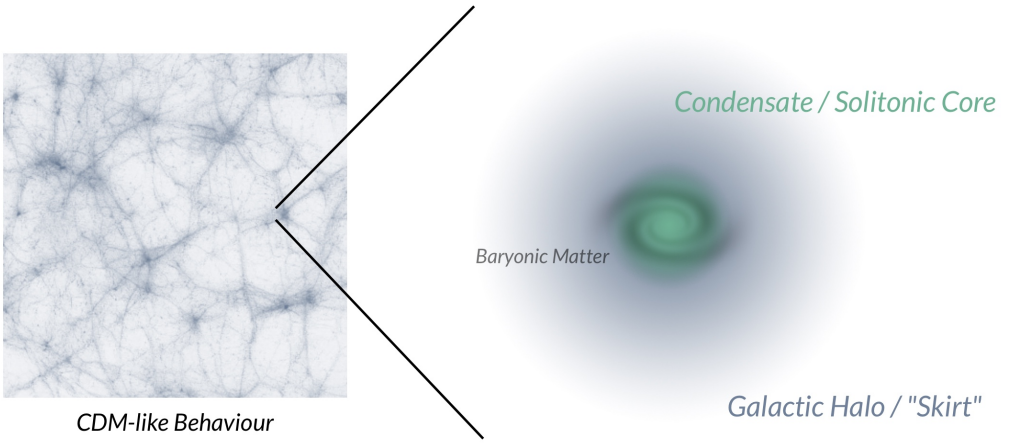

Figure 2.7: A qualitative sketch of the behaviour of ULDM across various scales

where $r = |\mathbf{x}|$. If we introduce $\tilde{\varphi} = \varphi + \beta$, Equations 2.13a and 2.13b reduce to

$$0 = -\frac{1}{2}f''(r) - \frac{1}{r}f'(r) + \tilde{\varphi}(r)f(r), \tag{2.20a}$$

$$0 = \tilde{\varphi}''(r) + \frac{2}{r}\tilde{\varphi}'(r) - 4\pi f(r)^2, \tag{2.20b}$$

where primes denote spatial derivatives.

A soliton is the ground state solution to the Schrödinger-Poisson equations, that is, the solution with no zero-crossings in $f(r)$. Solitons do not have a convenient analytic form, but it is possible to find numerical solutions that can be used to initialise a 3D configuration. The numerical profile for a soliton is shown in Figure 2.8.

We are further aided by a simple scaling relation: if $e^{i\beta t}f(r)$ is a solution to the SPE, then for an arbitrary real constant α,

$$\psi_\alpha(r,t) = \alpha e^{i\alpha\beta t} f(\sqrt{\alpha}r) \tag{2.21}$$

is a solution as well. For fixed axion particle mass m_{A}, it is useful to remember that if we double a soliton's mass, its central density will increase by a factor of $2^4 = 16$, while the core radius decreases by a factor of 2. This is illustrated in Figure 2.9.

For the "standard" soliton, where $f(0) = 1$, an empirical profile is sometimes employed [28],

$$f(r) \approx \left(\frac{1}{1 + 0.091\left(\frac{r}{r_c}\right)} \right)^8, \tag{2.22}$$

where r_c is a constant determined by a fit on the soliton profile above. In Chapter 4, we explore ways to impart solitons with phase and momentum.

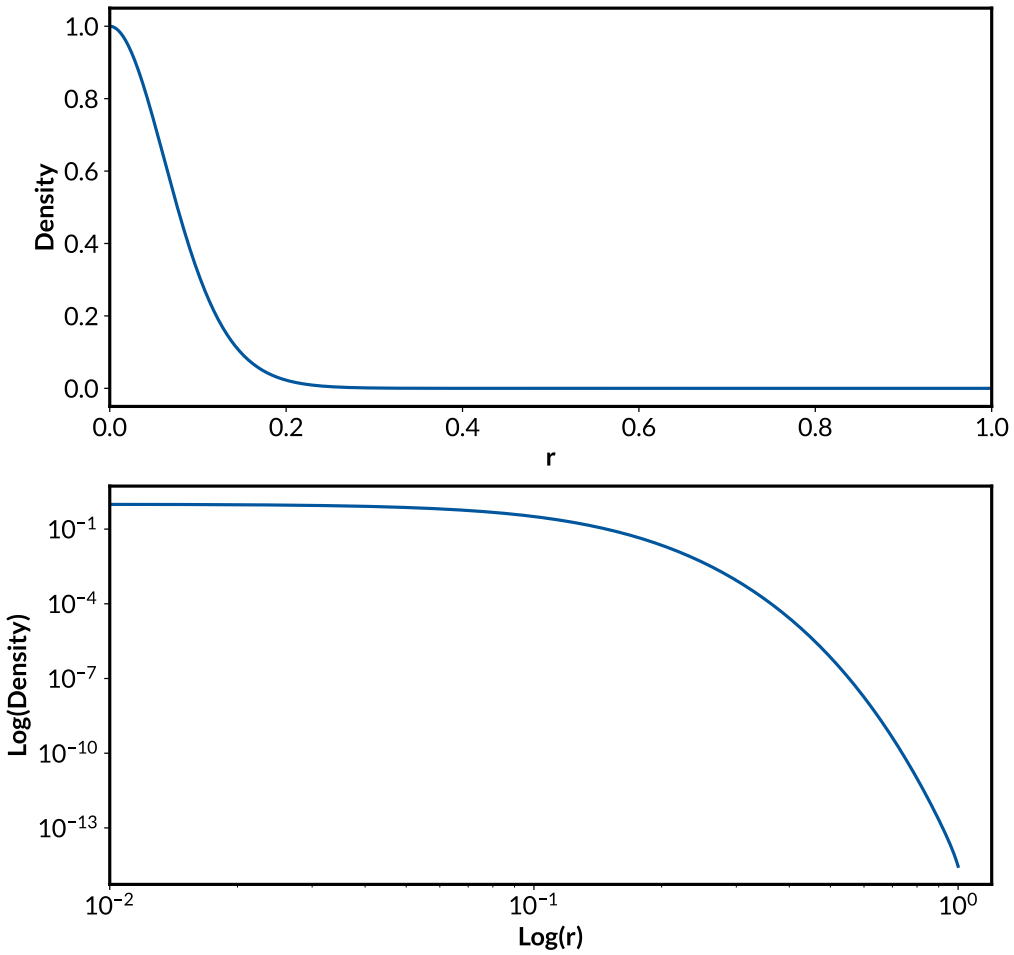

Figure 2.8: A numerically generated ULDM soliton profile. The axes are in arbitrary units.

2.4.1 Higher Order Eigenmodes

Scenarios where the ULDM soliton dominates the gravitational potential can make a perturbative treatment of the evolution worthwhile [29]. This is particularly relevant when there are other objects interacting with the soliton. An analogy to the hydrogen atom is sometimes drawn, where higher order eigenmodes are labelled by l, and m, analogues to the angular momentum and magnetic quantum numbers.

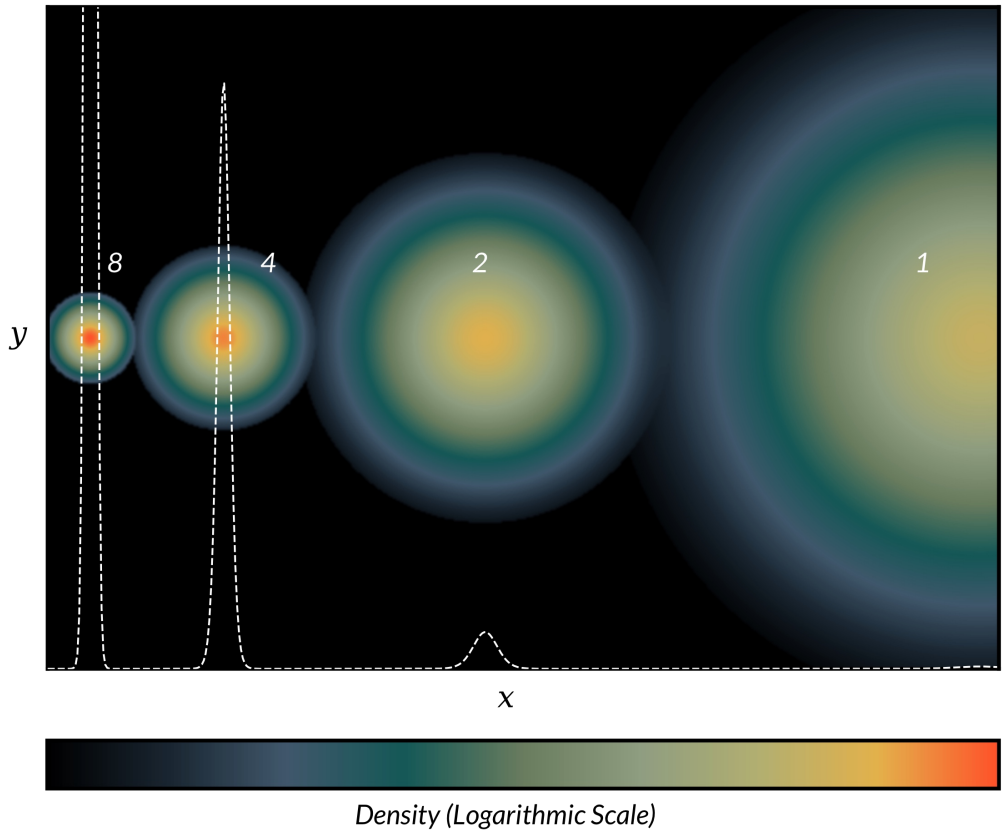

Figure 2.9: A density slice-plot of four ULDM solitons side by side, where the mass decreases by a factor of 2 from left to right

2.4.2 Core and Halo

In Figure 2.7 we have seen that ULDM halos consist of a spherically symmetric solitonic core and a "skirt" that roughly follows an NFW profile. It is of interest to investigate what fraction of ULDM mass reside in the core for a given halo and how this correlates with different halo masses. This is the so-called core-halo relation. Work by Schive et al. [30] established that the central soliton of a ULDM halo has a mass

$$M_{\text{Sol}} \propto a^{-1/2} M_{\text{Halo}}^{1/3}, \tag{2.23}$$

where a is the scale factor. With $a = 1$, the empirical relationship is

$$M_{\mathsf{Sol}} = 1.25 \times 10^9 M_\odot \left(\frac{M_{\mathsf{Halo}}}{10^{12} M_\odot} \right) \left(\frac{10^{-22}\mathsf{eV}}{m_{\mathsf{A}}} \right). \tag{2.24}$$

Other investigators have found different scaling relationships. For example, [31] investigates the core-halo relation through a dynamic approach. ULDM halos are dynamically formed through the merger of different solitons, and the authors argued that the different merger histories led to different scaling relationships.

2.5 ULDM Extensions

2.5.1 Self-Interacting Fuzzy Dark Matter (SIFDM)

The Ultralight Axion action invites higher order potential terms. This means there are natural ways to introduce non-gravitational self interactions in a collection of ULDM particles. The most common modification contains a quartic term. Depending this term's sign, the additional self-interaction can be attractive or repulsive.

Some of the phenomenology of the minimal model reflects in these self-interacting models too, such as wave interference. However, stability and granularity may be greatly altered in the presence of quartic self-interactions.

2.5.2 Multi-Field ULDM

As we have seen in Figure 2.6, m_{A}, the axion mass, is subject to myriad observational constraints that while weak, seem to rule out the entire region

of interest. One avenue out of this contentious situation is the possibility that ULDM doesn't exist as an isolated singlet, but a family of particles with different masses that have similar origin mechanisms. This so-called Multifield ULDM model significantly alters the resulting cosmological dynamics [32]. Our contributions to this idea will be discussed in Chapter 6

The multifield picture reduces the granularity in a dark matter halo which in turn weakens several key observational constraints that are sensitive to the amplitudes of granules around the soliton, e.g. the heating of stellar orbits in ultrafaint dwarf galaxies.

Separately, there is a strong analogy between ULDM dynamics and the physics of the inflaton condensate in the very early universe [33, 34, 35, 36] and the dynamics of N-field ULDM may be mirrored in the primordial universe if the cosmic inflation itself was driven by multiple fields [37, 38, 39].

如果说那个原始人对宇宙的几分钟凝视是看到了一颗宝石，其后你们所谓的整个人类文明，不过是弯腰去拾它罢了。

If we're to say that the caveman saw a gem in his brief gaze into the night sky, your entire civilisation thereafter is merely the stooping to pick it up.

Liu Cixin, *Zhao Wen Dao (Morning, Truth)*

3

Exploring the Physics of Galaxies

An idea attributed to Martin Rees is that cosmology resembles two very different sports, depending on the epoch. The physics of the very early universe is abstract yet logical, reminiscent of a game of chess; the moment neutral atoms formed and baryonic physics began, with its myriad messy complications, things became more akin to mud wrestling.

We now look into a selection of baryonic physics processes, features of the observable components of the Universe. Just as the distribution of galaxies themselves in a CDM / ULDM universe is correlated with local dark matter overdensities, many components and phenomena within galaxies can trace or constrain the properties of dark matter. The review presented

in this chapter constitutes a short glimpse at a few key aspects that directly inform our modelling effort, as discussed in the later chapters.

3.1 Dynamical Friction and Orbital Decays

As a massive object travels through a diffuse interstellar medium it injects some of its momentum and energy into the surrounding matter. This is called dynamical friction. It is not a contact force like the friction or drag that we experience on earth: the overdense "wake" a moving object induces gives rise to a net gravitational drag on the object opposed to its direction of motion. This was first systematically studied by Chandrasekhar [40]. The full expression is an integral over the phase space density of the field of matter,

$$\frac{\mathrm{d}\mathbf{v}_M}{\mathrm{d}t} = -16\pi^2(\ln\Lambda)m(M+m)\frac{1}{v_M^3}\int_0^{v_M}\mathrm{d}v v^2 f(v)\mathbf{v}_M, \tag{3.1}$$

where M is the mass of the object entering the medium, $m \ll M$ is the mass of each star in the stellar distribution, v_M is the velocity of the travelling heavy object in the reference frame where the centre of gravity of the matter field is initially at rest, $\ln(\Lambda)$ is called the Coulomb logarithm, and $f(v)$ is the number density distribution of the stars. Chapter 5 contains explicit evaluations of some of these parameters for an initially uniform ULDM background, and the reader is referred to [41] and [42] for more general discussions.

The strength of dynamical friction depends on the incoming object's mass and the medium's density, as well as the object's speed. For an initially uniform patch of ULDM, the speed dependence is sketched in Figure 3.1. If the massive object enters slowly (top panel), the gravitational wake generated will be roughly symmetric around it, providing little net drag. If

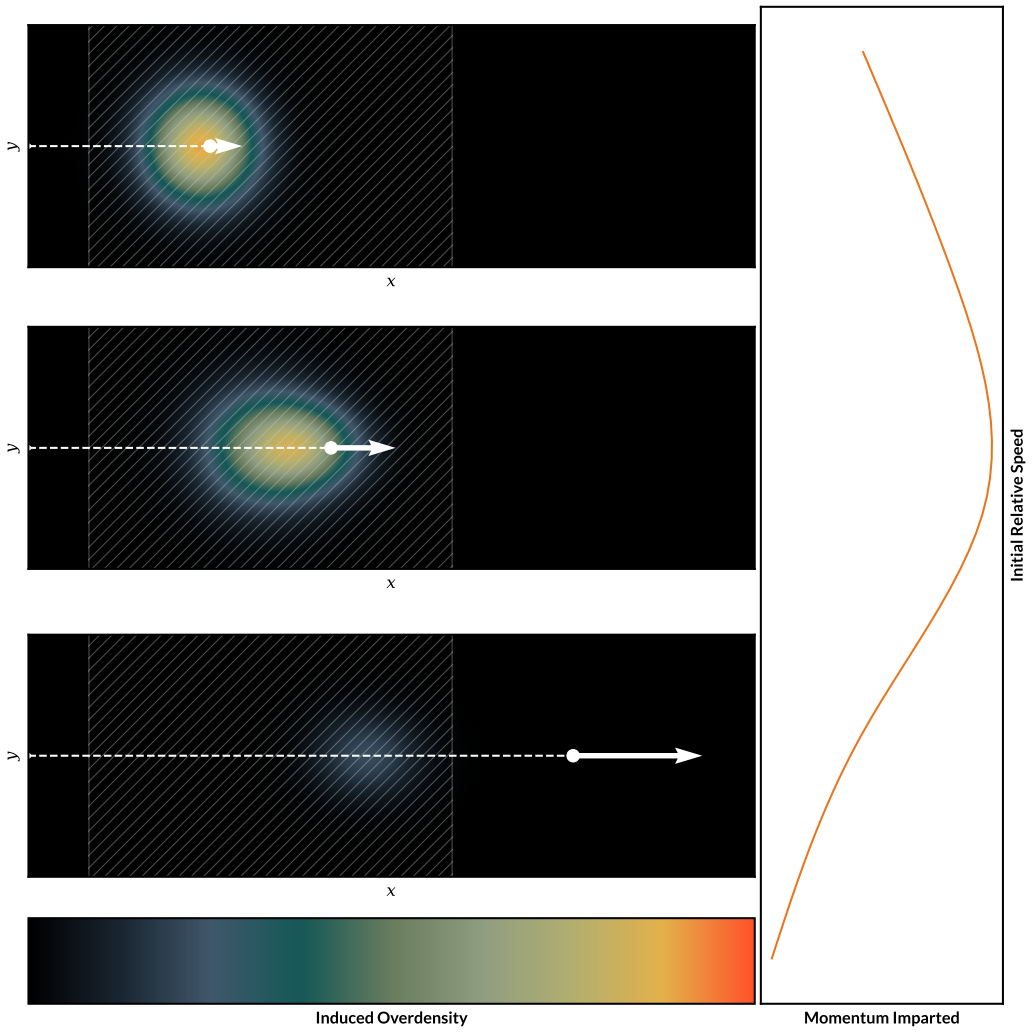

Figure 3.1: A sketch of the dependence of dynamical friction on velocity in ULDM. A massive object enters a uniform volume of interstellar medium (shaded region) at three different speeds.

the object traverses too quickly (bottom panel), the background doesn't have enough time to react, producing a small drag as well. Consequently, there is a middle ground where the drag is maximised.

Dynamical friction can manifest across a range of astrophysical scales, from a single neutron star travelling through a star cluster or dark matter waves [43, 44], to the bulk motion of clusters themselves around their host galaxies.

Globular clusters, consisting of approximately 10^4 to 10^7 stars, are densely packed and gravitationally bound stellar systems orbiting in stable formations. Conversely, a dwarf spheroidal galaxy, visually resembling a larger globular cluster, contains a significantly higher proportion of dark matter compared to the former.

As a globular cluster orbits its host galaxy, dynamical friction exerts a torque that reduces its radial separation from the centre. In a simplistic view, by looking at the radial separation of the smaller globular clusters from the centre of their host galaxies, and comparing this with the galaxy's estimated age, a rough estimate can be made about their rate of orbital migrations, and, in extension, the strength of dynamical friction – due to stars, interstellar gas, and dark matter [45].

3.2 Black Holes

Physical processes that take place around a black hole, especially a supermassive black hole (SMBH) which has a mass at least 10^5 times the mass of the Sun, are some of the most extreme in the known universe [46]. Here we outline two processes of potential interest to our investigations in ULDM cosmology: accretion and superradiance. In addition, we discuss the Final Parsec Problem of black hole mergers, which in part motivated the modelling efforts in this thesis.

Furthermore, because relativistic effects become relevant near the edge of a black hole, we revert to the full Klein-Gordon description of ULDM where necessary.

3.2.1 Black Hole Accretion of a Scalar Field

Black holes can absorb both mass and angular momentum from the medium around them, and ULDM is no exception. The study of Klein-Gordon systems around a black hole can be traced as far as the 1970s, where Unruh [47] provided a way to estimate the accretion rate, the number of particles that cross the event horizon compared to the overall particle flux. In more recent times, the stationary accretion flow around a black hole are studied by Clough et al. [48], Hui et al. [49], and Bamber et al. [50]. The reader is referred to the review by Hui [51] for a detailed analysis. In the parameter space relevant to us, where the mass of each individual dark matter particle is vanishing, the black hole accretion rate is estimated to be

$$\frac{\mathrm{d}M_{\mathsf{BH}}}{\mathrm{d}t} \approx 4 \times 10^{-9} M_{\odot} \mathsf{yr}^{-1} \left(\frac{M_{\mathsf{BH}}}{10^{9} M_{\odot}}\right)^{2} \left(\frac{\rho_{\mathsf{Halo}}}{0.1 M_{\odot} \mathsf{pc}^{-3}}\right), \tag{3.2}$$

where M_{BH} is the black hole mass and ρ_{Halo} refers to the ambient dark matter density. The rate is small, as ultralight axions, semiclassically speaking, readily tunnel across the potential barrier around a black hole, and our simulations reported in this thesis do not consider accretion effects.

A related problem was considered in 2018 by Avilez et al [52]. They looked at the process of black hole formation straight from a ULDM halo collapse process.

3.2.2 Rotating Black Holes and Superradiance

Superradiance is a feature of many dissipitive systems, from lab-based quantum optics to black hole astrophysics. In our context, it refers to the amplification of a ULDM axion particle's energy as it encounters a spinning black hole, where it "borrows" energy from within the event horizon [53].

Black-hole superradiance (BHSR) is closely linked to the Penrose process, tidal forces, and even Hawking radiation, which can be seen as a quantum version of BHSR. The review by Stott and Marsh [54] provides a detailed exploration of the subject.

The spacetime around a rotating black hole without electric charge is described by the Kerr solution. Using the standard Boyer-Lindquist coordinates, it takes the form

$$\begin{aligned} \mathrm{d}s^2 = &- \left(1 - \frac{2M_{\mathsf{BH}} r}{\Sigma}\right) \mathrm{d}t^2 + \frac{\Sigma}{\Delta}\mathrm{d}r^2 + \Sigma \mathrm{d}\theta^2 \\ &+ \left(r^2 + a^2 + \frac{2M_{\mathsf{BH}} r \eta^2}{\Sigma} \sin^2\theta\right) \sin^2\theta \, \mathrm{d}\phi^2 - \frac{4M_{\mathsf{BH}} r \eta \sin^2\theta}{\Sigma} \, \mathrm{d}t \, \mathrm{d}\phi, \end{aligned} \tag{3.3}$$

where, for brevity, variables related to the black hole's angular momentum J are introduced:

$$\eta = \frac{J}{M} \tag{3.4a}$$

$$\Sigma = r^2 + \eta^2 \cos^2\theta \tag{3.4b}$$

$$\Delta = r^2 - 2M_{\mathsf{BH}} r + \eta^2. \tag{3.4c}$$

It prescribes the existence of a region known as the ergosphere, where spacetime is dragged along the rotating black hole and must rotate with the black hole [55].

The analysis of black hole superradiance comes down to solving the Klein-Gordon equation in the Kerr background subject to the infalling boundary condition at the event horizon and the asymptotically vanishing boundary condition far away.

A cloud of particles surrounding the spinning black hole will have modes that extract energy and angular momentum from the black hole, making

these properties time-dependent, opening them to dynamical stability analysis. This was explored in the paper by Ficarra et al. in 2019 [56].

BHSR provides a powerful bound on m_{A} because the stability of superradiance modes are linked closely to the mass and composition of fields around the black holes. The excluded ranges [54] are

$$7 \times 10^{-14}\mathsf{eV} < m_{\mathsf{A}} < 2 \times 10^{-11}\mathsf{eV},$$
$$7 \times 10^{-20}\mathsf{eV} < m_{\mathsf{A}} < 1 \times 10^{-16}\mathsf{eV}.$$

Furthermore, a model with multiple axions is excluded if just one component species lies in these ranges.

3.2.3 The Final Parsec Problem

The time gap between when two galaxies merge and their central black holes merge is very hard to fit into the age of the universe. Once two black holes are already very close, the binary system does lose energy and orbital separation via gravitational wave radiation; when two black holes are far apart, they can lose angular momentum through dynamical friction. However, this effect weakens as the black holes get closer – there is less chance for a close encounter with another star in a smaller orbit. However, binary SMBH systems are apparently rare so the mergers must have somehow taken place. This is known as the “final parsec problem”.

For ULDM cosmology, Hui et al. [57], Bar-Or et al. [58], and Lancaster et al. [45] considered the effects of ULDM on inspiraling black hole binaries, and provided characteristic timescales of their orbital decay. The prospect that ULDM can bring SMBH binaries together is a main focus of our current and future modelling efforts.

3.3 Baryonic Systems

This section outlines the considerations arising from simulations of baryonic physics, following the paper by Almgren et al. [59]. Here, we emphasise the parameters available to us for each aspect of baryonic physics.

3.3.1 Basic Gas Dynamics

We take a mixture of hydrogen and helium that follows a γ-law equation of state, with γ being the usual specific heat ratio,

$$p = (\gamma - 1)\rho\, e, \tag{3.5}$$

where p is the (comoving) pressure, ρ the (comoving) density, and e stands for the internal energy. We first write down the continuity equation

$$a\frac{\partial \rho_b}{\partial t} = -\boldsymbol{\nabla} \cdot (\rho_b U), \tag{3.6}$$

where ρ_b is the comoving baryon density. This enables us to write the momentum equation as

$$\frac{\partial a \rho_b U}{\partial t} = -\boldsymbol{\nabla} \cdot (\rho_b U U) - \boldsymbol{\nabla} p - \rho_b \boldsymbol{\nabla} \Phi, \tag{3.7}$$

where Φ is the gravitational potential. A simulated gas system's internal e and total energies $E = e + U^2/2$ are separately evaluated.

Assuming they are well-approximated as monoatomic ideal gases, $\gamma = 5/3$, we have

$$\frac{\partial a^2 \rho_b e}{\partial t} = -a\boldsymbol{\nabla} \cdot (\rho_b U E + pU) - a(\rho_b U \cdot \boldsymbol{\nabla}\Phi - \Lambda_{HC}) \tag{3.8a}$$

$$\frac{\partial a^2 \rho_b E}{\partial t} = -a\boldsymbol{\nabla} \cdot (\rho_b U e) - ap\boldsymbol{\nabla} \cdot U + a\Lambda_{HC}, \tag{3.8b}$$

where Λ_{HC} are additional terms that account for heating and cooling effects. And of course, the gravitational potential, Φ, is solved using the Poisson equation from the total density,

$$a\boldsymbol{\nabla}^2\Phi = 4\pi(\rho - \langle\rho\rangle), \tag{3.9}$$

where $\langle\rho\rangle$ is the simulation domain's average density accounting for everything – baryons, dark matter, and stars. $\mathrm{AxioNyx}$ is then capable of advancing this equation in time, subject to a set of well-laid initial conditions.

3.3.2 Star Formation and Feedback

When dense regions of gas clouds in interstellar space undergo further collapse, stars are ignited. Star formation is an epitome of the "mud wrestling" side of cosmology, full of delayed responses to nonlinear physics that morph into at best statistical characterisations. It is a fascinating aspect of the Universe to model and consider, since we are currently orbiting one star and our bodies are comprised of fragments of others.

Stars alter the environment around them through a series of mechanisms collectively referred to as feedback, which regulates star formation rates within galaxies. Near the centre of an active galactic nucleus or a region with many supernovae, for example, the vast amount of energy released impacts the interstellar medium, which in turn changes the rate at which new stars form.

Code that accounts for star formation and evolution is absent from the work reported in this thesis, but it is the logical next step. It is sometimes argued that a better understanding of stellar formation and feedback mechanisms may bring a resolution to both the core-cusp problem and the final parsec problem (in that the stellar distribution of a galaxy post-merger are

different) without requiring exotic physics. This adds to the necessity for future cosmological models to account for it.

3.3.3 Stellar Velocity Dispersion

The stellar velocity dispersion of a galaxy, often denoted $\sigma(r)$, is the variance in line-of-sight velocity of stars. It is seen as a powerful predictor of many galactic properties, and modern observational techniques have made data widely available.

As we have established, ULDM halos have granular structures on scales similar to the de Broglie length of the underlying field. Orbiting stars are perturbed as they interact with the gravitational potential of these structures, heating them relative to their motion in a smooth background.

The purpose of computing is insight, not numbers.

Richard Hamming, *Numerical Methods for Scientists and Engineers*

4

Aspects of ULDM Simulation

We now review several numerical routines used to evolve an astrophysical system containing ULDM. We also outline ways to calculate derived quantities as simulations take place, and discuss their potential errors or limitations. This thesis makes use of the computational frameworks provided by PyUltraLight [60] and AxioNyx [61], and involves significant modifications to both. We primarily focus on the former, as we spent the more effort extending and testing this program.

4.1 Advancing the SPE in Time

To the lowest order, one can realise the signature "fuzzy" ULDM behaviours as a perturbative term on top of existing simulation code for cold dark matter cosmology, which is often implemented as a collisionless N body system [62][1]. This is valid because ULDM, by construction, should behave like CDM on large scales. If more robustness is desired, the so-called "quantum-pressure" associated with ULDM can also be added to sophisticated computational fluid dynamics (CFD) simulators [63].

The gold standard, however, is a purpose-built solver that deals with the non-linearity of the Schrödinger-Poisson Equations (SPE) directly, either via finite differencing or pseudo-spectral methods. The finite difference (FD) method is straight-forward to implement and insensitive to boundary conditions. However, as we will see, it is subject to stringent constraints on timestep sizes. The pseudo-spectral (PS) method advances the nonlinear SPE by manipulating the frequency components in a Fourier transformed version of the wavefunction.

The pseudo-spectral method works as follows. For a domain of edge length L and resolution N, the root grid is the set of points

$$\mathbf{x} = -\frac{L}{2}\begin{bmatrix}1\\1\\1\end{bmatrix} + \frac{L}{N}\begin{bmatrix}n_x\\n_y\\n_z\end{bmatrix}, \tag{4.1}$$

where n_x, n_y, and n_z are integers between 0 and $N-1$, and we denote the tuple of indices as $j := (n_x, n_y, n_z)$. To advance Equations 2.13a and 2.13b, we approximate the unitary time evolution of the quantum field using the

[1] Not to be confused with the massive particle ensembles we shall discuss later.

symmetrised split-step Fourier method. With the operations applied from right to left, we can write it as follows:

$$\psi(t+\Delta t) = \exp\left[-\frac{i\Delta t}{2}\Phi(t+\Delta t)\right]\times \\ \mathcal{F}^{-1}\left\{\exp\left[\frac{-i\Delta t k^2}{2}\right]\mathcal{F}\exp\left[-\frac{i\Delta t}{2}\Phi(t)\right]\right\}\psi(t). \tag{4.2}$$

$\mathcal{F}$ ($\mathcal{F}^{-1}$) denotes the (inverse) discrete Fourier transform on the root grid. The ULDM gravitational potential is obtained by solving Poisson equation in the frequency domain,

$$\Phi_{\mathsf{U}}(t+\Delta t) = 4\pi\mathcal{F}^{-1}\left\{\left(-\frac{1}{k^2}\right)\mathcal{F}\left(\psi^*(t)\psi(t)\right)\right\}. \tag{4.3}$$

This method is correct to second order in time [60]. The resolution of the root grid limits our ability to resolve the evolution of our simulated ULDM, and a simulated condensate can deviate significantly from physical reality under conditions that strain the numerical simplifications or our theoretical assumptions, and it is important to be cognisant of such limitations, especially how they scale with resolution and the size of our domain.

4.1.1 Spatial and Temporal Resolution

We recall from Chapter 2 that ULDM velocity is manifest as the gradient in the phase of ψ. Consequently, if the phases between two neighbouring cells differ by than π radians, structures will appear to move in the wrong direction. In the language of Fourier analysis, this is *aliasing* – when signals are time-limited, and not band-limited. This is illustrated schematically in Figure 4.1.

By default, the integration step length, Δt, is chosen using the Courant-Friedrichs-Lewy (CFL) condition, such that an object with the highest speed

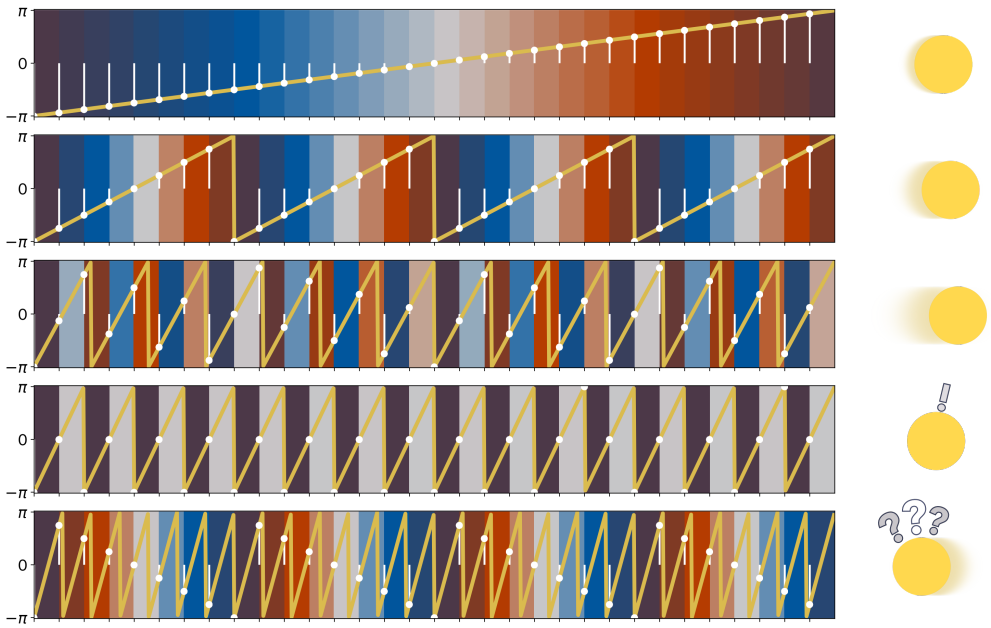

Figure 4.1: The grid-based nature of our simulations imposes an effective speed limit, above which motion is interpreted incorrectly. In this 1D example, the real x-velocity (gradient of the yellow lines) increases from the top panel to the bottom panel, while the simulated velocity based on the values on the grid (white dots), reaches a maximum value and then turns the wrong way.

resolvable by the grid travels exactly one grid interval during one time step [64],

$$\Delta t = \frac{L^2}{\pi N^2}. \tag{4.4}$$

The CFL condition is a qualitative requirement, since the Schrödinger-Poisson equation is not hyperbolic, but it provides a useful baseline[2]. For our practical use, except for simulations where the time-step lengths are determined by N body or hydrodynamical constraints, as discussed in Chapter 5, the main performance bottleneck is the three-dimensional Fourier transforms that advance the wavefunction over the base grid.

PyUltraLight accepts any positive even integer as grid resolution and automatically chooses the next "fast" one, where necessary, as evaluated by

[2] In a hyperbolic system, such a condition on the timesteps enforces causality.

the function `scipy.fft.next_fast_len()`[3]. In this thesis, we favour the following resolutions: 64^3, 128^3, 192^3, 256^3, 384^3, 512^3, and 1024^3. The complexity involved in each FFT operation is at least $\mathcal{O}(3N^3 \log N)$. For example, if we increase the mesh resolution by a power of two, from 128^3 to 256^3, the simulation requires $2^2 = 4$ times the number of steps to complete, with each step costing as much as $2^3 = 8$ more memory and disk space, in addition to taking about 9 times longer for each step. The number of steps and simulation time lengths for a simple ULDM simulation on the author's personal Mac Studio computer[4] is presented in Figure 4.2.

The performance figures illustrate that simulations achieve optimal results when utilising a large box and high spatial resolution. However, it is important to note that this approach can rapidly escalate in cost. This N^5 dependence on resources[5] motivates the use of SPE solvers with adaptive mesh refinement to resolve finer structures in larger-scale simulations, which we attempt with $\mathrm{AxioNyx}$.

[3]The FFT algorithms are fast because they employ a recursive divide and conquer strategy. Signal lengths with with small prime factors should be used.

[4]This machine has 8 high-performance CPU "P-cores" at a base clock speed of 3.2GHz, and 64 gigabytes of RAM. $\mathrm{PyUltraLight}$ is mainly designed to facilitate intermediate exploration of ULDM dynamics, whereas $\mathrm{AxioNyx}$ focuses on large-scale computation.

[5]Note additionally that, in practice, the scaling will be exacerbated by delays due to initialisation and I/O operations.

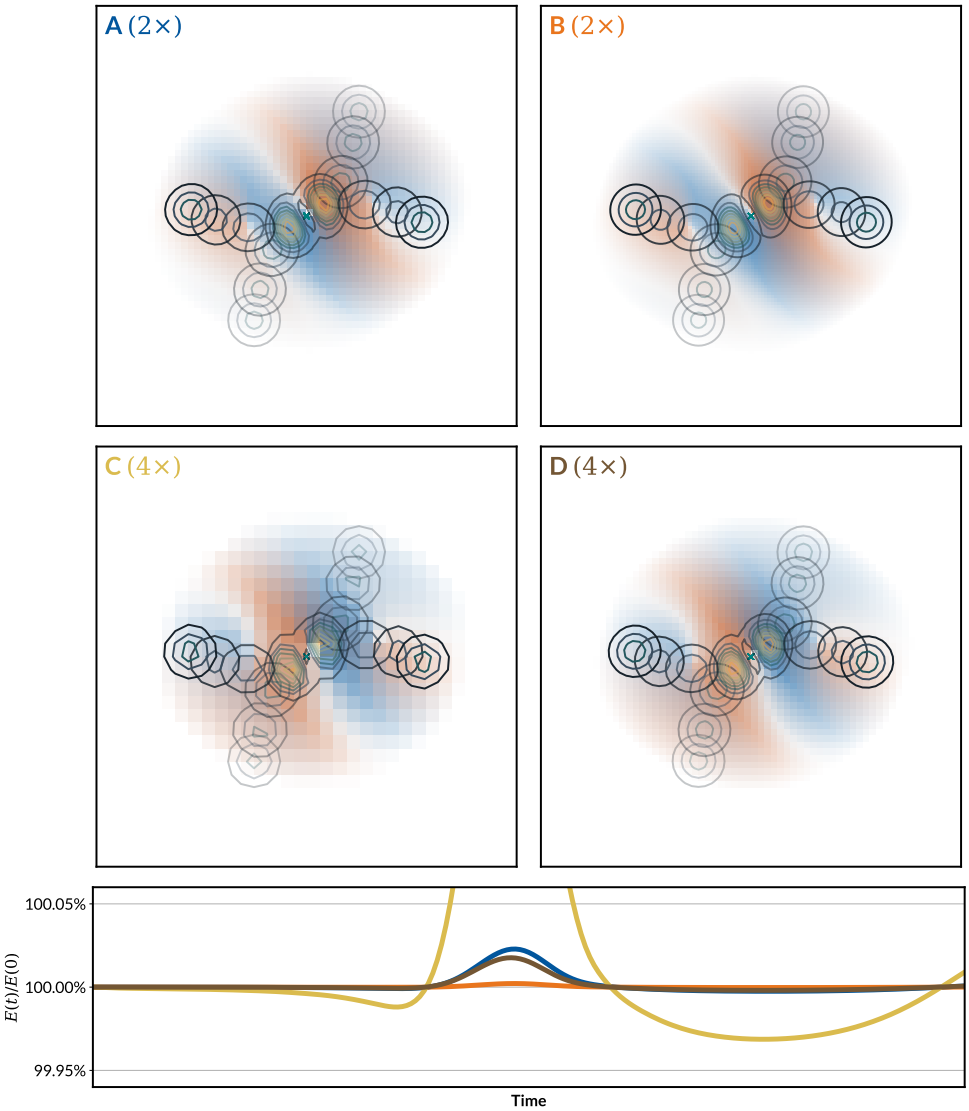

	N	L	Eff. Resol.	Steps	Time taken (s)
A	**128**	2	1x	644	32
B	**256**	2	2x	2574	867
C	**128**	4	0.5x	161	10
D	**256**	4	1x	644	267

Figure 4.2: Simulated scattering of two equal-mass solitons with an initial phase difference of π. The contour lines show the evolution of densities on the $x-y$ plane over time, while the colour overlays represent the phase information at the moment of closest approach. Information on systems' total energy conservation and simulation time on the author's Mac Studio is presented for four different settings.

4.1.2 $\mathrm{PyUltraLight}$ Code Units

It is practical to use units that absorb quantities such as H_0, G, $\hbar$ and c. The units that we adopt for mass $\mathcal{M}_\mathsf{c}$, time $\mathcal{T}_\mathsf{c}$, and length $\mathcal{L}_\mathsf{c}$are thus,

$$\begin{aligned}\mathcal{M}_\mathsf{c} &= \frac{1}{G}\sqrt[4]{\frac{3H_0^2\Omega_{m0}}{8\pi}}\left(\frac{\hbar}{m_\mathsf{A}}\right)^{\frac{3}{2}} \\ &\approx 70.4\left(\frac{10^{-23}\mathsf{eV}}{m_\mathsf{A}}\right)^{\frac{3}{2}}\mathsf{M}_\odot\end{aligned} \tag{4.5}$$

$$\mathcal{T}_\mathsf{c} = \sqrt{\frac{8\pi}{3H_0^2\Omega_{m0}}} \approx 75.1\mathsf{Gyr}, \tag{4.6}$$

$$\mathcal{L}_\mathsf{c} = \sqrt[4]{\frac{8\pi\hbar^2}{3m_\mathsf{A}^2H_0^2\Omega_{m0}}} \approx 121\sqrt{\frac{10^{-23}\mathsf{eV}}{m_\mathsf{A}}}\mathsf{kpc}, . \tag{4.7}$$

$\mathrm{PyUltraLight}$ can translate a variety of physical quantities between code units and physical units, including time, length, and mass, but also acceleration, momentum, density, and energy.

4.1.3 Simulation Boundary Conditions

The Fourier integrator naturally endows our simulation with periodicity in all three directions, which can drive our simulations away from reality over long runs, and violate the conservation of energy and momentum. This can either be due to “crosstalk”, where the wavefunction near the boundary is influenced by the neighbouring image of the simulation domain, or “wrapping”, where matter ejected from one end of the simulation domain spuriously returns from the opposite end instantaneously.

In our discussion of ULDM dynamical friction, Section 5, we take advantage of the periodicity and set the simulation domain to be an exact multiple of the ULDM de Broglie wavelength, achieving a much larger effective simulation domain.

For general simulations, it is, however, imperative that we keep the majority of the mass density and energy density sufficiently far from the simulation domain, and implement variations on the default boundary to improve the realism, efficacy, or stability of our simulations. The three boundary conditions currently implemented in $\mathrm{PyUltraLight}$ are shown in Figure 4.3.

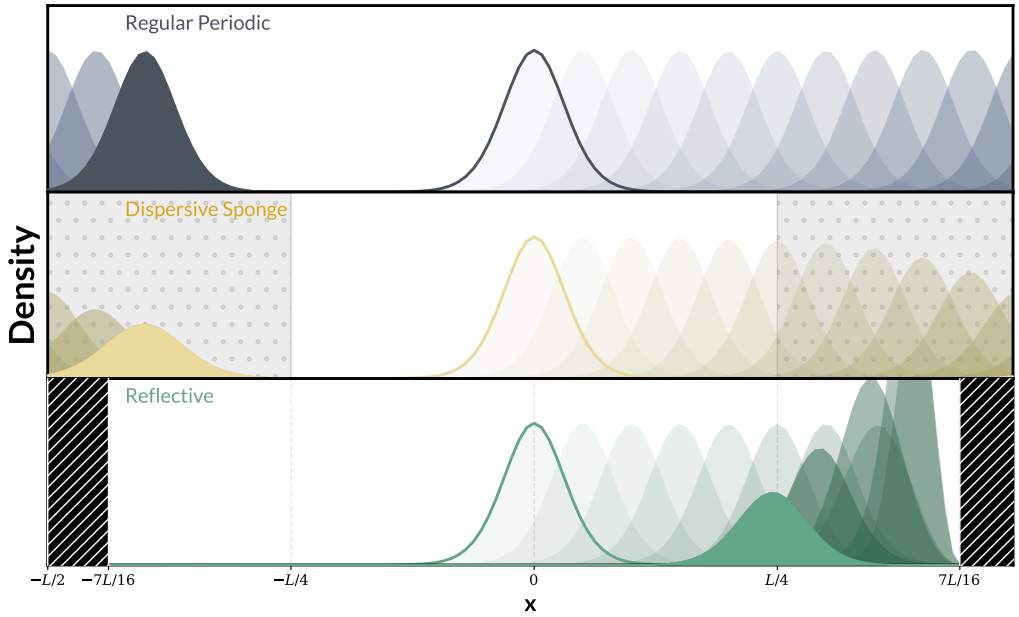

Figure 4.3: A soliton moving from the origin to the right, with the three kinds of boundary conditions discussed in text

4.1.3.1 Reflective Boundary

The reflective boundary condition prevents any ULDM from escaping the simulation domain by establishing an *infinite potential well* around a region of interest. This is achieved by setting the wavefunction amplitude outside a subdomain (of any shape) to zero, effectively causing repulsion effects when ULDM approaches.

4.1.3.2 Dispersive Sponge Boundary

For simulations that eject matter outwards, it can be more beneficial if we repress the outgoing matter in a more sophisticated manner than simply bouncing it back. This helps prolong the duration of simulation validity while avoiding increasing the size of the simulation domain.

The sponge boundary condition in $\mathrm{PyUltraLight}$ is enforced by adding an imaginary component to the system potential.

$$\psi_{\mathsf{DS}}(\mathbf{x}, t+\Delta t) = \psi(\mathbf{x}, t+\Delta t) e^{-\Delta t D(r)}, \tag{4.8a}$$

$$D(r) = 0.3\left(2 - \tanh\left(\frac{1+s}{2(1-s)}\right) + \tanh\left(\frac{2r}{L(1-s)} - \frac{1+s}{2(1-s)}\right)\right), \tag{4.8b}$$

where s controls the size of the sponge. The default value $\mathrm{PyUltraLight}$ takes is $s = 0.5$.

4.1.4 Isolated Potential

The isolated potential (I.P.) numerical routine is computational trick where we effectively double the simulation region when calculating Φ by padding the domain with zero in all directions [65]. This is helpful for high-resolution runs where further enlargement of the domain resolution is infeasible, as well as simulations where significant ULDM moves towards the boundary.

An example of this is shown in Figure 4.4, where we can see as a soliton drifts to the right, its ghost image emerging from the left boundary is significantly suppressed when the I.P. routine is enabled. Additionally, the two methods give different values for Φ due to the different choices for the surface of zero potential. Nonetheless, they yield practically the same relative shape.

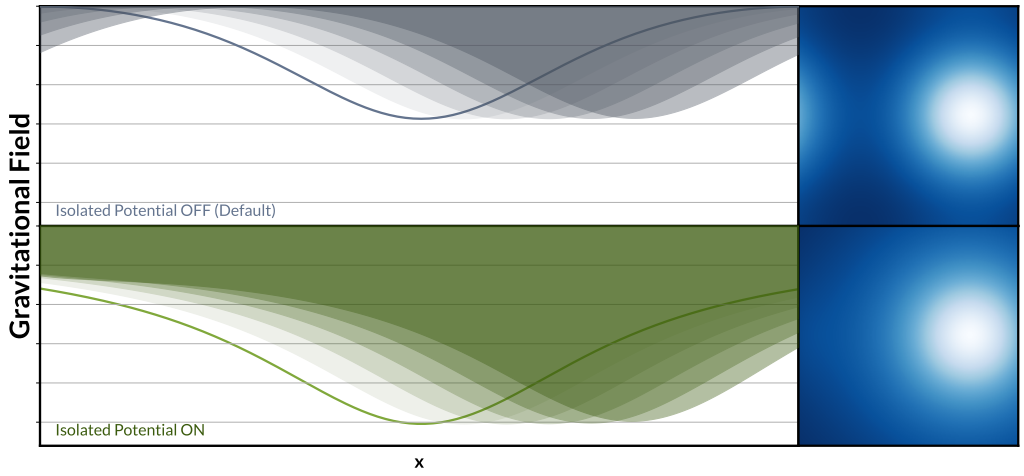

Figure 4.4: The gravitational field produced by a soliton moving from the origin to the right, without and with I.P. enabled. The 2D slice plots of the final snapshot are presented in the right column. Observe how the I.P. effectively suppressed the ghost image arising from the periodic boundary.

4.2 Coupling ULDM to an N Body System

When the ULDM is coupled to particles, the equations of motion become

$$i\hbar\dot{\psi} = \left[-\frac{\hbar^2}{2m_{\mathsf{A}}}\nabla^2 + m_{\mathsf{A}}(\Phi_{\mathsf{U}} + \Phi_{\mathsf{N}})\right]\psi, \tag{4.9a}$$

$$\nabla^2\Phi_{\mathsf{U}} = 4\pi G m_{\mathsf{A}}|\psi|^2, \tag{4.9b}$$

$$\Phi_{\mathsf{N}} = \sum_j^n \Phi_{\mathsf{N}_j}, \tag{4.9c}$$

$$\ddot{\mathbf{x}}_j = -\sum_{k\neq j}^n \boldsymbol{\nabla}\Phi_{\mathsf{N}_k}(\mathbf{x}_j) - \boldsymbol{\nabla}\Phi_{\mathsf{U}}(\mathbf{x}_j). \tag{4.9d}$$

Here ϕ_i is the gravitational field due to the i-th point mass. Equations 4.9d and 4.9c simply describe a rigid[6], point-based N body system, which the program handles using an explicit RK4 integrator. The flowchart of a PyUltraLight simulation is shown in Figure 4.5.

[6]For large particle ensembles, say $N \geq 10^5$, we have a grid-based routine where the N body potential is discretised before we evaluate gradients, the same way we evaluate Φ_{U}.

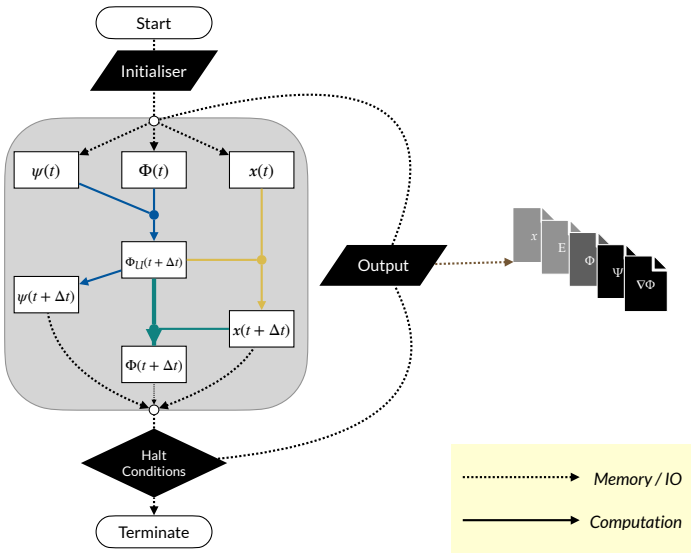

Figure 4.5: The loop logic of PyUltraLight , with details on how each step is taken.

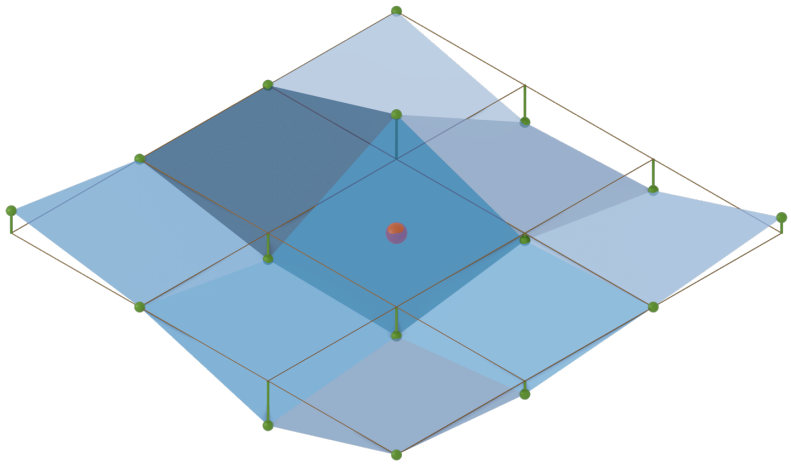

Figure 4.6: In this 2D version of the interpolating problem, to estimate the local gradient from information on nearby grid points our linear interpolation scheme uses grid information on the surrounding 4^2 grid points.

4.2.1 From Mesh to Force

The N body system moves over $\mathbb{R}^3$ while the ULDM field that it interfaces with is only defined over a discretised grid. In order to advance the particles in sync with the pseudo-spectral ULDM simulation an efficient interpolation scheme had to be implemented. After some experimentation and background research, we make use of a local trilinear interpolation.

We show the algorithm for one dimension on the grid, and an illustration for the two-dimensional equivalent is presented in Figure 4.6. The 2-D and 3-D equivalents simply means applying the 1-D algorithm once for each axis. For our grid there are N equi-distant mesh grids covering a physical interval of $\left[-\frac{L}{2}, \frac{L}{2}\right)$. For a mass m_j at position $x = x_j$, we first find the grid interval in the ULDM mesh that encloses it,

$$\begin{cases} n_j &= \left\lfloor N\left(\frac{x_j}{L} + \frac{1}{2}\right)\right\rfloor, \\ r_j &= N\frac{x_j - x_{n_j}}{L}, \end{cases}$$

where x_{n_j} is the coordinate of the n_j-th grid point. Then, we read the values of gravitational potential, Φ_{U}, at grid points n_j-1, n_j, n_j+1, and n_j+2. Their values allow us to compute a first-order approximation to the gradient via central differencing,

$$\begin{aligned}\Phi'_{\mathsf{U}}(x_j) &\approx r_j \Phi'_{n_j+1} + (1-r_j)\Phi'_{n_j} \\ &\approx \frac{N}{2L}\left[r_j(\Phi_{n_j+2} - \Phi_{n_j}) + (1-r_j)(\Phi_{n_j+1} - \Phi_{n_j-1})\right]. \end{aligned} \tag{4.10}$$

In the beginning of the project, an attempt was made where we interpolated using the plane wave components obtained from the FFT in the main $\mathrm{PyUltraLight}$ loop. However, given that the convergence of FFT is only guaranteed at mesh grids, so this did not deliver a reliable way to interpolate Ψ or Φ_U in general.

4.2.2 Smoothed Gravitational Potential

The finest physical length scale achieved by our simulations is on the order of parsecs, at which it is reasonable to treat the N body particles as point masses, regardless of their physical structures. However, the $1/r$ potential associated with an idealised point can compromise the numerical stability of our simulations: a point mass approaching arbitrarily close to a grid point will induce an arbitrarily deep potential well, causing the ULDM ψ to break down during the Fourier transform.

We thus smooth the potential by modelling the particles as Plummer spheres with variable sizes [66]. The Plummer potential is given by

$$\Phi_{\mathsf{P}}(r) = -\frac{M}{\sqrt{r^2 + r_{\mathsf{P}}^2}}, \tag{4.11}$$

where r_{P} is known as the Plummer radius. Figure 4.7 outlines how the smoothed potential compares with the $1/r$ potential, as well as the default settings for r_{P} employed by $\mathrm{PyUltraLight}$.

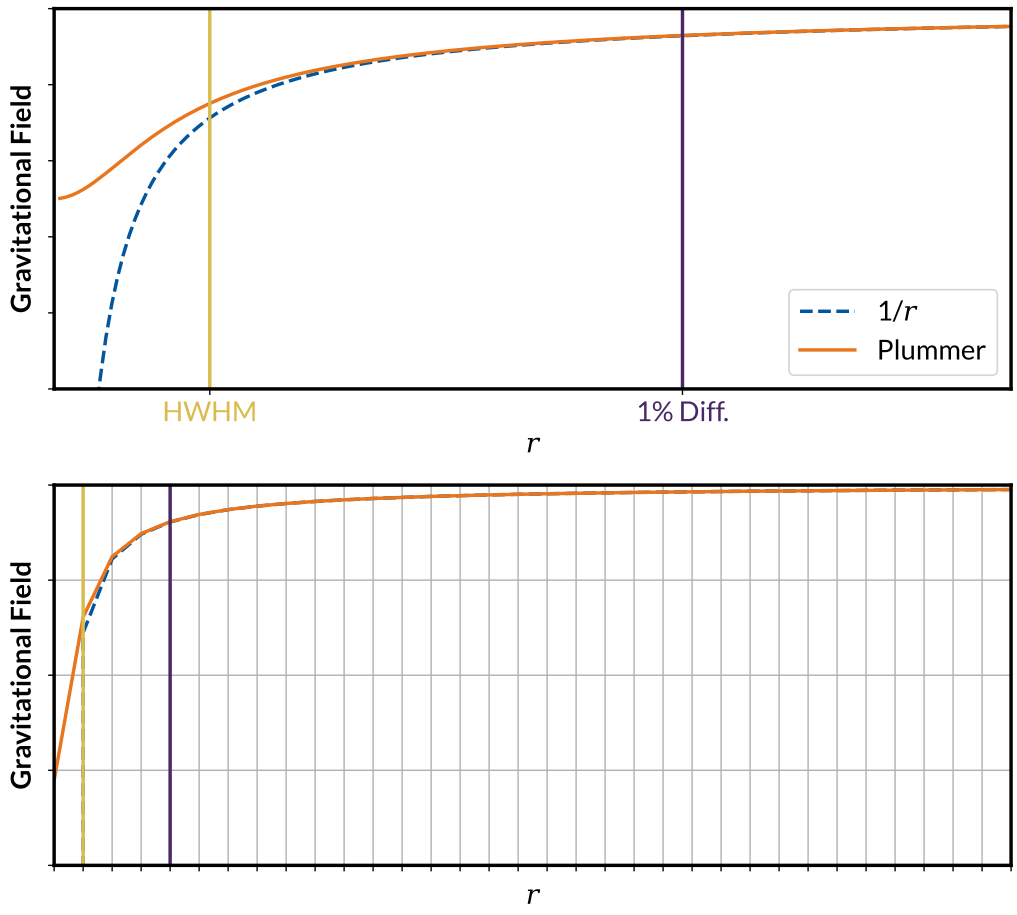

Figure 4.7: A comparison between a Coulomb potential and a typical Plummer potential. The lower panel highlights a set of simulation grids to illustrate the default PyUltraLight setting, where the Plummer HWHM is equal to the length of one grid.

The particle-particle gravitational force in simulations is obtained by differentiating Equation 4.11, though we note that the classical gravitational equation often suffices: for two masses M_1 and M_2

$$\mathbf{F}_{12} = -\frac{M_1 M_2}{|\mathbf{r}_{12}|^3}\mathbf{r}_{12}. \tag{4.12}$$

4.2.3 Pre-Relaxed Solitons

The soliton is a delicate equilibrium state between self-gravity and quantum pressure means we have to be "gingerly" when setting up a simulation. Initial conditions where a soliton is placed close to a considerable external gravitational potential can be problematic because they, like a compressed spring, proceed to oscillate around a new equilibrium until the excess energy is released, and it settles to a new ground state.

Such a nonlinear response makes it tricky to analyse many situations. To counter this, $\mathrm{PyUltraLight}$ can now compute soliton radial profiles that account for a massive particle embedded in its centre, and use the altered radial profile to initialise the simulation. The density profile of one such "pre-relaxed" soliton with a mass of 9 (code units) and an embedded point particle with mass 0.9 (code unit) is shown in Figure 4.8.

The numerical module we employ is called $\mathrm{PyUltraRound}$, a 1-D SPE solver that assumes spherical symmetry written by Lilian Guo. The code can find soliton profiles with arbitrary numbers of nodes. It employs a shooting method reminiscent of the tool we used to solve Equation 2.20 and generate the regular soliton in Chapter 2, and the reader is referred to Chapter 3 of [67] for a detailed discussion of the assumptions and algorithm.

As before the solver returns the $f(r)$ that satisfies the boundary condition $f(0) = 1$. From this, the other solitons can be recovered using the

scaling relationship (Equation 2.21). However, this means that α is also a variable that we have to solve for: for a given central potential, the mass of the soliton computed around it by $\mathrm{PyUltraRound}$ is not known a priori.

$\mathrm{PyUltraLight}$ uses a two-pass trial-and-error system to evaluate the soliton profile given an embedded mass. In the first pass, the code solves the SPE with a range of central black hole masses at a low resolution, and computes the resulting soliton's mass. Once a close match to the given mass ratio is found, the same parameters are fed into a repeat run with higher resolution and lower error tolerance. This method is robust for $M_{\mathsf{BH}}/M_{\mathsf{Soliton}} \leq 0.5$. The central potentials used in this process are Plummer spheres of user-specified diameters, and simple radial scaling of the soliton may occasionally violate this assumption.

A simple example is shown in Figure 4.9, where a standard soliton and a 10% point mass (**Default**), a suitably pre-relaxed soliton for the same point mass (**Pre-Relaxed**), and a default soliton on its own (**BH Absent**), travel in a straight line. The changes in their kinetic and gravitational energies are plotted over roughly one period in the left panels, and their density changes are illustrated using the contours in the right panels. It can be seen that the first configuration exhibits far more variation in both density and energy components, suggesting that it is displaced from equilibrium.

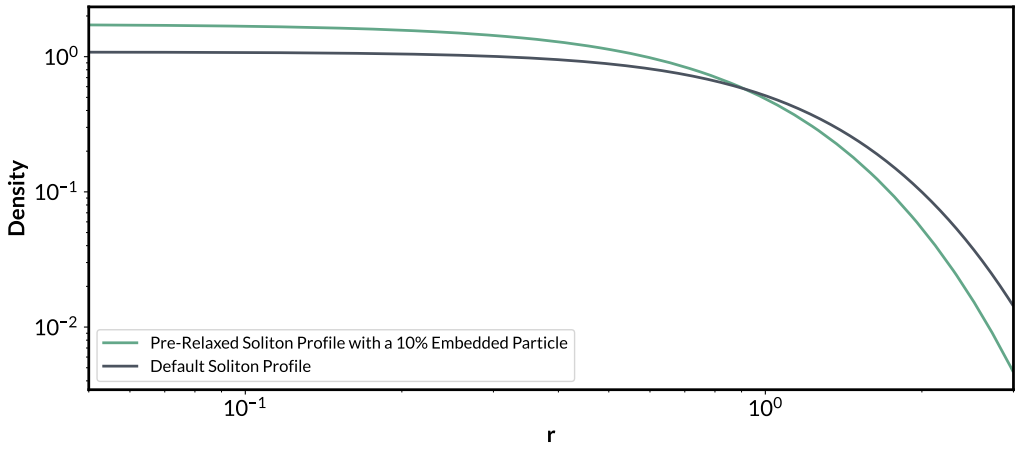

Figure 4.8: A ground state soliton profile computed in the presence of an embedded particle compared with the PyUltraLight default soliton that contains the same overall mass of ULDM.

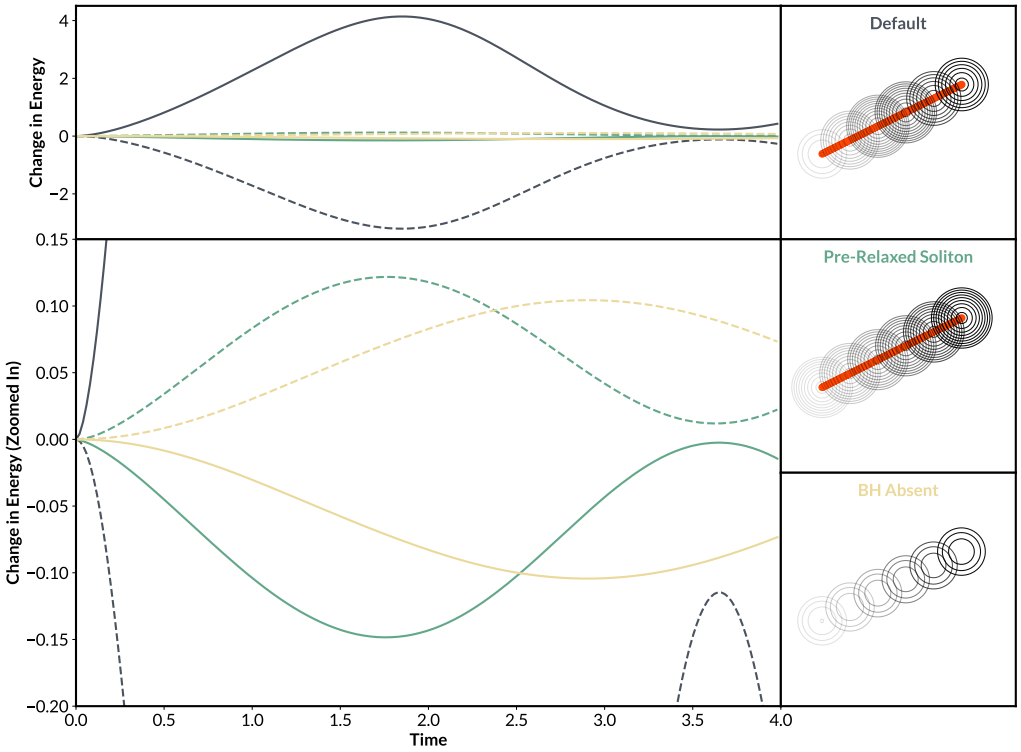

Figure 4.9: A simple evolution of embedded soliton-particle systems. The left panels show the ULDM energy components (solid line for E_{KQ} and dashed line for E_{GP}, as defined in Section 4.3.1). The right panels are individual density contours of the three setups described in text. We use the same scale across the three panels for the density contours.

4.3 Derived Quantities

4.3.1 Components of ULDM Energy

We approach ULDM energies from the perspective of the system's governing equations of motion, following the discussion in [60]. Over the entirety of spacetime, the action S whose variation over Φ, ψ, and ψ^* (and their respective time derivatives) that yields the SPEs can be written as

$$S[\Phi,\psi,\psi^*] = -\frac{1}{2}\int \mathrm{d}t \int_{\mathbb{R}^3} \mathrm{d}^3x \left(|\boldsymbol{\nabla}\Phi|^2 + 2\Phi\psi\psi^* + \boldsymbol{\nabla}\psi\boldsymbol{\nabla}\psi^* + i(\psi\dot{\psi^*} - \dot{\psi}\psi^*)\right). \tag{4.13}$$

The integrand of Equation 4.13 is the Lagrangian density, $\mathcal{L}$. We can use it to obtain an expression for the system energy,

$$\begin{aligned} E_{\mathsf{ULDM}} &= \int_{\mathbb{R}^3} \mathrm{d}^3x \left(\frac{\partial\mathcal{L}}{\partial\dot{\psi}}\dot{\psi} + \frac{\partial\mathcal{L}}{\partial\dot{\psi^*}}\dot{\psi^*} + \frac{\partial\mathcal{L}}{\partial\dot{\Phi}}\dot{\Phi} - \mathcal{L}\right) \\ &= \int_{\mathbb{R}^3} \mathrm{d}^3x \left(\frac{1}{2}\Phi|\psi|^2 - \frac{1}{2}\psi^*\nabla^2\psi\right) \qquad (4.14) \\ &\approx V_{\mathsf{Cell}} \sum_{\mathsf{Box}} E_{\mathsf{GP},j} + E_{\mathsf{KQ},j}, \qquad (4.15) \end{aligned}$$

where j are tuples of indices that run over the entire simulation domain.

The two non-vanishing terms in the integrand of Equation 4.14 are named thusly because the first is associated with the gravitational potential energy of the ULDM, whilst the second result from the combined contributions of the wavefunction's "kinetic effects" and "quantum pressure".

This quantity is not equivalent to the expectation value of the SPE Hamiltonian[7], which one can read off from Equation 2.13a,

$$\langle\mathcal{H}\rangle = \int_{\mathbb{R}^3} \mathrm{d}^3x \left(\Phi|\psi|^2 - \frac{1}{2}\psi^*\nabla^2\psi\right). \tag{4.16}$$

[7]The action that we used to derive the full SP system of equations is not the same as the action which we use to derive the common Schrödinger equation, so the conserved quantities which we call energy will have different functional forms.

When we introduce other sources of mass, they will also contribute to the potential Φ. Hence we further make the distinction between *self* gravitational potential energy and external gravitational potential energies, where relevant, in the next chapter. An example energy breakdown is shown in Figure 4.10.

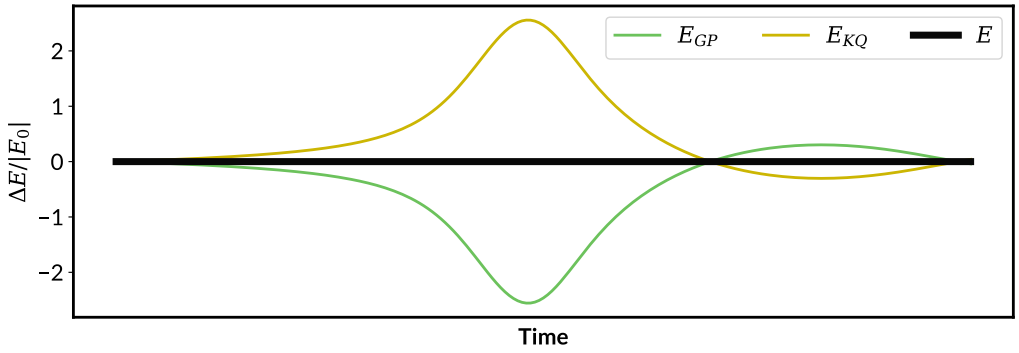

Figure 4.10: Energy components for the process shown in Figure 4.2 (B)

4.3.2 Momenta, Angular Momenta, and Vortices

The ULDM wavefunction encodes information for both density and speed, and the need to evaluate momentum, both globally and per-cell, arose from our interest in the simulation of black hole binaries inside a ULDM medium, as we discuss in the next chapter. For a fluid distribution with density $\rho(\mathbf{r})$ and velocity field $\mathbf{v}(\mathbf{r})$, the total momentum is

$$\mathbf{p} = \int_{\mathbb{R}^3} \mathrm{d}^3\mathbf{r}\rho(\mathbf{r})\mathbf{v}(\mathbf{r}). \tag{4.17}$$

When we model this system over a uniform mesh grid, this discretises to

$$\mathbf{p} \approx V_{\text{Cell}} \sum_{\text{Box}} \rho_j \mathbf{v}_j. \tag{4.18}$$

We begin with the Madelung picture, Equation 2.16. Explicit evaluation of $\mathbf{v} = \boldsymbol{\nabla}\theta$ is disfavoured due to the cyclic nature of $\theta \in [-\pi, \pi)$. Rather, we

can evaluate $\boldsymbol{\nabla}\psi$ in the frequency domain,

$$\boldsymbol{\nabla}\psi = \mathcal{F}^{-1}\left(i\mathbf{k}\mathcal{F}(\psi)\right). \tag{4.19}$$

Temporarily denoting the wavefunction amplitude as $A := \sqrt{\rho}$ for clarity, we evaluate the following spatial gradient,

$$\begin{aligned}\boldsymbol{\nabla}\psi &= (\boldsymbol{\nabla}A)e^{i\theta} + i(\boldsymbol{\nabla}\theta)Ae^{i\theta} \\ &= (\boldsymbol{\nabla}A)\,\frac{\psi}{A} + i\,(\boldsymbol{\nabla}\theta)\,\psi.\end{aligned} \tag{4.20}$$

Rearranging to get the velocity term, we observe that

$$\begin{aligned}\boldsymbol{\nabla}\theta &= i\frac{\boldsymbol{\nabla}A}{A} - i\frac{\boldsymbol{\nabla}\psi}{\psi} \\ &= i\frac{\boldsymbol{\nabla}A}{A} - i\frac{1}{A^2}\psi^*\boldsymbol{\nabla}\psi.\end{aligned} \tag{4.21}$$

If we substitute this back to Equation 4.18, we obtain an estimate of the momentum,

$$\begin{aligned}\mathbf{p} &\approx V_{\text{Cell}}\sum_{\text{Box}} A_j^2(\boldsymbol{\nabla}\theta)_j \\ &= V_{\text{Cell}}\sum_{\text{Box}}\left[iA\boldsymbol{\nabla}A - i\psi^*\boldsymbol{\nabla}\psi\right]_j.\end{aligned} \tag{4.22}$$

An example momentum evaluation is presented in Figure 4.11, where a particle scatters off a ULDM soliton, and the two objects exchange momentum. The error in momenta remains sub-percent even when conducted at a rather lightweight 128^3 resolution.

To compute the total angular momentum of a system, say, for a moving soliton, one can simply take the cross product of p at each cell with a set of position vectors,

$$\mathbf{L} = \sum_{\text{Box}} \mathbf{r}'_j \times \mathbf{p}_j, \tag{4.23}$$

where $\mathbf{r}'_j$ are a set of position vectors with respect to an arbitrary point. In $\mathrm{PyUltraLight}$, this can either be the origin of the simulation domain, or the

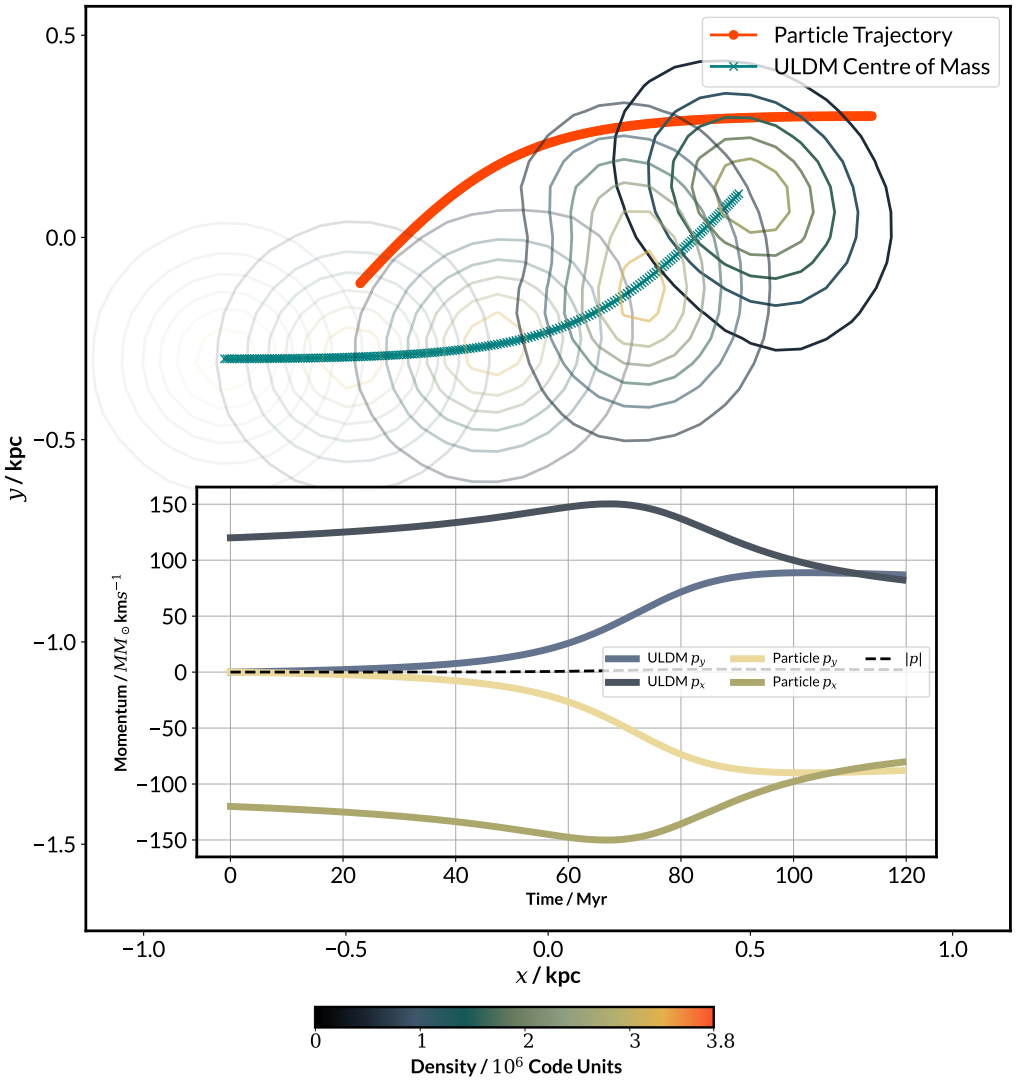

Figure 4.11: PyUltraLight simulation of a two-body scattering process between an equal-mass pair of a soliton and a particle. The top plot shows the trajectory and four snapshots of the ULDM density, while the inset shows the exchange between their momenta.

ULDM centre of mass. This functionality has been useful in the study of systems comprising of multiple solitons orbiting each other, an example of which is presented in Figure 4.12.

The simulated ULDM velocity field is irrotational by construction (the curl of a gradient vanishes). This actually reflects a defining characteristic of matter in superfluid state: irrotational and frictionless [27]. When angular momentum is imparted to a halo through, for example, merger dynamics, instead of making the entire ULDM structure rotate homogeneously, it excites inhomogeneous, quantised vortices instead. Works such as [68] discuss the stabilisation of such (SI)FDM vortices with a central potential.

For our uses, it is important to note the conservation of angular momentum is only respected until any ejected matter reaches the simulation boundary, because when a clump of ULDM “wraps around” the simulation domain, any angular momentum it carries with respect to the origin of the simulation domain will change sign, contributing incorrectly to the total angular momentum. Long runs that need angular momentum evaluation should be conducted in large boxes with sponge boundary conditions.

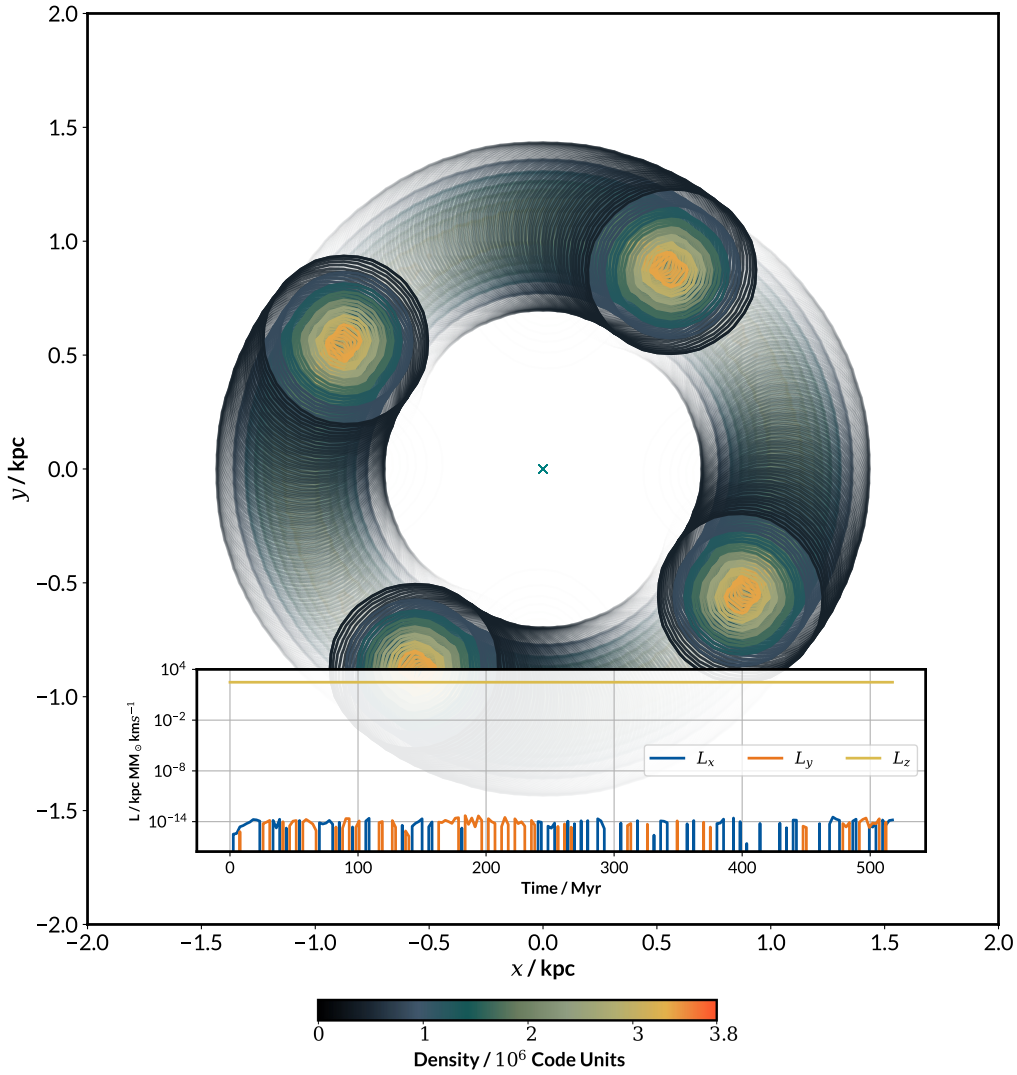

Figure 4.12: A toy model where four equal-mass solitons orbit each other. The program-evaluated angular momentum relative to the centre of mass (inset panel) indeed behaves as expected, with L_{xx} and L_{yy} vanishingly small compared with L_{zz}. This figure shows multiple overlapping snapshots, where later-time snapshots are more opaque.

4.3.3 Re-sampling ULDM Density and Tracking Bulk Motion

In many circumstances, we want to output Ψ in a region of interest, which may move within the simulation volume as the system evolves. However, saving the full 3D grid information of $\mathrm{PyUltraLight}$ simulations is often computationally expensive. We therefore evaluate the centre-of-mass coordinates of ULDM during runtime. $\mathrm{PyUltraLight}$ then uses a linear interpolator on the real and imaginary parts of ψ to return ψ information in any subsection of the domain. Centre-of-mass velocity $\mathbf{v}_{\mathsf{COM}}$ is also estimated using central differencing, and the re-sampled ULDM wavefunction can be corrected to remove this velocity,

$$\psi_R(\mathbf{x}', t) = e^{-i\mathbf{x}'\cdot\mathbf{v}_{\mathsf{COM}}}\psi(\mathbf{x}', t). \tag{4.24}$$

A rudimentary example of this is shown in Figure 4.13.

4.3.4 Dipole and Quadrupole Moments

In 3-dimensional space, the quadrupole moment of a distribution of mass $\rho(x, y, z)$ is a 3-by-3 matrix whose elements are

$$Q_{ab} = \int d^3\mathbf{r}\rho(\mathbf{r}) \left(3r_a r_b - |r|^2\delta_{ab}\right), \tag{4.25}$$

where the indices a and b run over x, y, and z, and δ_{ab} is the Kronecker delta. Figures 4.13 and 4.14 provide a pair of test cases for quadrupole evaluations. The first quantifies the tidal disruption during the scattering process presented in Figure 4.11, while the second deals with the interesting topic of soliton phases.

In the top panel of Figure 4.14, one can read off the system's approximate period from the Q time series. In the lower panels, the excitation of

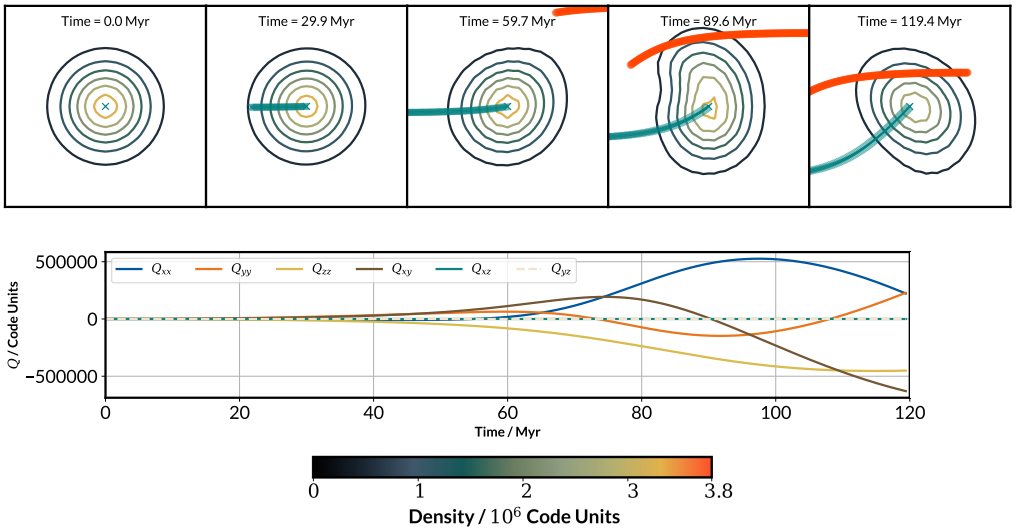

Figure 4.13: The same run as Figure 4.11, resampled in the rest frame of the soliton, alongside the quadrupole moment time series for each independent component. The colour scales for the two figures are the same.

the resulting ULDM structure is evident. We can further confirm that all simulated bulk motion are indeed in the x-y plane since Q_{xz} and Q_{yz} vanish in both Figures.

The quadrupole moment measured from the centre of mass can quantify the degree to which a soliton is disrupted, and this may be linked to the generation of gravitational waves, which we explore in future work [69].

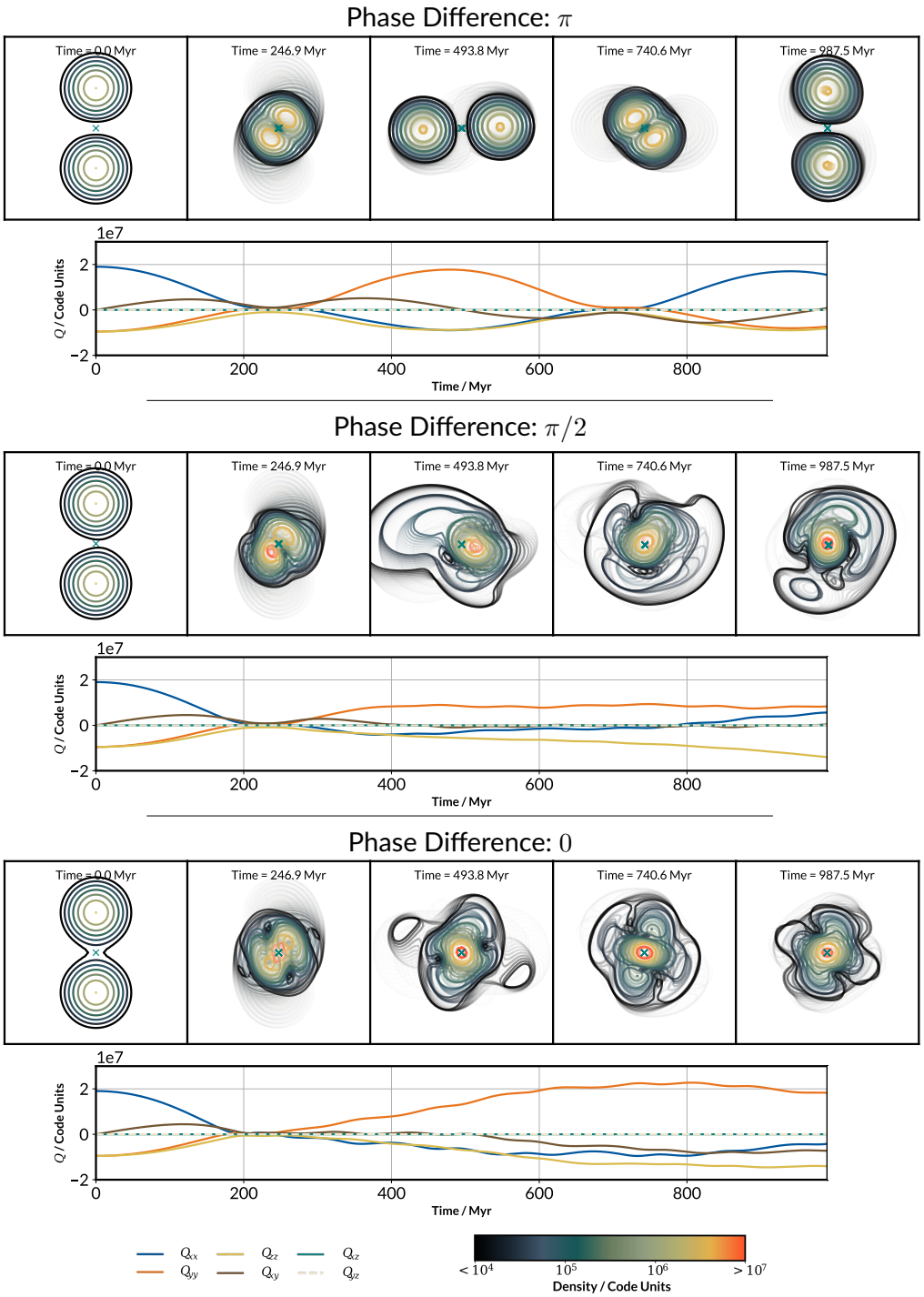

Figure 4.14: In the top panel, we have a pair of equal-mass solitons with a π difference in phase bounce off each other in the x-y plane. When this phase difference is reduced, however, the two solitons merge and become "excited" to varying extents, shown in the lower panels. The three series of density contour plots use the same colour scale.

4.3.5 Numerical Soliton Eigenmode Decomposition

For a simulation, assuming our dynamical evolution is perturbative in ψ and produce no significant impact on the system's total (time-averaged) gravitational potential $\langle\Phi\rangle$, it is possible to calculate an eigenbasis of the potential, and project our wavefunction into distinct quasinormal modes that each have an associated natural frequency. Discretised over grids, this manifests as an eigenvalue problem,

$$\left(\begin{bmatrix} \chi(r_1) & \cdots & \cdots & \cdots & 0 \\ 0 & \chi(r_2) & \cdots & \cdots & 0 \\ \vdots & \ddots & \ddots & \ddots & \vdots \\ 0 & \ddots & 0 & \chi(r_{n-1}) & 0 \\ 0 & \cdots & 0 & 0 & \chi(r_n) \end{bmatrix} - \frac{1}{\Delta r^2}\begin{bmatrix} -2 & 1 & 0 & \cdots & 0 \\ 1 & -2 & 1 & \cdots & 0 \\ \vdots & \ddots & \ddots & \ddots & \vdots \\ 0 & \ddots & 1 & -2 & 1 \\ 0 & \cdots & 0 & 1 & -2 \end{bmatrix}\right)\begin{bmatrix} u_1 \\ u_2 \\ \vdots \\ u_{n-1} \\ u_n \end{bmatrix} = 2E_{nl}\begin{bmatrix} u_1 \\ u_2 \\ \vdots \\ u_{n-1} \\ u_n \end{bmatrix}, \tag{4.26}$$

where $\chi(r) \equiv 2\langle\Phi\rangle(r) - l(l+1)/r^2$ is the gravitational potential with the centrifugal barrier, and $E_{n\ell}$ the eigenenergy. For the isolated soliton, its first few eigenbasis is shown in Figure 4.15. As with standard quantum mechanics, the expansion coefficients of a particular state can be obtained as inner products of the simulated wavefunction and this eigenbasis.

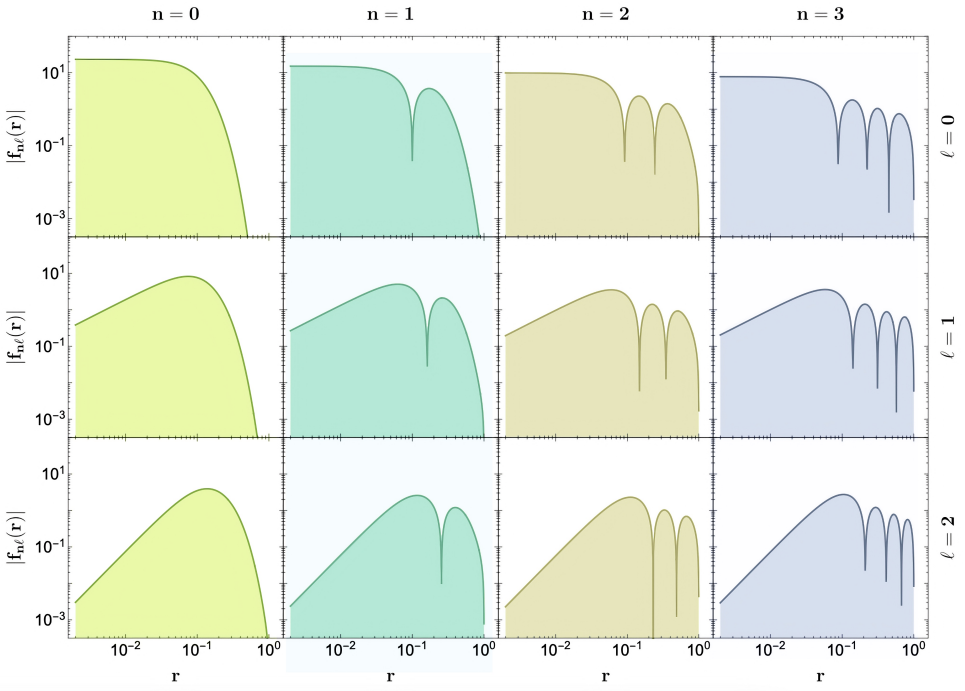

Figure 4.15: The first eigenmodes of the isolated soliton, adapted from [29]

4.3.6 ULDM Halo Construction

In 1979, M. Schwarzschild outlined a way to self-consistently approximate the phase-space distribution of stars inside an elliptical galaxy with a given density profile [70]:

1. take the target density profile and compute its corresponding gravitational potential,
2. generate a library of single-particle trajectories moving inside the potential for extended time,
3. assign appropriate weights to the orbits to recover the original density profile.

This method has been successfully generalised to construct dark matter halos for dynamical simulations as well. For ULDM, however, soliton eigen-

modes take the place of individual particle trajectories. This is described in detail by Yavetz et al. [71], and stands as an economic parallel to the "traditional" approach where halos are dynamically formed from soliton mergers. This method is employed in Section 6.3 to generate ULDM halos.

4.3.7 Correlation and Smoothness

We can easily obtain the spherically-averaged density profiles $\bar{\rho}(r)$ around the ULDM centre of mass, which only depends on the distance $r = |\mathbf{x}|$ from that point. The overdensity field is then defined as

$$\delta(\mathbf{x}) = \frac{\rho(\mathbf{x}) - \bar{\rho}(r)}{\bar{\rho}(r)} \,. \tag{4.27}$$

This quantity is sampled at n random points with coordinates $\mathbf{x}$ inside a spherical domain with radius r_{max}. We now define the two-point correlation function [72]

$$\begin{aligned} \xi(d) &= \langle \delta(\mathbf{x}) \delta(\mathbf{x}+d) \rangle \\ &= \frac{1}{V} \int \mathrm{d}^3 x \delta(\mathbf{x}) \delta(\mathbf{x}+d) \,, \end{aligned} \tag{4.28}$$

which quantifies the smoothness of the density field.

4.4 AxioNyx: Baryonic Physics

4.4.1 Outline of Algorithm

Our work developed a modified version of AxioNyx with the capability to simulate ULDM and gas dynamics together. AxioNyx has two different pseudo-spectral schemes to solve the SPE: one at second order, the same as used in PyUltraLight , and another at sixth order. Absorbing coefficients into tuples labelled $\{c_\alpha, d_\alpha\}$ as summarised in Table 1 of [61], we can write down the schemes as

$$\psi(t+\Delta t) = \prod_\alpha \exp\left(-i\Delta t\left(c_\alpha \frac{k^2}{2m_{\mathsf{A}}a^2} + d_\alpha m_{\mathsf{A}} V_\alpha(x)\right)\right)\psi(t). \tag{4.29}$$

On the hydrodynamical side, Nyx represents the simulation state of the gas as

$$\bar{U} = [\rho_b, a\rho_b U, a^2\rho_b E, a^2\rho_b e], \tag{4.30}$$

and the flux vector is defined as

$$\mathbf{F} = [1/a, \rho_b U, \rho_b UU, a(\rho_b UE + pU), a\rho_b Ue]. \tag{4.31}$$

Denoting the local gravitational field as $-\boldsymbol{\nabla}\Phi = \mathbf{g}$, the time-evolution terms for internal energy, gravity, and heating-cooling are

$$S_e = [0, 0, 0, -ap\boldsymbol{\nabla}\cdot U] \tag{4.32a}$$

$$S_g = [0, \rho_b\mathbf{g}, a\rho_b U\cdot\mathbf{g}, 0] \tag{4.32b}$$

$$S_{HC} = [0, 0, a\Lambda_{HC}, a\Lambda_{HC}] \tag{4.32c}$$

Following Equation 3.7, the overall gas evolution equation is now,

$$\frac{\partial\bar{U}}{\partial t} = -\boldsymbol{\nabla}\cdot\mathbf{F} + S_e + S_g + S_{HC}, \tag{4.33}$$

where the divergence is evaluated per-variable. The algorithm for one step (at a given level of refinement) is given in Figure 4.16

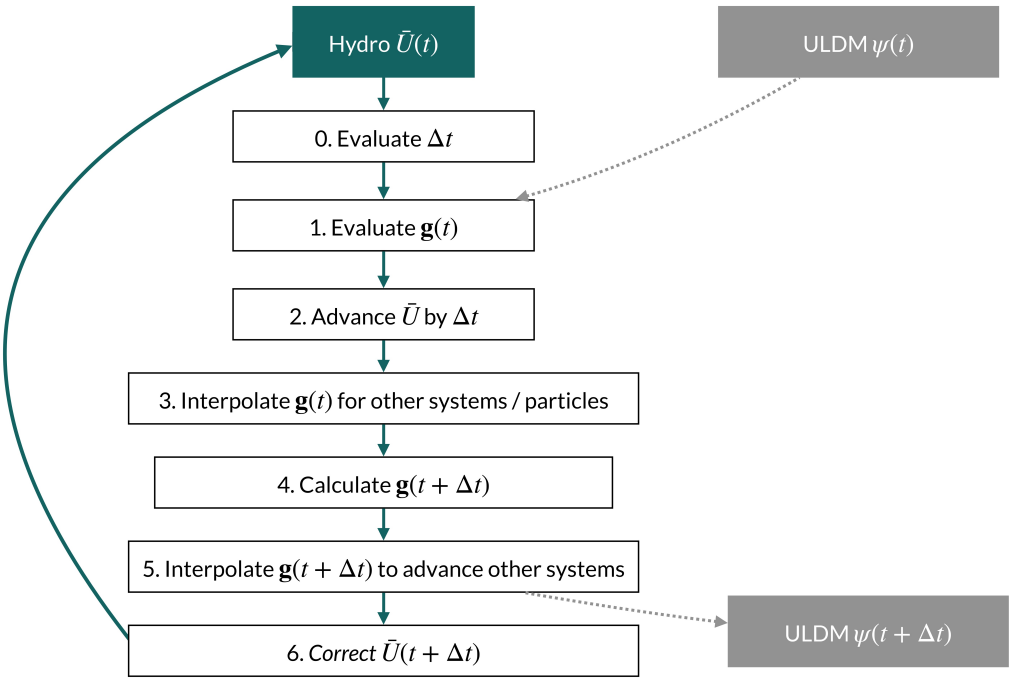

Figure 4.16: Breakdown of one simulation step of AxioNyx , based on [59, 61]. The ULDM advance itself employs either the pseudospectral (root grid) or finite difference (refined grid) numerical routines.

4.4.2 Adaptive Mesh Refinement

Adaptive mesh refinement (AMR) using block structures was introduced by Berger and Oliger in the 1980s [73] and has seen use in a wide variety of computational applications. The AMR methodology employed by Nyx/AxioNyx uses a nested hierarchy of rectangular grids with refinement of the grids in space by a factor of two between levels. Furthermore, refinement in the lengths of time steps between levels is dictated by the subcycling algorithm. The program default requires that Δt be halved for a region of $2\times$ refinement, for example.

Refinement is triggered by pre-set criteria related to the simulation state. The one we use the most commonly is a density threshold, while it is also possible to set triggers based on density gradient, (gas) temperature, and momentum. Due to the way ULDM velocities are defined, rapid flows require refinement to faithfully simulate, even if the density is low. However, we assume that the detailed behaviour of low-density high-speed flows does not significantly alter the overall dynamics.

Autour de nous, les étoiles continuaient leur marche silencieuse, dociles comme un grand troupeau.
Around us, the stars continued their silent march, docile like a great flock.

Alphonse Daudet, *Les Étoiles (The Stars)*

5

ULDM Dynamical Friction[1]

We analyse a point-like massive particle interacting with self-gravitating quantum matter. The overall investigation is motivated by the dynamics of super-massive black holes (SMBH) moving inside Ultralight Dark Matter (ULDM) halos.

This chapter is complementary to that of Lancaster *et al.* [45] who give numerical and analytic treatments of both point-like and extended masses moving through a ULDM background. We provide more numerical detail, but focus on point masses. The uniform background case is primarily a test for our code, recovering known analytic solutions (which are analogous to a

[1]This chapter is based on the publication [74], with some updates to better fit in the context of further investigations that it has since influenced.

much older problem in electron propagation [41]) in the limit where the self-gravity of the quantum matter is ignored and the point mass moves with constant velocity. However, a point mass moving in an otherwise undisturbed ULDM background leaves an elongated overdensity in its wake, which eventually undergoes gravitational collapse. The deep potential of the resulting overdensity then brings the moving mass to a rapid standstill.

Conversely, when a black hole interacts with a ULDM halo the central soliton has already collapsed and is supported by "quantum pressure". We consider a the idealised scenario of a mass in an initially circular orbit around an unperturbed soliton. We broadly confirm simple estimates of the timescales over which an orbiting mass sinks to the centre of the halo. However, the moving mass excites oscillations in the soliton independently of the dynamical friction, and the resulting motion can be complicated and stochastic. In particular, we see possible evidence that an orbiting black hole will be "reheated" as it interacts with the now-dynamical soliton for some parameter combinations. This appears to increase the likelihood of core-stalling in SMBH mergers in a ULDM dominated universe in a way that is distinct from the heating of black hole binaries by the granular nature of ULDM halos, described by Bar-Or *et al.* [58]. Consequently for both uniform backgrounds and solitonic configurations we find that non-perturbative backreaction introduces qualitatively new phenomena into ULDM dynamics.

This work rests on numerical solutions of the coupled Schrödinger-Poisson equation. In what follows we set the axion mass to 10^{-22} eV for the idealised scenario of a point mass moving in a uniform ULDM background. This system has no direct astrophysical analogue and could be treated as dimensionless However, this value is often adopted as a fiducial ULDM mass [27] and providing concrete numbers contextualises the

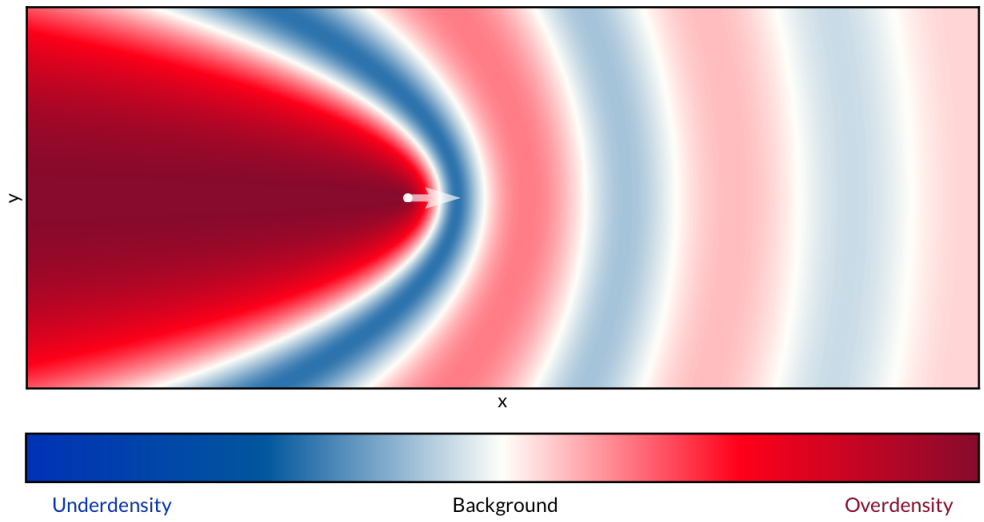

Figure 5.1: The analytic density profile for a Coulomb scattering process involving a mass travelling to the right (with back-reaction neglected). The overdense tail extends infinitely behind it. The numerical scales are omitted since the underlying equation is linear.

results. When looking at interactions between point masses and ULDM solitons we set $m = 10^{-21}$ eV, given that larger values are broadly preferred by the data although our overall focus here is the underlying dynamics of these systems, not their detailed astrophysics.

We use periodic spatial boundary conditions. For the case of a black hole moving in a uniform ULDM background we limit the duration of simulations to

$$t_{\text{Max}} = \frac{L}{2v_{\text{rel}}}, \tag{5.1}$$

so that the ULDM wake is prevented from "wrapping round" the periodic boundary. This is less of an issue when the black hole interacts with a soliton.

5.1 Steady State Gravitational Wakes

In the limit that the self-gravity of the wake is negligible and the point mass travels at a constant velocity, the problem reduces to Coulomb scattering [41, 57] in the reference frame in which a stationary mass is subject to an "axion wind". Consequently, we assume the particle of mass M is at the origin immersed in an axion flow with velocity $\mathbf{v} = -v_{\mathsf{rel}}\hat{x}$ and density ρ when undisturbed.

Ignoring axion self-gravity and denoting the radial coordinate $\mathbf{r} = x\hat{\mathbf{x}} + y\hat{\mathbf{y}} + z\hat{\mathbf{z}}$, the system obeys the time-independent Schrödinger equation $E\psi = \hat{H}\psi$,

$$\left[\frac{mv^2}{2} + \frac{GMm}{r} + \frac{\hbar^2}{2m}\nabla^2\right]\psi(\mathbf{r}) = 0. \tag{5.2}$$

This has an analytical solution in the form of a confluent hypergeometric function,

$$\begin{aligned}\psi(\mathbf{r}) =& \sqrt{\rho}e^{\pi\beta/2+2\pi i x/\lambda_{\mathsf{dB}}}|\Gamma(1-i\beta)|\times \\ & M\left[i\beta, 1; i\frac{2\pi(r+x)}{\lambda_{\mathsf{dB}}}\right].\end{aligned} \tag{5.3}$$

In Equation 5.3, $\lambda_{\mathsf{dB}} = h/(mv_{\mathsf{rel}})$ is the axion de Broglie wavelength and the inverse quantum Mach number is

$$\beta = 2\pi\frac{GM}{v^2\lambda_{\mathsf{dB}}}, \tag{5.4}$$

and we have

$$M(a, b; z) = \sum_{n=0}^{\infty}\frac{a^{(n)}z^n}{b^{(n)}n!}, \tag{5.5}$$

where $p^{(q)}$ is the Pochhammer symbol,

$$p^{(q)} \equiv \frac{\Gamma(p+q)}{\Gamma(p)}. \tag{5.6}$$

Figure 5.1 illustrates a typical density profile.

The dynamical friction is supplied by the gravitational field of the overdense wake. However, a naive integral of the source over $\mathbb{R}^3$ diverges since the overdensity approaches a non-zero constant value at arbitrary large distances behind the moving mass. This problem (which stems from the unphysical assumption that the semi-infinite wake can be generated at a constant velocity within finite time) is solved by introducing a spatial cutoff scale, b, the distance traveled by the mass relative to the medium. It is also helpful to expresses b in units of the axion de Broglie wavelength, denoted as $\tilde{b}$,

$$\tilde{b}(t) = \frac{2\pi b}{\lambda_{\mathsf{dB}}} = \frac{m v_{\mathsf{rel}}(t)}{\hbar} \int_0^t v_{\mathsf{rel}}(t')dt', \tag{5.7}$$

If the mass travels at constant velocity, the dynamical friction is [57, 45]

$$F_{\mathsf{DF}} = 4\pi\bar{\rho}C(\tilde{b}) \left(\frac{GM}{v_{\mathsf{rel}}}\right)^2, \tag{5.8}$$

where $C(\tilde{b})$ is a friction coefficient. The gravitational force on the mass is $-M\partial\Phi_U/\partial x$, so approximately we have

$$C(\tilde{b}) = \frac{v_{\mathsf{rel}}^2}{4\pi\bar{\rho}G^2M} \left|\frac{\partial\Phi_U}{\partial x}\right|. \tag{5.9}$$

When $\beta \ll 1$ we can extract $C(\tilde{b})$ from the wavefunction, Equation 5.2,

$$C(\tilde{b}) = \mathsf{Cin}(2\tilde{b}) + \mathsf{sinc}(2\tilde{b}) - 1 + \mathcal{O}(\beta), \tag{5.10}$$

where $\mathsf{Cin}(x) \equiv \int_0^x [(1-\cos(t))/t]\,dt$ and $\mathsf{sinc}(x) \equiv \sin(x)/x$. In the limit that $\tilde{b} \ll 1$, one evaluates

$$C(\tilde{b}) \approx \frac{1}{3}\tilde{b}^2. \tag{5.11}$$

5.2 Simulation Without Self-Gravity

We begin with simulations without ULDM self-gravity. As before, we assume a mass moving along the x axis in an initially uniform ULDM medium

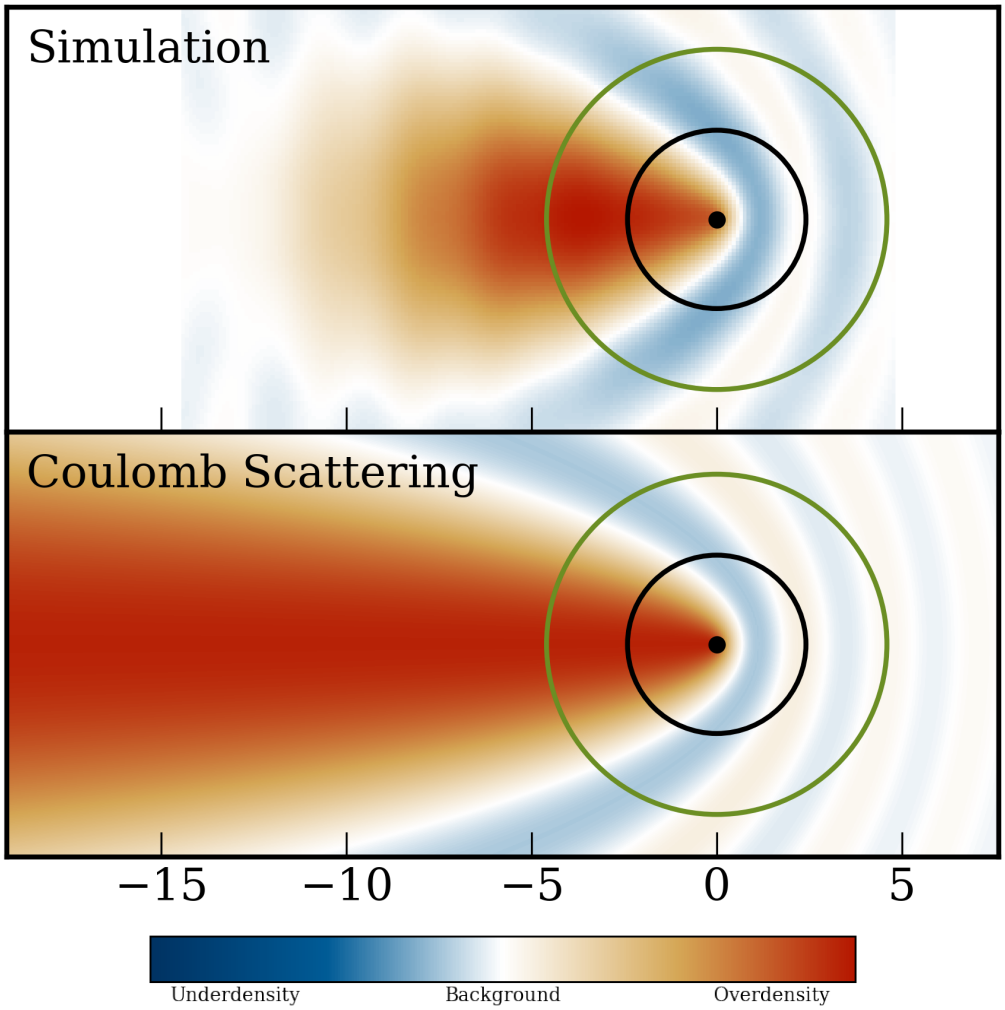

Figure 5.2: A slice of the simulated overdensity at 192^3 resolution without self-gravity versus the analytical Coulomb scattering result (Equation 5.3). The length unit are in kiloparsecs, and the circle overlays represent instantaneous values of λ_{dB} (black) and b (green).

at a constant velocity. Unless noted otherwise, the simulations shown in

this section are produced with:

$$\begin{aligned} L &= 4\lambda_{\mathsf{dB}} \approx 9.63\ \mathsf{kpc}\ , \\ \rho_0 &= 10^7 \rho_{\mathsf{crit}} \approx 1.27 M_\odot/\mathsf{pc}^3\ , \\ M_{\mathsf{BH}} &= 10^7 M_\odot\ , \\ v_{\mathsf{rel}} &= 50\ \mathsf{km/s} \\ r_P &= 48\ \mathsf{pc}\ , \\ \beta &= 0.0449\ , \\ m_{22} &= 1\ . \end{aligned}$$

These quantities can be calibrated against expectations for the central solitonic condensations of ULDM halos [75]:

$$\rho_c = 2.94 \times 10^{-3} M_\odot \mathsf{pc}^{-3} \left(\frac{M_{\mathsf{vir}}}{10^9 M_\odot}\right)^{4/3} m_{22}^2, \tag{5.12a}$$

$$r_c = 1.6 \mathsf{kpc} \left(\frac{M_{\mathsf{vir}}}{10^9 M_\odot}\right)^{-1/3} m_{22}^{-1}, \tag{5.12b}$$

where ρ_c and r_c are the central density and HWHM radius of a halo with virialised mass M_{vir}. The background density in our simulations is similar to that of the solitonic core of a $10^{11} M_\odot$ halo, but our uniform-density simulated volume is substantially larger than the soliton. In Fig. 5.2 we compare a simulation (with axion self-gravity disabled) to the steady state Coulomb solution. There is good qualitative overlap between the two solutions in the the vicinity of the mass point. However, the wake is truncated in the numerical simulation as a consequence of the finite duration of the calculation.

We can work with two inertial frames, the *ULDM frame* and the *initially comoving frame*. In the former, the mass has initial velocity $\mathbf{v}_m = v_{\mathsf{rel}} \hat{\mathbf{x}}$ in a stationary ULDM background. In the latter, the mass is initially at rest,

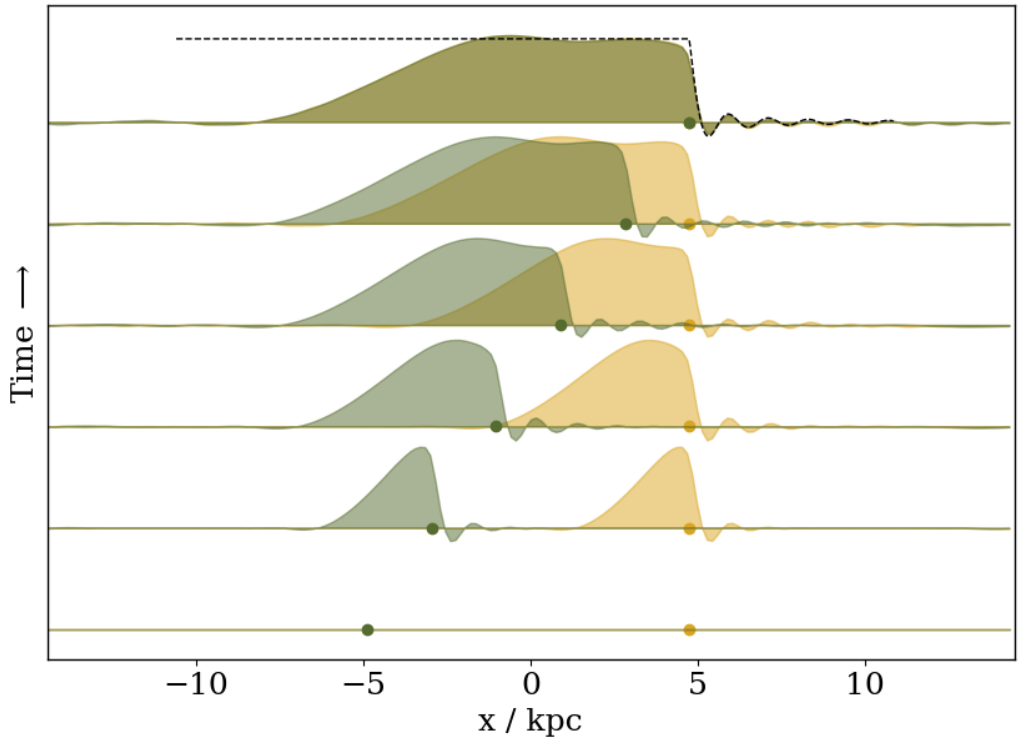

Figure 5.3: The overdensity along the x-axis in the co-moving (green) and the ULDM (yellow) frames, as described in the text. The analytical density profile due to Equation 5.3 is superimposed on the final snapshot.

embedded in a ULDM background moving with velocity $-v_{\text{rel}}\hat{\mathbf{x}}$. Fig. 5.3 illustrates that our simulations are consistent between these frames.

If the dynamical friction does not alter v_{rel} significantly, Equation 5.7 reduces to

$$\tilde{b} = \frac{m v_{\text{rel}}^2}{\hbar} t. \tag{5.13}$$

Evaluating $C(\tilde{b})$ via Equation 5.10, we can quantitatively compare the simulation with the analytical results, as shown in Fig. 5.4. The simulation results are obtained via Equation 5.9, which is a direct measure of the force. This is a nontrivial test of the code in that it demonstrates that using a "cut-off" to compute the dynamical friction is a good match to that given by the time-dependent wake.

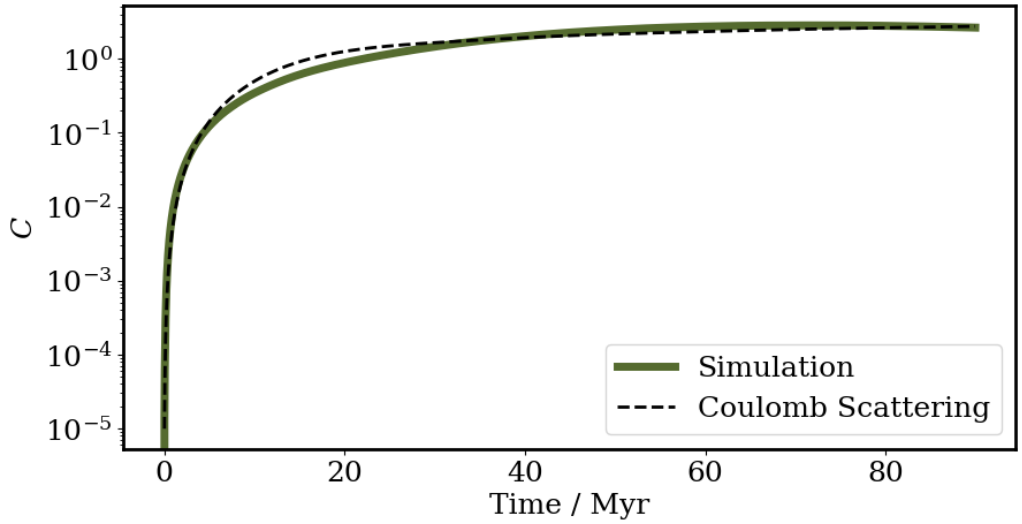

Figure 5.4: The dynamical friction coefficient, C, extracted from a canonical simulation without self-gravity, plotted against time. A theoretical result obtained by substituting $b = v_{\text{rel}}t$ into Equation 5.10 is superimposed.

5.3 Simulations with Self-Gravity

We now enable ULDM self-gravity, and allow the travelling mass to slow down in response to the ULDM potential. In this case, the wake undergoes gravitational collapse forming a high-density region behind the particle. The resulting gravitational potential greatly increases the dynamical friction, bringing the particle to a rapid halt.

Fig. 5.5 illustrates the time-evolution of such an overdensity. It initially tracks the previous case, but eventually tips over into a runaway collapse. We plot C and $\tilde{b}$ for our representative solution in Fig. 5.6. Once the collapse is well underway, v decreases, causing $\tilde{b}$ to similarly decrease.

In Fig. 5.7, we show the energy transfer between the moving mass and the background medium in the two reference frames. In the initially co-moving frame the total kinetic energy is larger since a much greater mass of ULDM is moving toward the black hole, in contrast to the ULDM rest

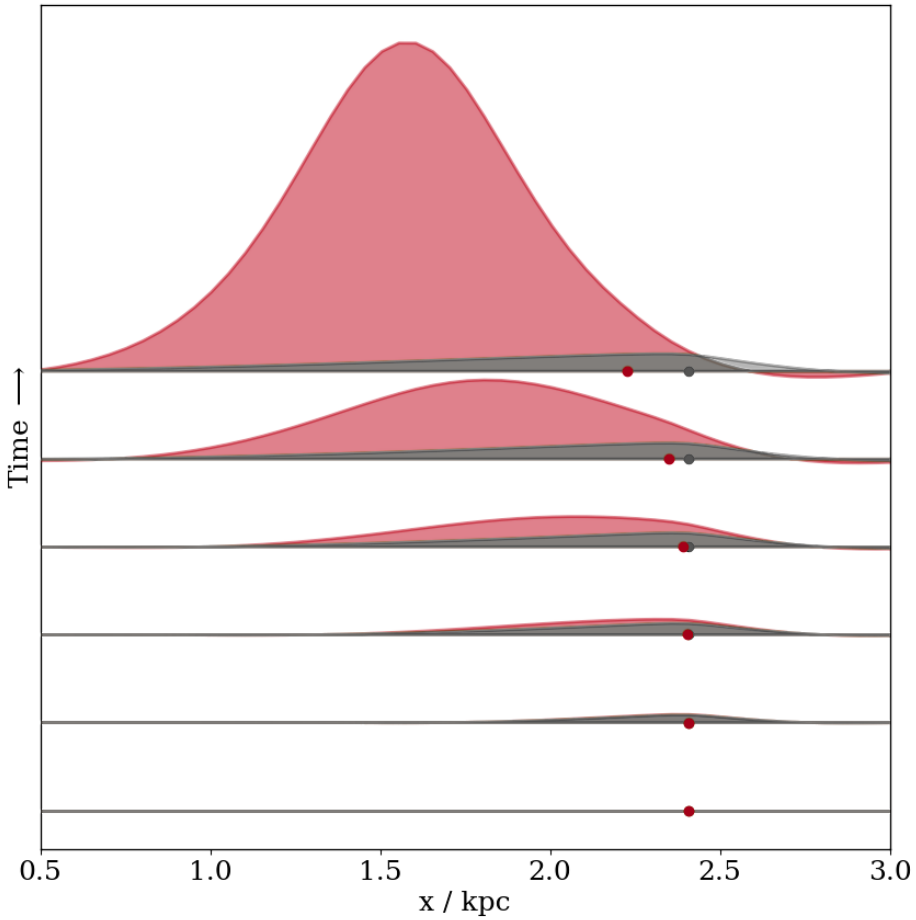

Figure 5.5: Time evolution of a gravitational wake behind the test mass (red), compared with simulation result without self-gravity (dark gray). With all gravitational interactions enabled the overdense wake undergoes collapse, and the mass falls backwards (in the comoving frame) into the resulting potential.

frame in which only the black hole is moving initially. In both cases we find good energy conservation, but the total amount of energy is not invariant under the Galilean transformation. In the lower plot we see that energy conservation improves with resolution as we would expect. Conservation appears to be better in comoving frame. However, this is a byproduct of the axion flow carrying more kinetic energy than the moving mass, rather than a physical distinction.

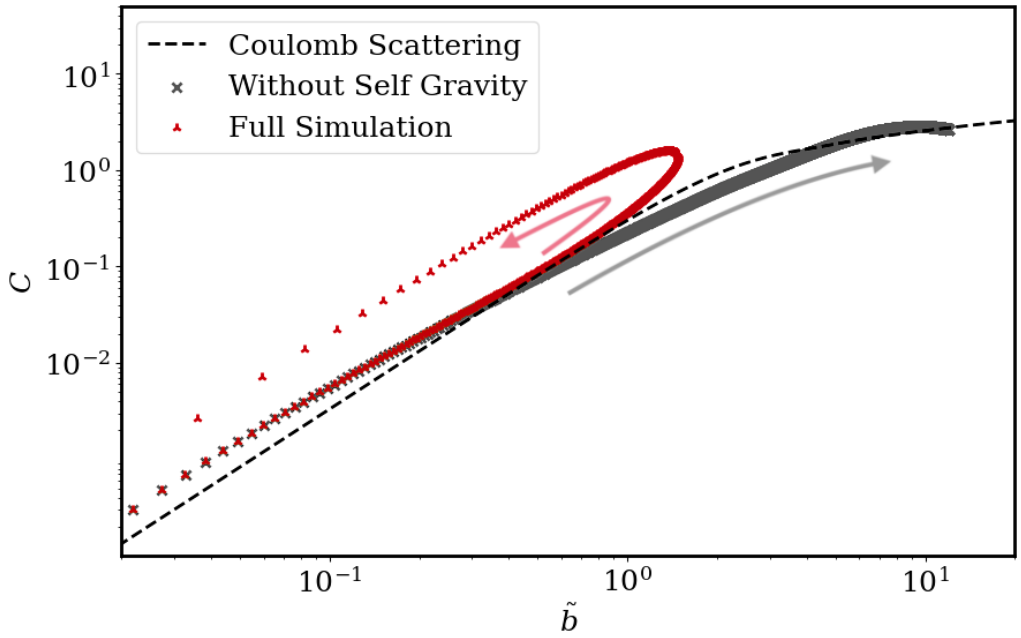

Figure 5.6: Dynamical friction coefficient C with gravitational backreaction for a representative case (red), compared with a simulation where backreaction is neglected (black). Initially, $\tilde{b}$ tracks the perturbative solution and the increases as the collapse begins; the decreasing velocity reduces the de Broglie wavelength and $\tilde{b}$. The solid arrows represent the flow of time in each scenario.

Fig. 5.8 shows the dependence on mesh resolution and the Plummer radius. We see that decreasing the Plummer radius increases the friction and decreases stopping distance, as expected [45]. We also verify that a subgrid Plummer radius can be chosen without inducing numerical instability. Conversely, if we fix the Plummer radius relative to the grid spacing, decreasing N effectively makes the potential more diffuse, and stopping time increases as N is reduced. However, one can extrapolate to the continuum limit without difficulty.

When the self-gravity term in the Schrödinger-Poisson equation is small the Coulomb scattering approximation is typically sufficient to compute the force on a moving particle. However, once the wake becomes gravitationally unstable the particle rapidly slows down. To illustrate this we surveyed

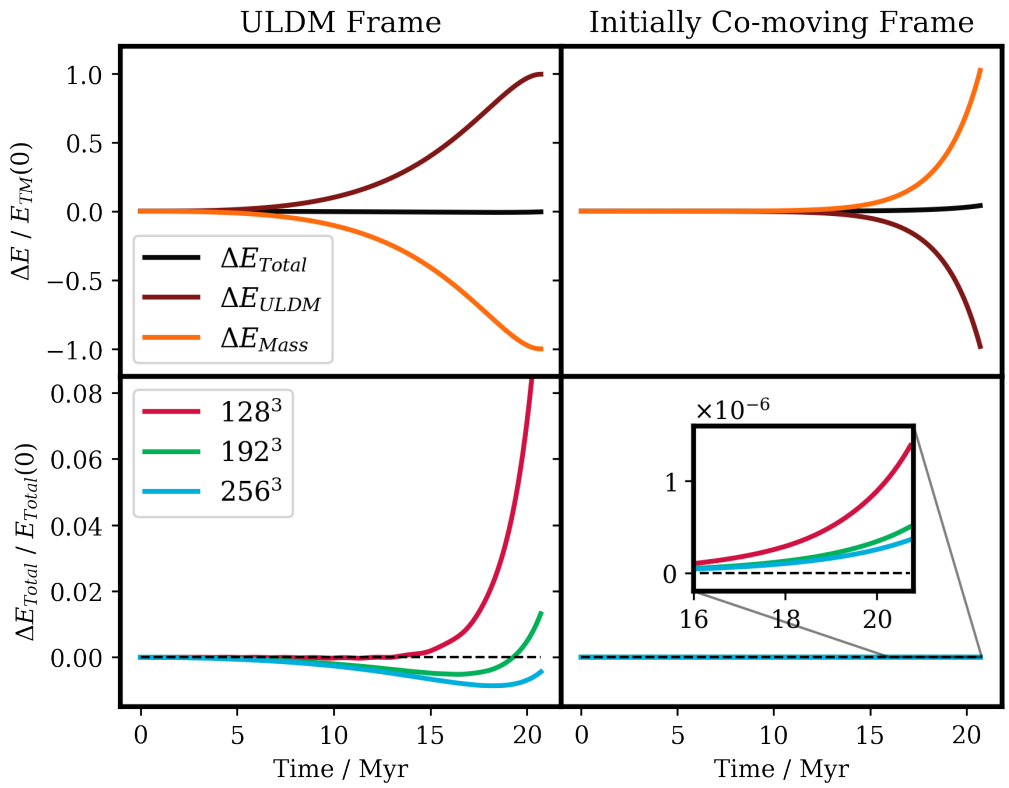

Figure 5.7: Upper Row: The energy transfer between the travelling mass and ULDM, in units of the object's initial kinetic energy in the ULDM frame, with $N = 256$. After 20 Myr the mass is sensibly at rest. **Lower Row:** Net change in system energy for $N = 128$, 192 and 256.

a range of initial particle masses between 0.1 and 100 million solar masses and ULDM densities between 10^5 and $10^8 \rho_{\text{crit}}$. In almost all cases the moving mass came to halt after traveling less than 3.5 kpc and within 100 Myr. For large black holes in a very dense ULDM background the stopping distance can be on the order of $\mathcal{O}(10)$ parsecs. This result is illustrated in Fig. 5.9.

Physically, however, this scenario is unlikely to be encountered in practice - the densest parts of a ULDM are the central soliton, which need not behave in the same way as a uniform ULDM background. Conceivably conditions close to this scenario could exist in the early universe (recall-

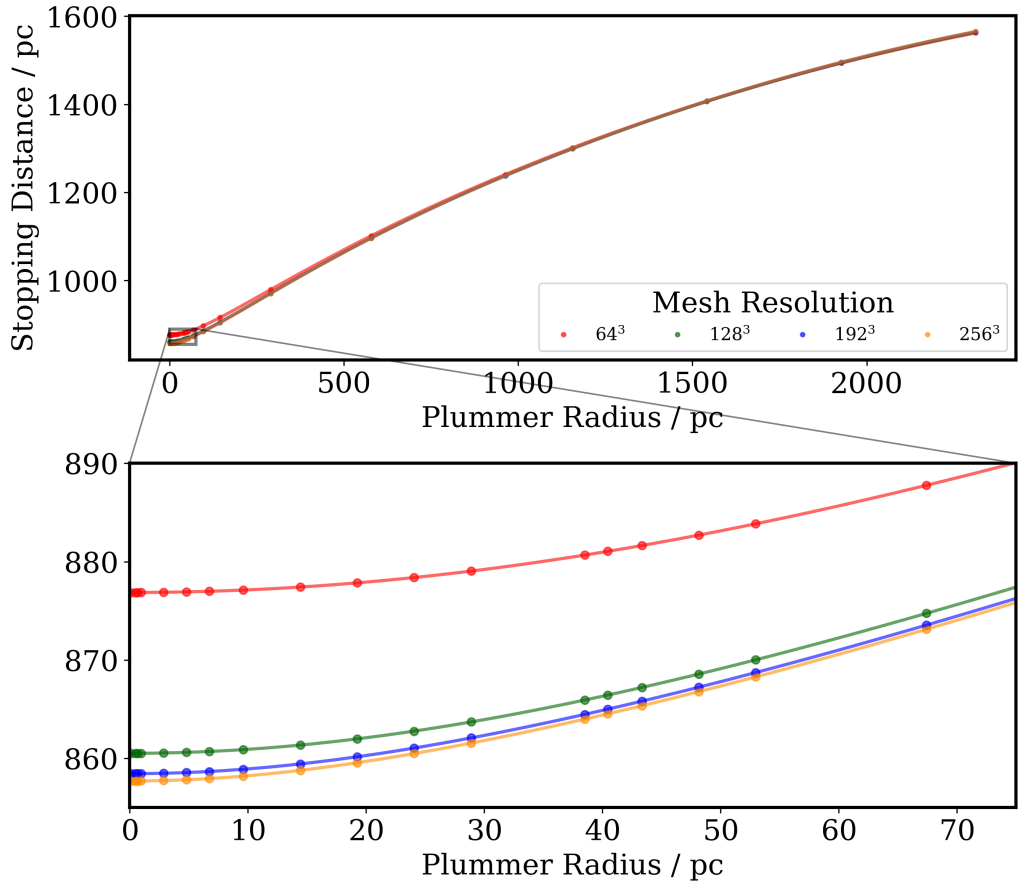

Figure 5.8: The stopping distances of the $10M_\odot$ object as a function of its Plummer Radius, simulated at 4 mesh resolutions.

ing that $\rho \approx 10^9 \rho_{\text{crit}}$ at recombination) but in that scenario the moving object would necessarily be a primordial black hole, formed in a much earlier epoch. Moreover, in this scenario axion collapse may lead to the formation of a black hole, as studied in Ref. [76].

5.4 Physical Configuration

We now consider a mass moving in an initially circular orbit around (and inside) a Schrödinger-Poisson soliton and analyse the decay of its orbital radius and energy. SMBH dynamics after a galactic merger are obviously a

key motivation for this work but we focus on a single, displaced SMBH in this initial treatment.

The simulations in this Section make use of a soliton with the parameters

$$M_{\text{Soliton}} = 1.2 \times 10^7 M_\odot,$$
$$m_{22} = 10,$$
$$r_{50} = 279.7\text{pc},$$

where r_{50} is the radius which encloses 50% of the soliton mass. The chosen axion mass (10^{-21} eV) is broadly compatible with current astrophysical bounds (although see [77]); the mass of the central soliton is consistent with that expected for a $\sim 10^{10} M_\odot$ halo [28, 57]. The simulations are per-

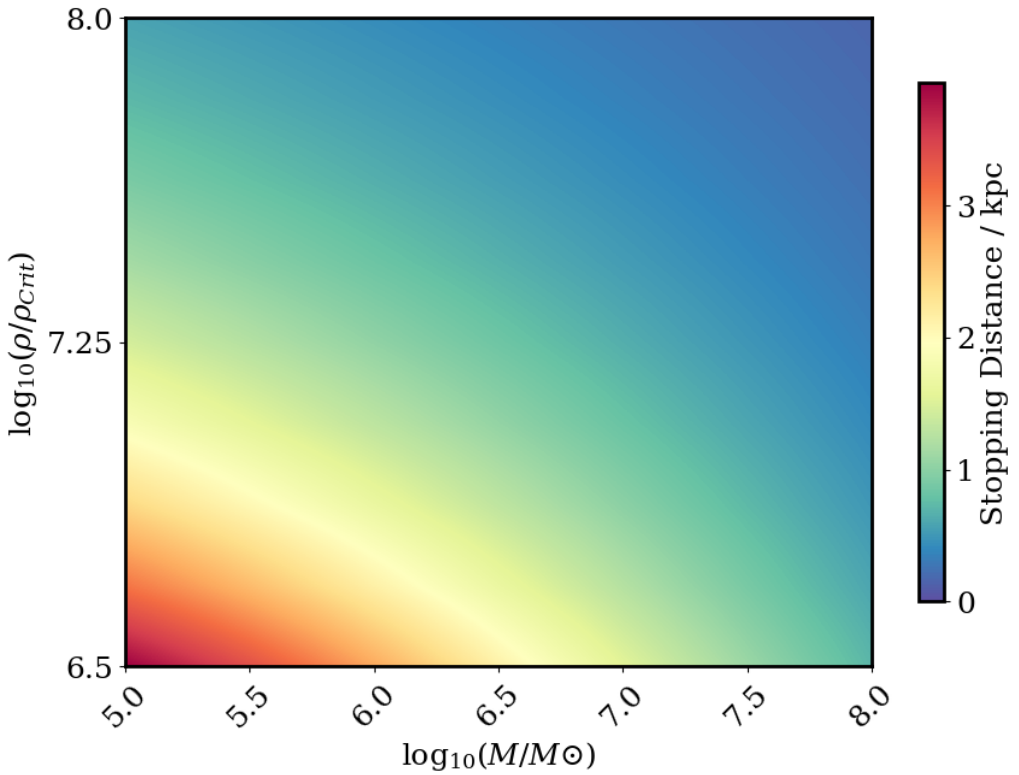

Figure 5.9: Stopping distance interpolated using 13 object masses and 9 density values, all with $v_{\text{Rel}} = 50$ km/s. The simulations were conducted at 128^3 resolution in the ULDM frame.

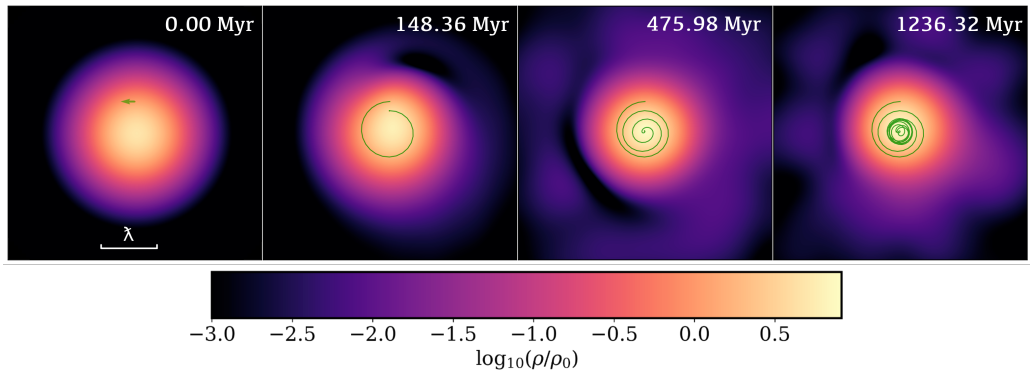

Figure 5.10: ULDM configuration in a black hole-soliton pair with an initial separation of 300pc and $M_{\mathrm{BH}}/M_{\mathrm{Soliton}} = 0.08$. Density is shown on a log scale, calibrated against the value at the initial location, $\rho_0 \approx 0.0295 M_\odot/\mathrm{pc}^{-3}$. The de Broglie wavelength is plotted for reference.

formed in a box $L = 4.5$kpc on a side and the Plummer radius is set to be half of the grid-spacing.

Our simulations begin with the black hole embedded in an undisturbed soliton. Fig. 5.10 shows the ULDM configuration at four different times for a mass ratio of $M_{\mathrm{BH}}/M_{\mathrm{Soliton}} = 0.08$. There is no obvious wake, since the ULDM background responds to both quantum pressure, and its own confining gravitational potential, but the overall soliton is disturbed by the passage of the black hole.

Fig. 5.11 shows the trajectories of two black holes (from separate simulations) with masses 6×10^4 and $9.6 \times 10^5 M_\odot$ in initially circular orbits; the more massive black hole feels a larger dynamical friction and quickly sinks towards the centre. The centre of mass is at the origin, so the more massive black hole has a smaller initial radial position.

5.5 Numerical Considerations

These simulations are performed in PyUltraLight with periodic boundary conditions; to suppress artifacts arising from interactions with the boundary the simulation volume is necessarily much larger than the soliton. However, our results are largely insensitive to the spatial resolution of the ULDM simulation and energy conservation scales as expected with resolution, as shown in Fig. 5.12.

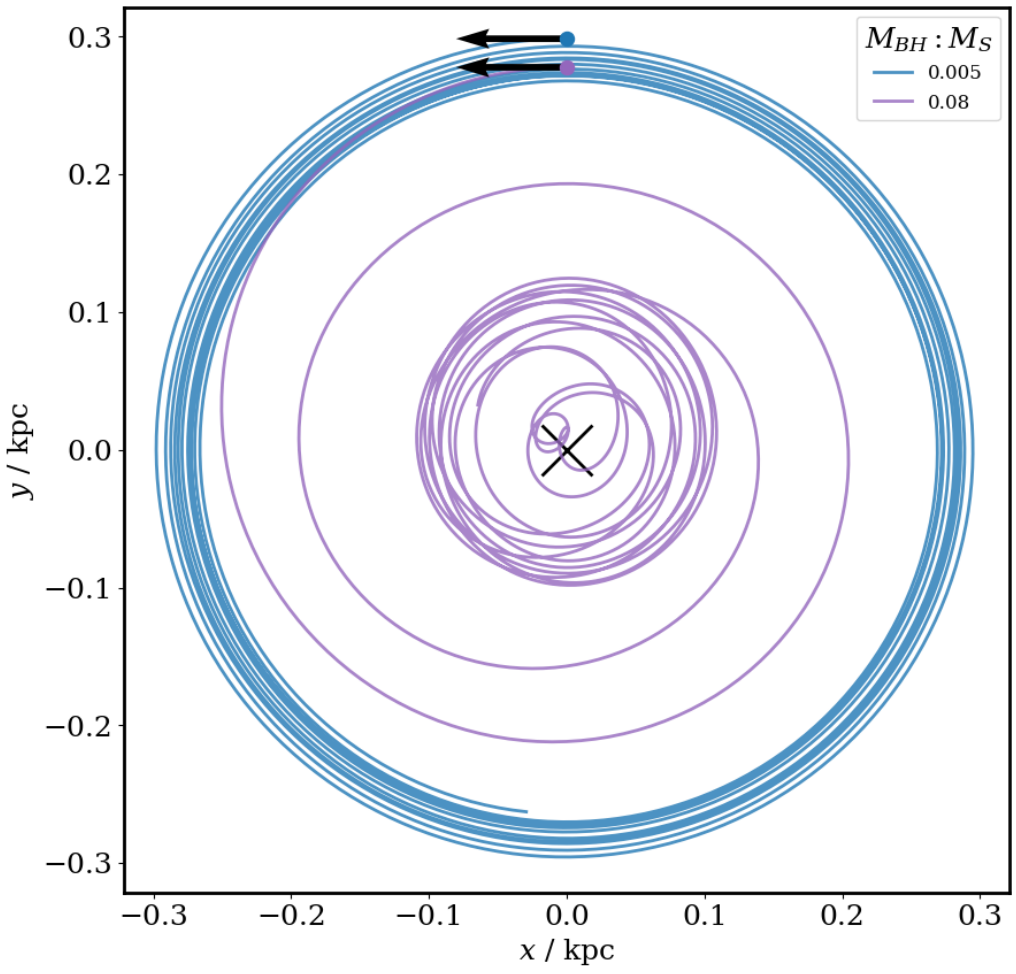

Figure 5.11: Trajectories from two simulations with initial black hole-soliton separation of 300 pc with respect to the individual system centres of mass. The orbital decay of the smaller black hole is significantly slower.

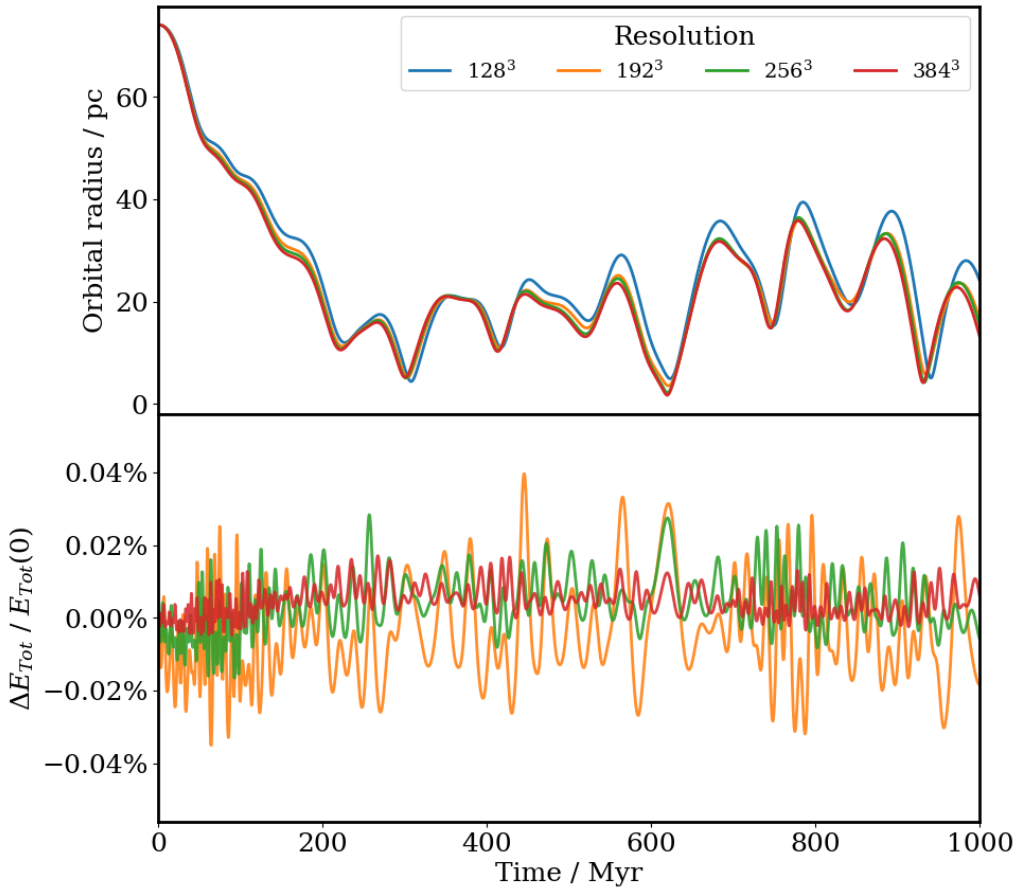

Figure 5.12: The black hole trajectory (top) and energy conservation (bottom) is shown for a mass ratio of 8% and an initial separation of 80pc for a range of resolutions.

The resolution-independence of these simulations is perhaps surprising, given that the whole trajectory in Fig. 5.12 fits into a region only a few mesh grids across for $N = 128$. However, this welcome result makes physical sense given that dynamical friction arises from a collective interaction between the black hole and the overall soliton, in contrast to drag forces associated with the mechanical displacement of a medium which are thus largely local phenomena. Consequently, provided the soliton is adequately resolved our simulations quickly reach a resolution-independent limit as N is increased. Recall too that the black hole position varies continuously with the lattice on which the wavefunction ψ is obtained. With $N = 384$, lattice

points are about 11pc apart, which is on the order of the minimum radial separation attained after the black hole has sunk toward the centre of the soliton.

5.6 Dynamical Friction

Fig. 5.13 shows the trajectories for five black hole masses and two different starting radii. The black holes all initially sink toward the centre but their kinetic energies need not decrease monotonically, due to their interactions with the newly disturbed soliton.

For circular motion the dynamical friction applies a torque on the moving mass, which gives the rate of change in the angular momentum. This implicitly defines a (rough) timescale for the orbital lifetime [57]

$$\tau \equiv \frac{\mathcal{L}}{r|F_{DF}|} = \frac{1}{C}\frac{\mathfrak{M}(r)^{3/2}}{4\pi\rho M\sqrt{Gr^3}}, \tag{5.14}$$

where $\mathcal{L}$ is the initial orbital angular momentum and $\mathfrak{M}(r)$ is the ULDM mass inside the radius r. We invoke Equation 5.11 to write

$$C \approx \frac{1}{3}\tilde{b}^2 \approx \frac{1}{3}\frac{Gm^2 r\mathfrak{M}(r)}{\hbar^2}. \tag{5.15}$$

which yields

$$\tau \approx \frac{3\hbar^2\mathfrak{M}(r)^{1/2}}{4\pi m^2\rho(r)M\sqrt{G^3r^5}}, \tag{5.16}$$

where we have explicitly denoted the density is function of r. Hui *et al.* [57] assume that the black hole is near the centre of the soliton and replace ρ with its maximum value; after this substitution it is immediately clear that $\tau \to \infty$ as $r \to 0$.

For a particle with mass M_{BH} orbiting this specific soliton at r_{50} the resulting timescale is

$$\tau \approx 160.18 \text{ Myr} \left(\frac{10^6 M_\odot}{M_{\mathsf{BH}}}\right), \tag{5.17}$$

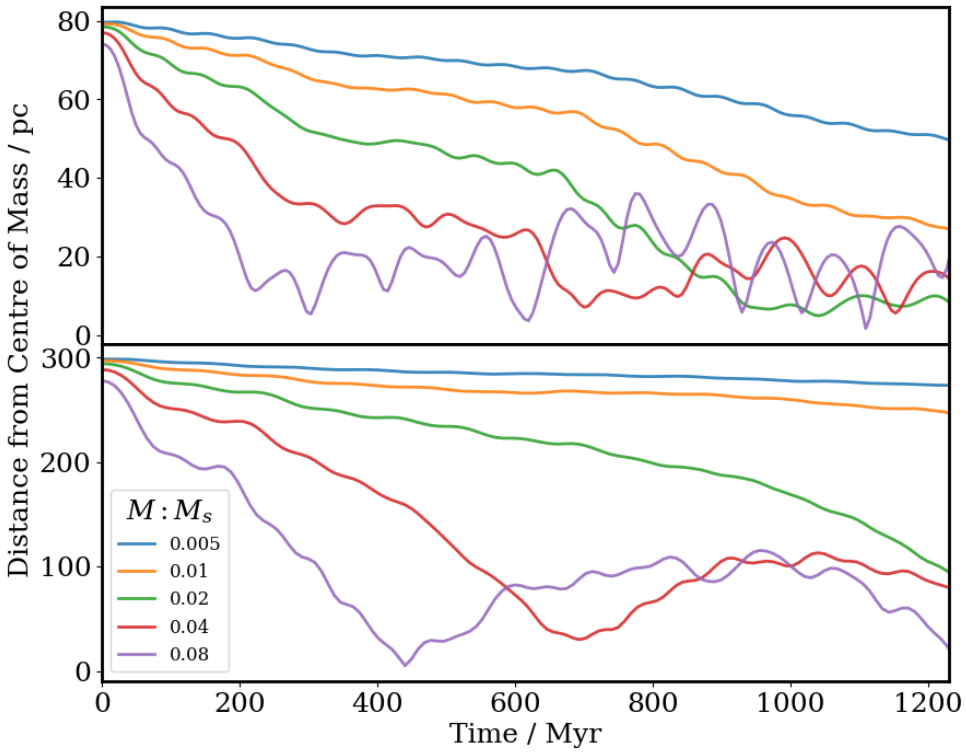

Figure 5.13: Black hole orbital radii for five mass ratios. The initial radii are 80 and 300 pc in the upper and lower panels respectively; all simulations run for 1.2 billion years.

recalling that $10^6 M_\odot$ is 8% of the soliton mass, the largest ratio we consider. Fig. 5.14 plots the characteristic timescale for a range of masses and radii, rescaled by $M_{\mathsf{BH}}/10^6$. As noted above, τ diverges at small r, since the circular velocity decreases at the centre of a spherical mass distribution, and likewise at large r when the density of the medium and and velocity both decrease with radius, but it is roughly constant for intermediate radii.

The derivation of the timescale in Equation 5.16 implicitly assumes a linear and steady decrease in angular momentum but the simulated black hole orbital radii are clearly non-monotonic. We obtain an empirical timescale for comparison purposes from the interval over which the black hole angu-

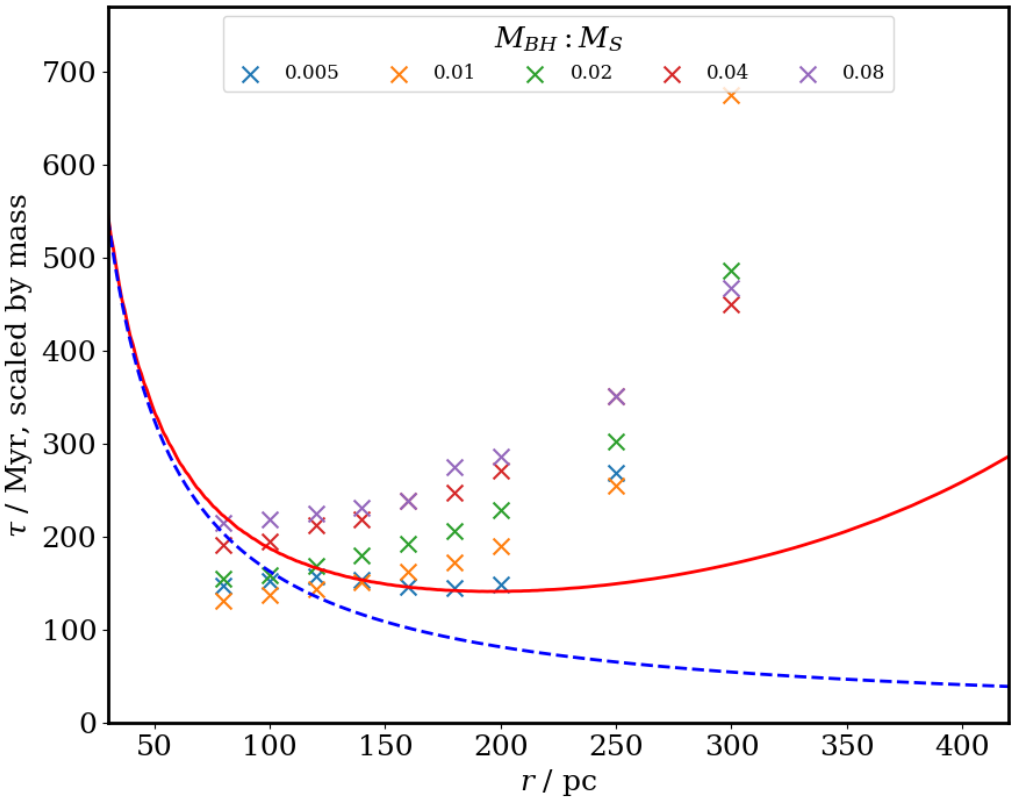

Figure 5.14: Orbital decay timescales for a $10^6 M_\odot$ black hole. The solid curve is based on Equation 5.16; the dashed curve results from fixing the density to the central value. The data points show the timescales obtained from simulations, scaled by $10^6 M_\odot / M_{\mathrm{BH}}$.

lar momentum with respect to origin decreases by 20%[2], and then rescale to the obtain the projected time to reach $L = 0$.

There is reasonable agreement between our dynamical estimates and the computed value of τ, given that it is, at best, an indicative value rather than a detailed prediction. Consequently, these results can be seen as a numerical verification of the semi-analytic treatments of the dynamical friction experienced by point masses interacting with ULDM solitons, even through the classical wakes seen in the previous Section do not form in these systems.

[2]In the simulations with the smallest black holes starting from the largest radii this threshold is never actually reached; for these cases we extrapolate.

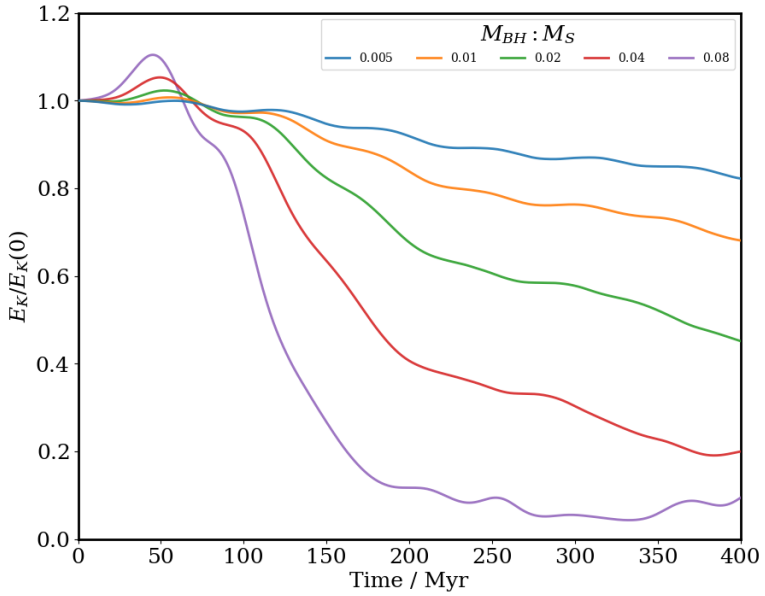

Figure 5.15: Kinetic energy as a function of time (relative to the initial value) for black holes with an initial radius of 80 pc.

5.7 Soliton Backreaction

In principle, the approximation in Equation 5.16 could be improved by integrating the instantaneous torque to yield the time taken to move between any two given radii. This would be less valuable in practice, given that in many cases the orbits are far from circular. For our chosen configuration, the black hole faces a force opposed to its initial velocity causing it to "fall" toward the centre, accelerating as it does so, as illustrated in Fig. 5.15. More massive black holes follow a clearly spiral trajectory toward the centre, as seen in Fig. 5.11, and can undergo effectively stochastic motion upon their arrival in the central region of the soliton. This motion resembles the "reheating" experienced by a massive particle when it is introduced to the centres of an already excited soliton [78].

The individual components of the total energy for a simulation with $r_0 = 300$ pc and $M_{\text{BH}}/M_{\text{Soliton}} = 0.08$ are shown in Fig. 5.16. The overall

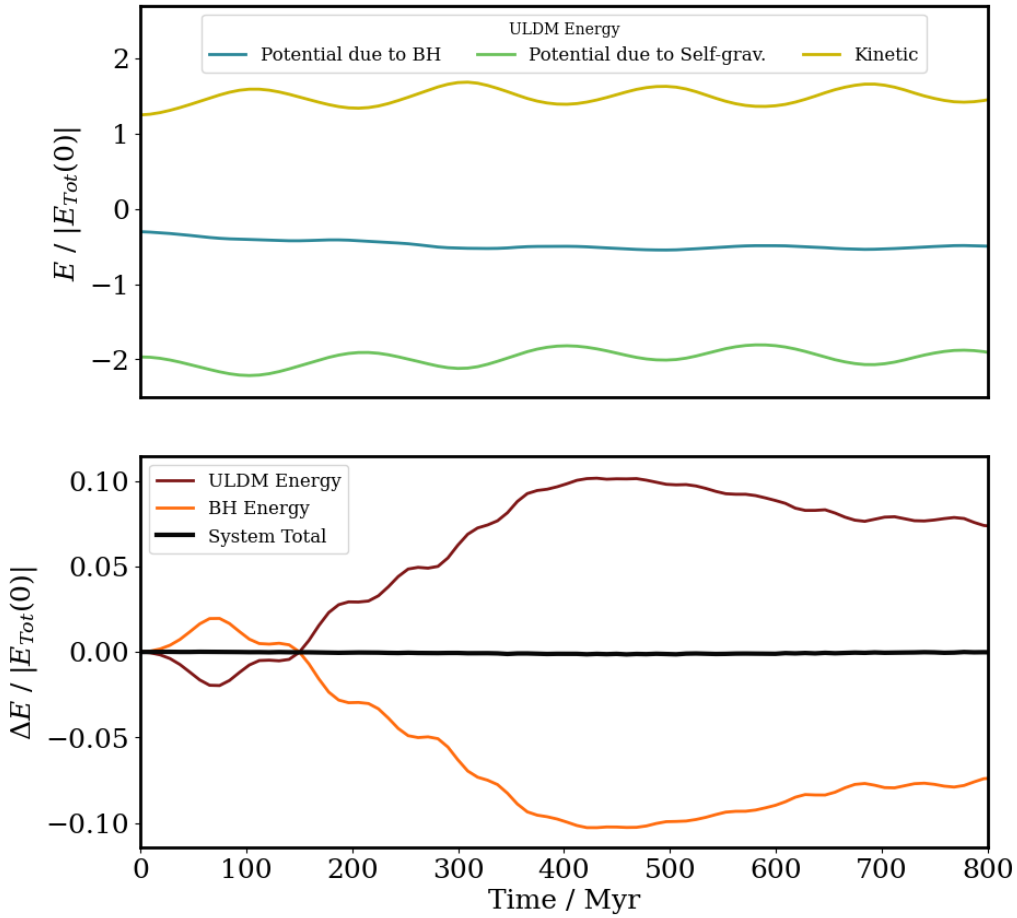

Figure 5.16: Components of the total energy for a simulation with $r_0 = 300$ pc and $M_{\text{BH}}/M_{\text{Soliton}} = 0.08$. The top panel shows a component-wise breakdown of the ULDM energies, relative to the system's total energy. The bottom panel shows the changes in ULDM, BH, and total energies.

energy of the black hole decreases as it sinks towards the centre of the soliton. However, we also see the onset of a persistent oscillation in the soliton itself, even though its total energy is constant, outside of the energy injected by the moving black hole. This is attributable to our chosen initial configuration which puts a stationary, spherically symmetric soliton in the potential of an adjacent black hole. This is a small perturbation to the overall gravitational potential of the soliton, but it means that it is no longer in its ground state configuration. The soliton is also relatively "compressible" – the overall change in its self-potential is several times larger

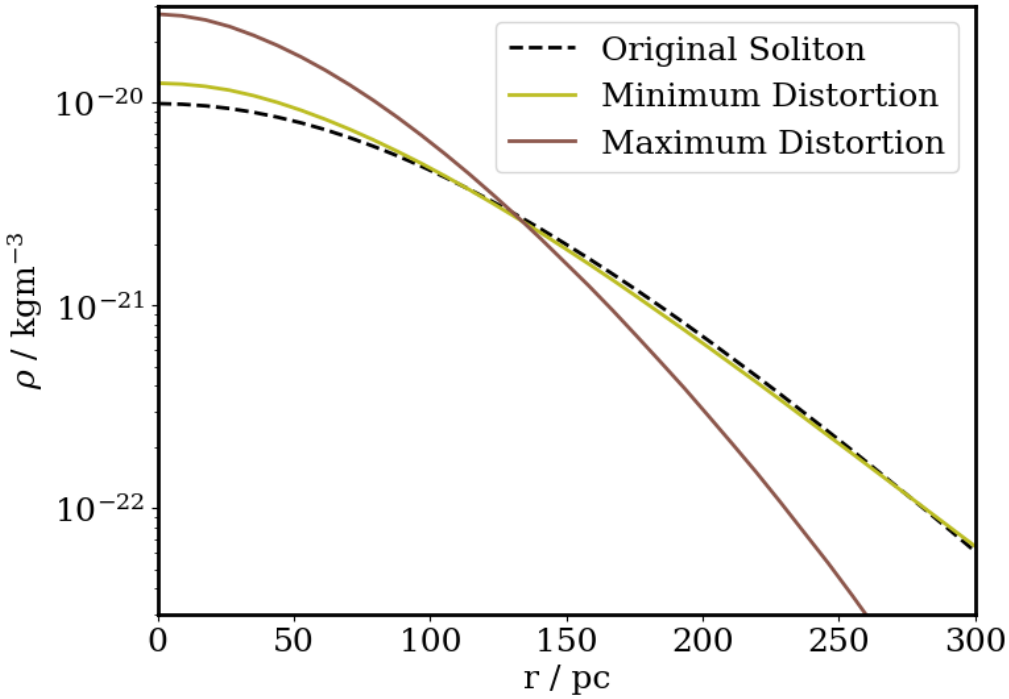

Figure 5.17: An idealised representation of the ULDM soliton's breathing behaviour, as excited by our massive particle of $8\%M_S$, initially orbiting 80 parsecs away from the soliton's centre. The soliton's density profile oscillates between the two solid lines on this graph, while the dashed line corresponds to the unperturbed soliton profile. The solid-line profiles were obtained from the simulations, via radial averaging around the ULDM centre of mass.

than the potential energy of the black hole. The impact of the breathing mode on the potential is illustrated in Fig. 5.18, which shows the trajectories of black holes for a series of different starting radii.

Physically, this is a breathing mode, where a soliton's radial density oscillates, as illustrated in Fig. 5.17. Although the oscillation an orbiting black hole excites likely lacks perfect spherical symmetry, given the off-centre position of the external gravitational field. The oscillations persist on timescales much longer than those over which the black hole orbit decays as there is no mechanism to remove this energy from the system. Moreover, they persist even if the black hole is deleted from the simulation after it has completed a number of orbits.

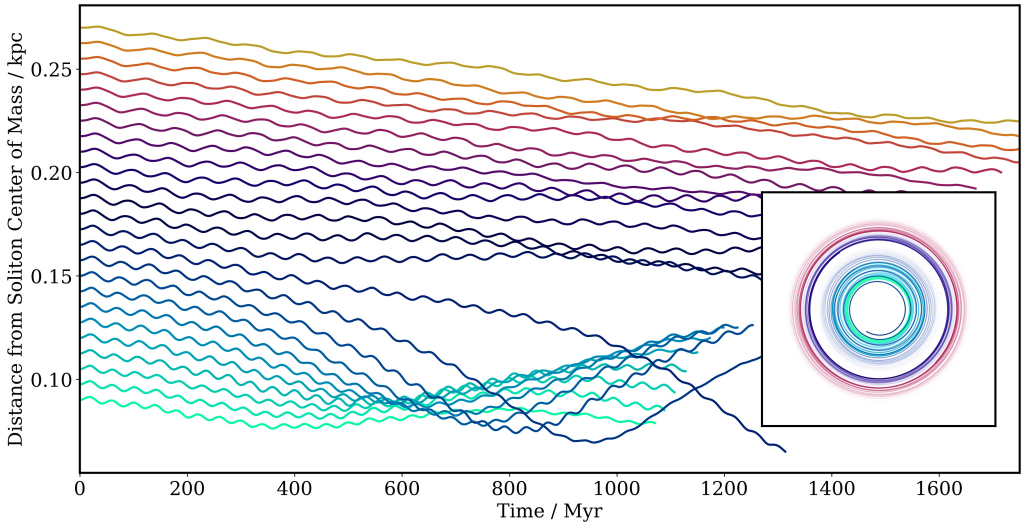

Figure 5.18: Radius as a function of time for a $0.5\%M_S$ black hole

Beyond the stochastic motion seen at the centre of the soliton, for certain parameter choices the breathing mode "reheats" black holes orbiting at some distance from the centre. This is illustrated in Fig. 5.18, which shows a set of trajectories in which the radial distance of the black hole steadily increases over a number of orbits. Physically, this behaviour appears to be driven by a resonance between the soliton breathing mode and the orbital period; a similar situation is described in Ref. [79]. It is more pronounced for small black holes (since it has to work against the dynamical friction, which increases with mass) and depends non-linearly on the initial radius, which fixes the specific form of the breathing mode. This behaviour (which is reminiscent of a stone skipped across a pond) is responsible for much of the scatter seen in Fig. 5.14.

We have presented simulations of (large) point masses interacting with ultralight dark matter (ULDM), and focused on two scenarios – a uniform background of ULDM and the soliton found at the centre of a ULDM galactic halo. In the former, the wake left by the moving point mass can collapse under its self-gravity, dramatically enhancing the dynamical friction. We

then simulate the dynamics of a super-massive black hole in an initially circular orbit about (and inside of) a ULDM soliton. The black hole sinks towards the centre of the soliton. We confirm simple estimates of the relevant timescale within $\mathcal{O}(1)$ but also see novel "stone skipping" trajectories at certain large initial radii, where the black hole does not monotonically approach the centre. Once near the centre, black holes undergo stochastic motion, migrating back out to radii of 10s of parsecs in the examples we study. Both the stone skipping and the stochastic trajectories are driven by excitations to the soliton sourced by its interactions with black hole.

Astrophysically, there may be few circumstances in which a point mass will encounter a uniform and otherwise unperturbed background, although one can imagine possible scenarios involving primordial black holes or very early universe physics [34, 36]. Conversely, a massive object inside a Schrödinger-Poisson soliton maps directly to the dynamics of SMBH at the centre of a galactic halo, and these systems have a wide range of astrophysical consequences. Identifying the ways in which the distinctive properties of ULDM modify our expectations for these interactions could be key to testing the scenario, given the potential of pulsar timing experiments [80, 81] and the upcoming LISA mission [82].

The present results complement suggestions by Bar-Or *et al.* [58] that black hole binaries will be "heated" by interactions with a granular ULDM halo. In the present case the ULDM is initially uniform and large scale oscillations are induced as the soliton-SMBH system orbits its common centre of mass. In a post-merger halo, the central soliton may be far from its ground state, suggesting that these effects might be substantially enhanced in astrophysical settings, resulting in the outward diffusion of light objects residing in the centre of the soliton [78]. In addition, the coupling and impulsive heating associated with a single SMBH-soliton interaction could be

analysed in detail using eigenstate expansions of the soliton potential [29], facilitating the semi-analytic treatment of these systems.

Perhaps surprisingly it seems that the interactions between ULDM solitons and the black hole motion are well-modelled even at low grid resolutions. This rather fortunate outcome arises from the difficulty of establishing large density gradients in ULDM on scales significantly shorter than the de Broglie wavelength; the black hole effectively interacts with the overall soliton, rather than just the matter in its immediate locality. That said, there is clear value in high-resolution simulations. However, we are obliged to simulate a large volume to prevent the soliton from being disrupted by boundary effects so the black hole trajectory is confined to a small fraction of the total simulation region. Consequently, implementing the combination of a hard N-body solver coupled to a Schrödinger-Poisson solver in a scheme that supports adaptive mesh refinement (e.g. Ref. [61]) is a logical next step.

We see interesting interactions at larger radii driven by "breathing modes" of the soliton excited by its interaction with the black hole. In these cases black holes at relatively large distances do not sink monotonically toward the centre of the soliton. These "stone skipping" trajectories differ from previous work on the dynamical friction in ULDM (e.g. [45, 58] in that they represent interactions between the point mass and the overall soliton, and point to further novel behaviours associated with SMBH-ULDM dynamics.

The breathing modes driving the stone skipping solutions are reminiscent of *quasinormal modes* arising from displacements of a Schrödinger-Poisson system away from its equilibrium configuration [83, 29]. These analyses can presumably be generalised to the asymmetric states seen here, allowing a more quantitative understanding of these trajectories.

5.8 Tidal Stripping by a ULDM Soliton

The scenarios we analysed in the previous section have neglected the internal dynamics and structure of the massive particles themselves. In doing so we left an interesting physical effect out of the picture, the tidal force. The tidal force arises when different parts of an object experiences differing gravitational field strengths. Using the ability to evolve entire particle ensembles built in $\mathrm{PyUltraLight}$, we can sketch a scenario where a globular cluster scatters off a soliton, and compare simulations with and without ULDM backreaction. Future modifications to improve the realism of this model are also outlined.

5.8.1 BH-Dominated Globular Cluster

We replace the single smoothed particle in the previous section with a "cluster", a 1000-particle structure with a central object that dominates in mass ($\sim 95\%$). The other particles are randomly distributed around this central object in 3 dimensions, and are given small random 3-velocities. The cluster is set up with a radius of 60pc. And, in order to maximise the tidal effects, the cluster is positioned so the impact parameter is equal to the soliton's HWHM. Figure 5.19 sketches the initial condition on the plane $z = 0$.

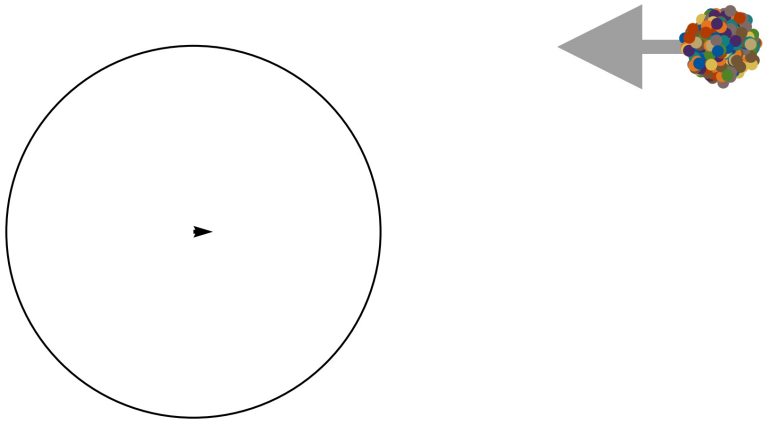

Figure 5.19: Sketch of the initial conditions on the $x-y$ plane. The soliton's velocity is set up so that the system centre of mass stays in the middle of the simulation domain. The arrows arising form individual particle velocity dispersion are omitted.

Other relevant parameters are,

$$
\begin{aligned}
M_{\text{Soliton}} &= 10^7 M_\odot, \\
M_{\text{Cluster}} &= 8 \times 10^5 M_\odot, \\
\sigma_{0\text{Cluster}} &\approx 2\text{km/s} \\
m_{22} &= 10, \\
b = r_{50} &= 284\text{pc}, \\
x_0 &= 800\text{pc}, \\
v_0 &= 10\text{km/s},
\end{aligned}
$$

where σ_0 is the initial velocity dispersion, x_0 is the initial separation in the x direction, and v_0 is the initial relative speed, which we set up to be parallel to the x axis. It is also assumed that the stars reach a reasonable degree of equilibrium by the time approach happens.

The first simulation of the model was conducted at a resolution $N = 256$ for a duration of 1 gigayear. A corresponding simulation without ULDM

backreaction is also implemented, with the soliton placed at the origin at rest and the initial positions and speeds of the particles adjusted suitably so the particles in these two runs can be identified and directly compared.

Figure 5.20 shows the trajectories of all particles in the $x - y$ plane from the full simulation, while highlighting the trajectory of one star. Figure 5.21 shows the trajectories of three representative stars with and without ULDM backreaction, alongside the central black holes. We can also see that after the encounter with a soliton, the cluster simulated with backreaction has a larger variance in positions and velocities, suggesting it has been heated and distorted to a bigger extent. A sizeable proportion of stars are stripped from the cluster by the ULDM wake, seen as the small region with an overdensity of 10^2 code units in Figure 5.20. This is reminiscent of the heating effect on stellar streams when they encounter ULDM granules.

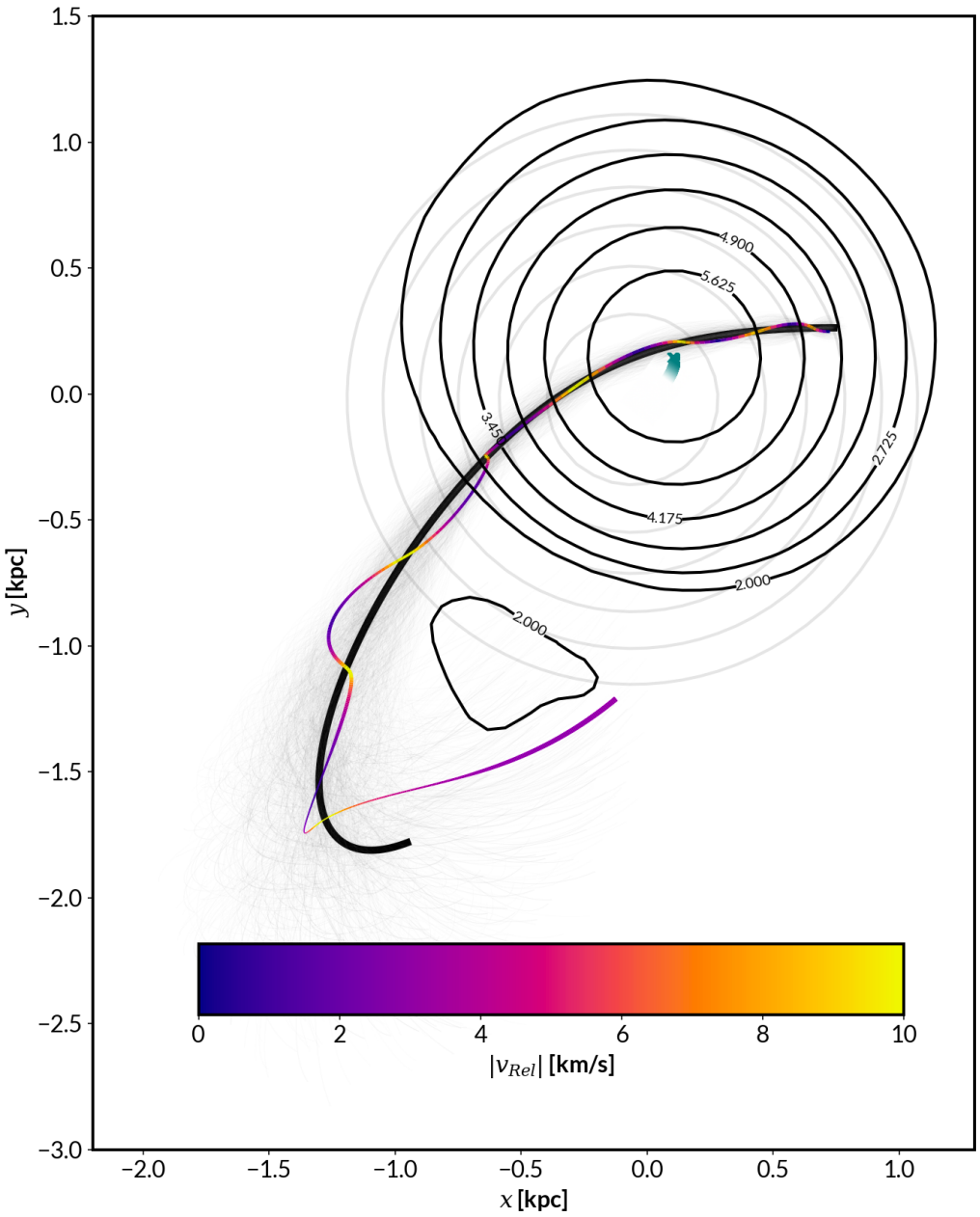

Figure 5.20: Trajectories of all simulated particles. The velocity history (measured relative to the central mass) of a representative star is mapped to colours, and the trajectory of the central black hole is plotted in bold. The ULDM density contours are given in logarithmic scale.

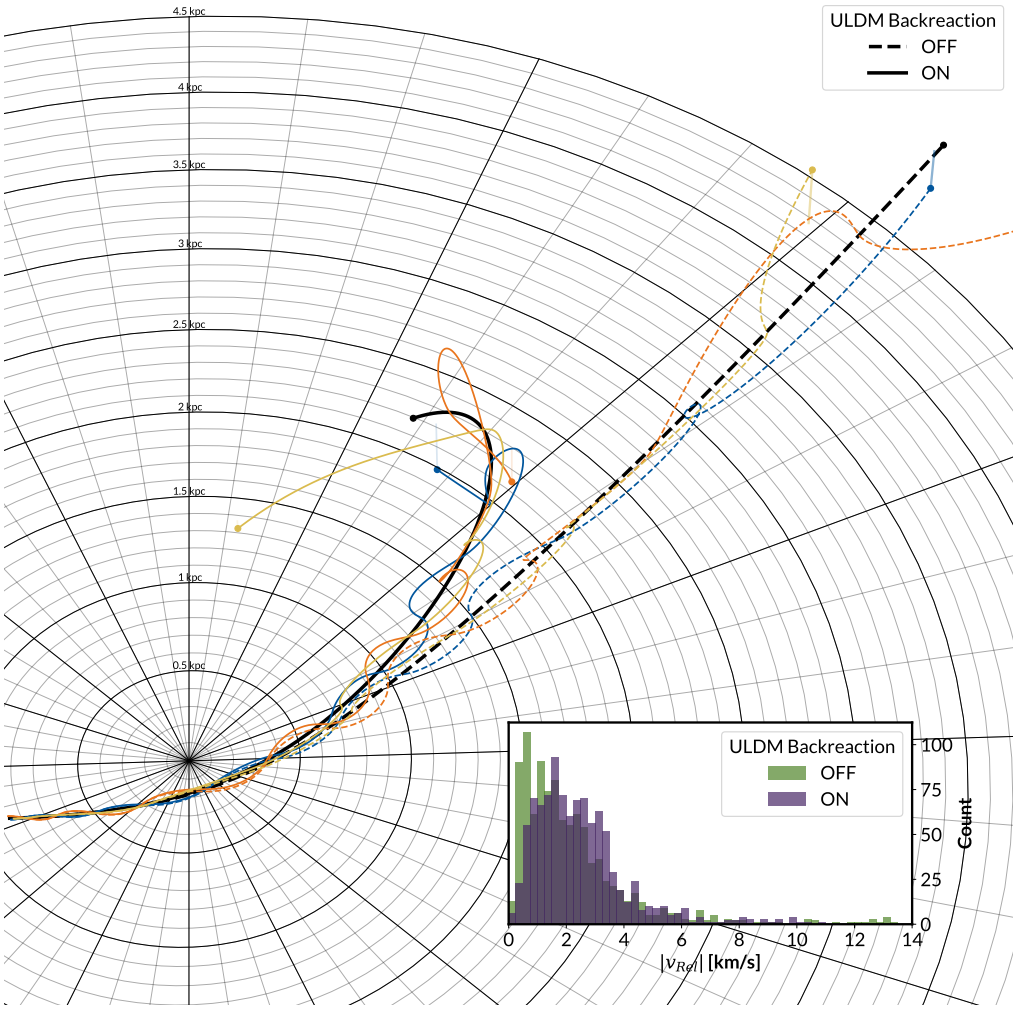

Figure 5.21: 3 dimensional view of the trajectories of 3 particles alongside their counterparts from a simulation without ULDM backreaction. The distributions of relative speeds at the end of the simulation ($t = 1$Gyr) is printed in the inset.

5.8.2 "Virialised" Globular Cluster

We modify the previous model so the 1000 stars have equal mass $m_P = 50M_\odot$, and follow the method outlined in [84] to give them initial velocities that satisfy the Virial theorem,

$$\langle K \rangle = -\frac{1}{2} \sum_{j=1}^{N} \langle \mathbf{F}_j \cdot \mathbf{r}_j \rangle \,, \tag{5.18}$$

Figure 5.22 shows the statistics of an initialised cluster in code units. The particle system is then placed in isolation and evolved for 70 Myr to check its stability. The histograms in Figure 5.22 show the initial and final distributions of positions and speed.

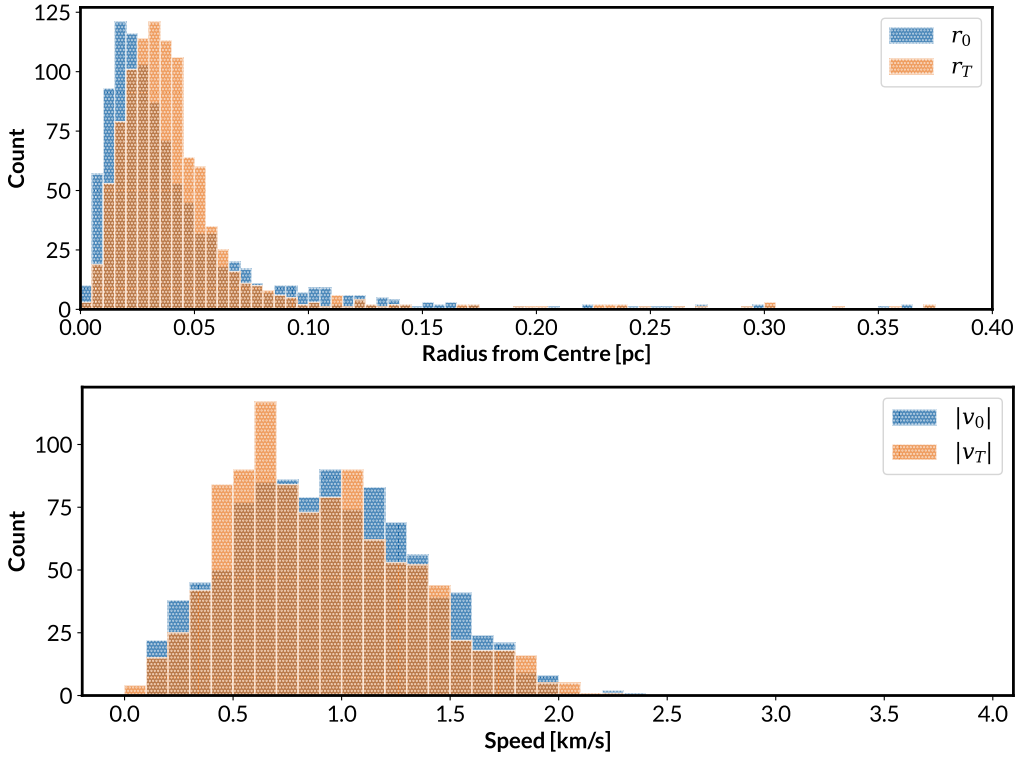

Figure 5.22: Distribution of stellar motion in the virialised cluster.

Other relevant parameters are,

$$
\begin{aligned}
m_{22} &= 10, \\
M_{\text{Soliton}} &= 10^7 M_\odot, \\
M_{\text{Cluster}} &= 5 \times 10^4 M_\odot, \\
\sigma_{\text{Cluster}} &= 0.4 \text{km/s}, \\
v_{\text{Rel,Median}} &= 0.8 \text{km/s}, \\
v_0 &= 10 \text{km/s},
\end{aligned}
$$

The resulting particle trajectories in the first simulation are presented in Figure 5.23. The conditions of the encounter are so extreme that the cluster becomes spread out after half an orbit, but the centre of mass follows a different trajectory from a single particle with the same mass as the cluster.

These simulations are a proof of concept. To further construct more realistic simulations of tidal stripping, one should start with a dynamic halo, set the cluster going in a less extreme orbit, and account for other components of the interstellar medium, such as other stars and gas. This possibility will be examined in future work.

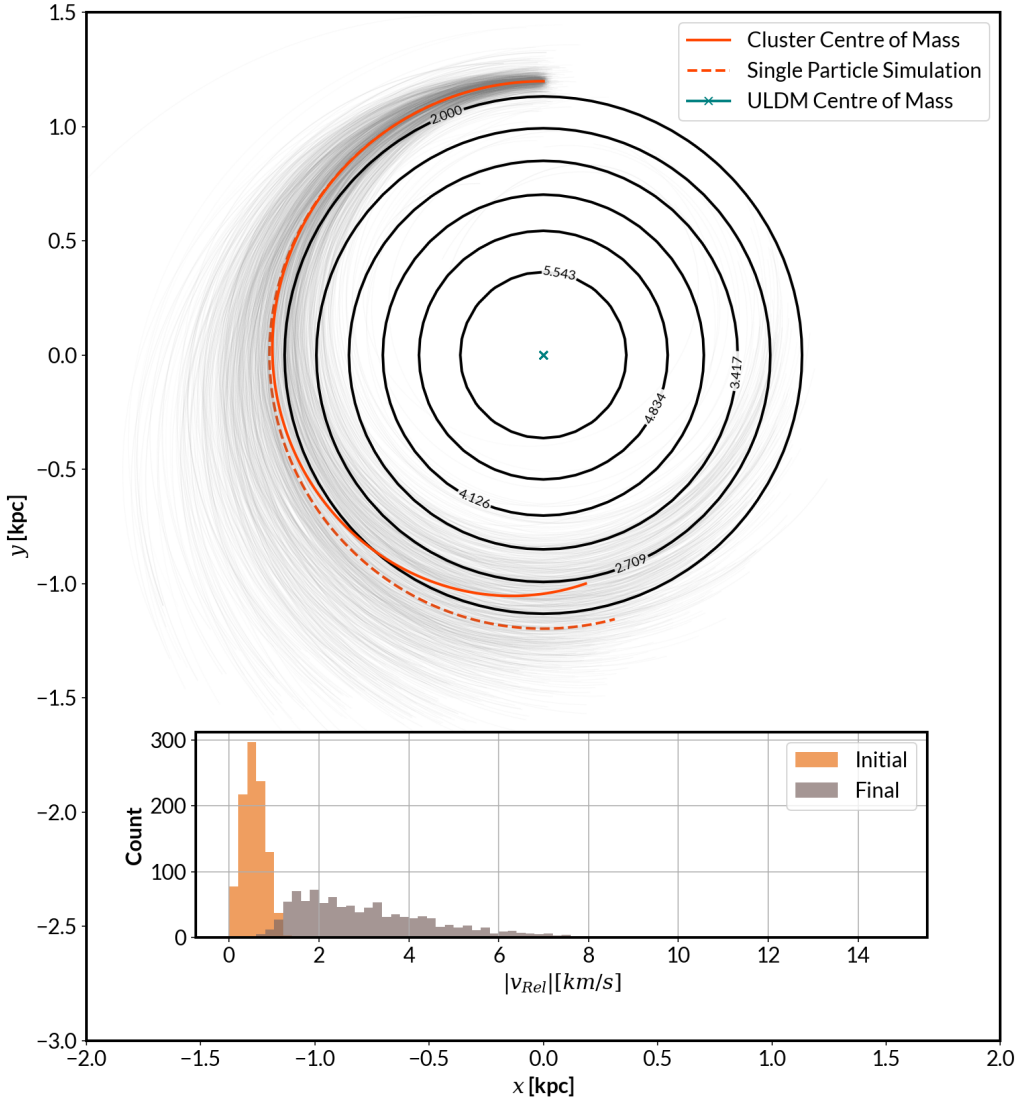

Figure 5.23: Trajectories of all simulated particles, with centre-of-mass trajectory compared with the simulation where all mass is concentrated in one particle. The ULDM density contours are given in logarithmic scale.

That all the world will be in love with night

And pay no worship to the garish sun.

William Shakespeare, *Romeo and Juliet*, Act 3, Scene 2

6

Multi-field ULDM[1]

Most of the arguments used to justify the existence of a single ULDM field do not typically predict the existence of just one field. Consequently, there is considerable motivation for considering multifield models.

We can modify our programs to account for more than one wavefunctions that interact with each other via a common Φ, calculated from the aggregate density of all fields. The time step, Δt, is set to equal the slowest required value of the set, i.e. the timescale associated with the ULDM species with the highest m_{A}.

[1]This chapter is based on [32], where simulations are conducted with modified versions of both PyUltraLight and AxioNyx. Results from AxioNyx runs (Figures 6.5 through 6.8) are due to Dr Mateja Gosenca, reproduced with permission.

6.1 Solitons: Equal Mass

The first scenario we investigate is a two-field model where the two axion species have equal mass. Each component behaves according to the Schrödinger-Poisson equations as before, but the two components only interact with each other via the combined gravitational field.

As for the test case, we present a variation of the scenario showcased in Figure 4.14. We set up two solitons that approach each other at a low relative speeds. As one would expect, this setup maintains the “quantum pressure” supporting each soliton, but turns off interference effects related to phase differences between the two solitons. As a result, the two solitons pass through each other and become asymmetrically excited. The system should eventually relax into a single soliton by dumping excitations to infinity, but our chosen boundary conditions could not support such a long simulation duration.

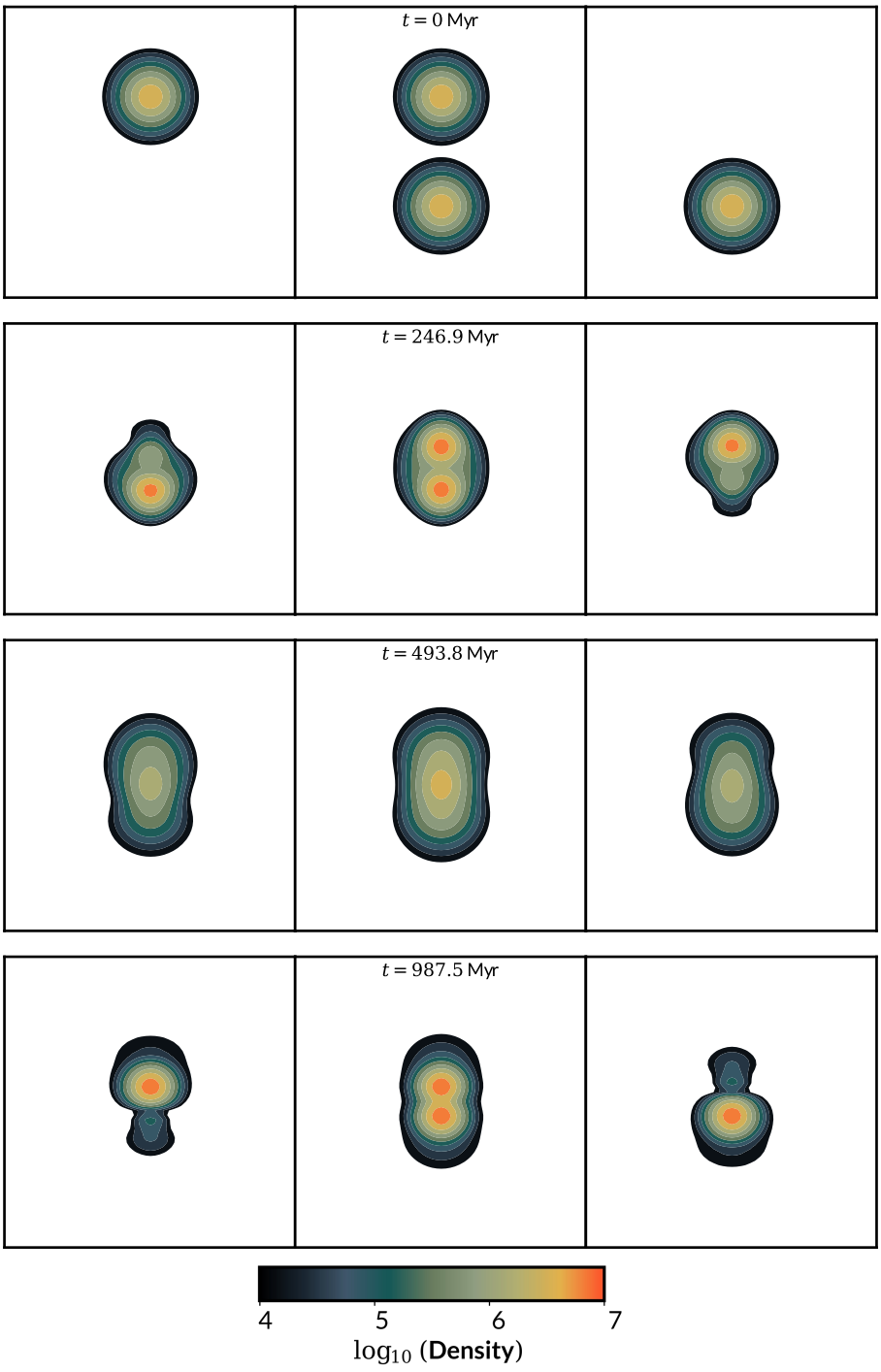

Figure 6.1: The scattering of two solitons from two ULDM species with equal m_{22}. ULDM species A is shown in the left column, B in the right column, and the centre column shows their combined density. Compared with Figure 4.14, interference effects are completely absent.

6.2 Solitons: Different Mass

For the next model, we superimposed 8 stationary soliton wavefunctions at the centre of the simulation domain from axion species whose m_{22} values range from 7 to 14. Each ULDM density distribution is scaled by a factor of $1/8$, such that the combined mass of all ULDM in the domain equals that of one soliton in a single-field simulation.

We set this system to evolve, and focus on at the time-evolution of the central density, which undergoes nonlinear oscillations shown in Figure 6.2. This is further broken down to show the contributions from each ULDM field, and we Fourier transformed the resulting time series. The heaviest ULDM species has the smallest and densest soliton by radius, and as such has more localised contribution to the gravitational field. Likewise, the lightest ULDM species oscillates at the lowest amplitude. The Fourier analysis shows that some slow-varying peaks are aligned, which suggests correlations between the different fields that develop via gravitational coupling.

Another astrophysically interesting quantity that varies with ULDM mass is the entire condensate's granularity [78, 85]. This is evident in the 2D density slices over time in Figure 6.3.

In Figure 6.4, the total[2] ($E_{GP} + E_{KQ}$) energies of each ULDM species is plotted. During the initial transient phase, the heavier axion species tended to spread outwards, and in doing so pulled the more diffuse lighter ULDM solitons inwards, setting the oscillations in motion.

Due to the scaling we applied and the external gravitational influence of its neighbours, none of the component ULDM distributions started off in

[2] E_{GP} here refers to the potential energy due to the combined gravitational field.

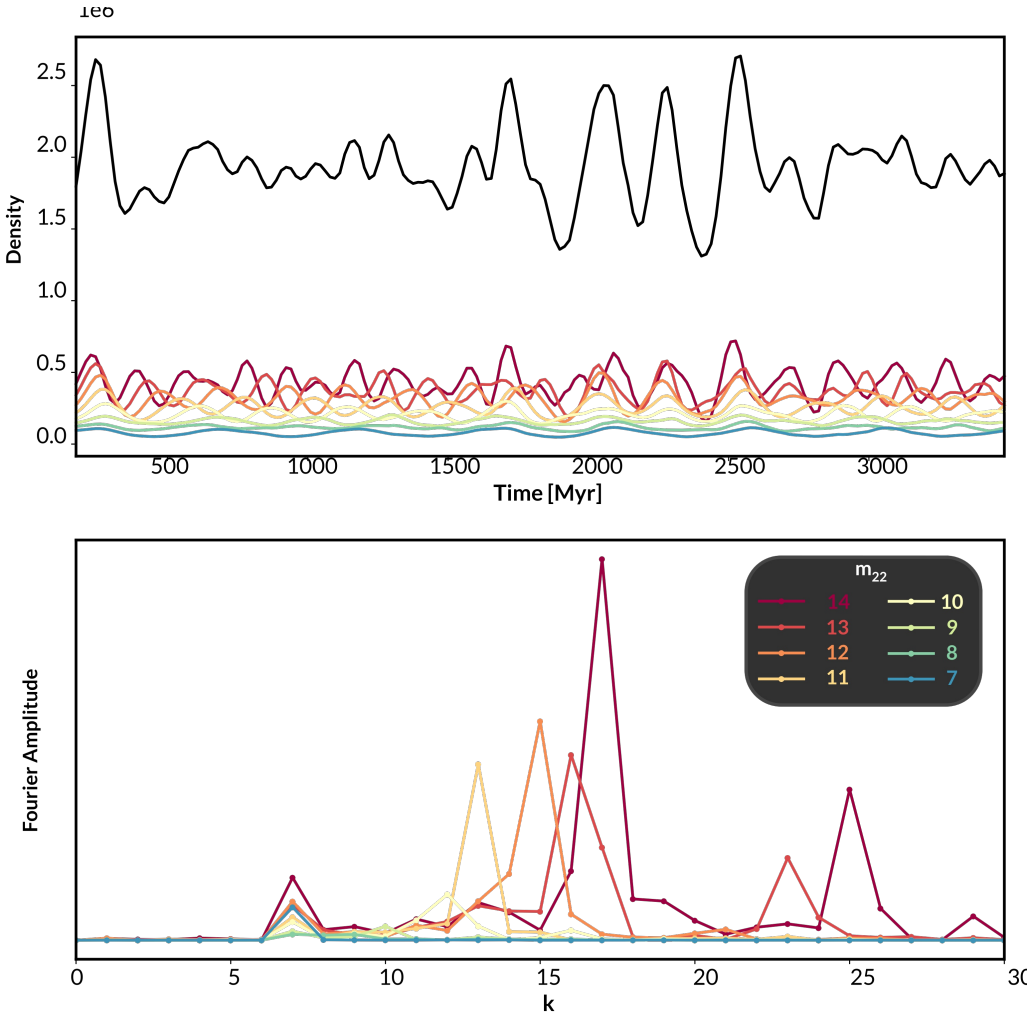

Figure 6.2: Time evolution of the central density of the 8-field soliton and the Fourier spectrum of each components' central densities. Initial transients are excluded from the Fourier analysis.

an equilibrium configuration, so radial excitations in each field are quickly induced.

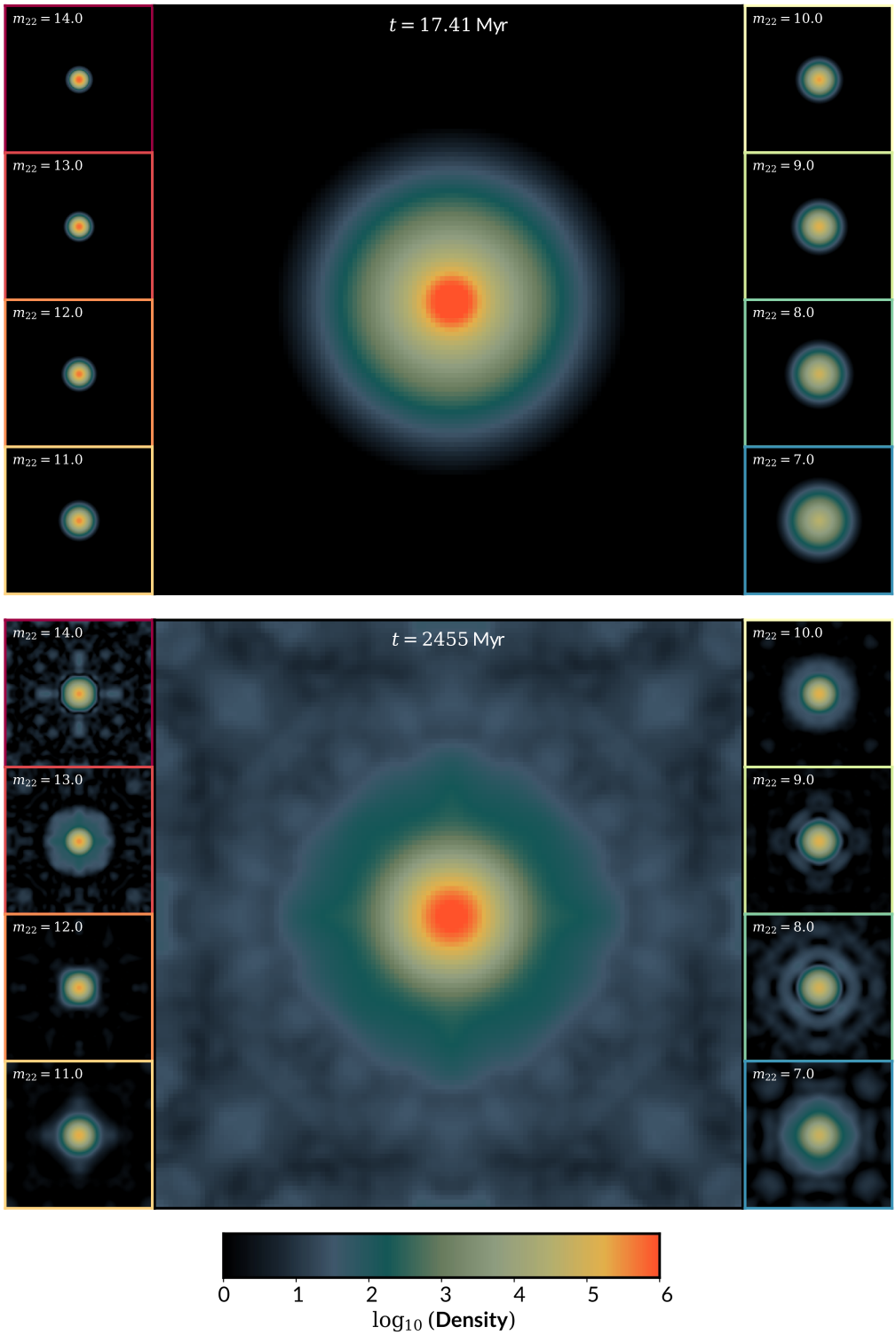

Figure 6.3: Aggregate density slices of the 8-field simulation at two points in time, with the densities of each field shown in the smaller boxes

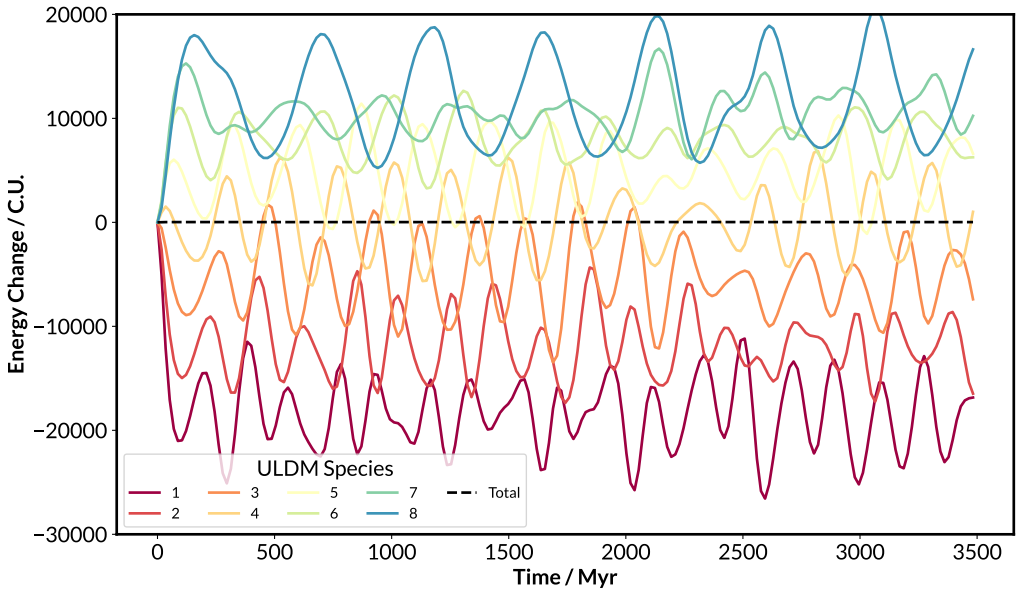

Figure 6.4: Component energy changes over time in the 8-field setup

6.3 Halos: Same Mass

We can generate multifield halos directly by adapting the eigenmode method described in Section 4.3.6 in which the initial configuration is constructed by decomposing the halo density profile into radial eigenfunctions and multiplying each of them with a random phase. We extend this to the multifield case by using the same radial eigenfunctions for the density but a different set of random phases for each field.

We assume that each field has a central soliton and a surrounding NFW halo with a combined density profile

$$\rho(r) = \begin{cases} \rho_{\text{Sol}}(r) & \text{if } \rho_{\text{Sol}} > \rho_{\text{NFW}} \\ \rho_{\text{NFW}}(r)\; e^{[-(r/r_{\text{vir}})^2/2]} & \text{otherwise.} \end{cases} \tag{6.1}$$

The extra exponential term suppresses the density outside the virial radius r_{vir} to minimise interactions at the periodic boundaries of the box. According to convention, we define the virial radius as the radius at which the

average density in the enclosed sphere is 200 times the critical density of the Universe, which also sets the virial mass within this region, $M_{\rm vir}$.

For a single field, the standard central soliton is the same as in Chapter 4. We use the virial halo mass $M_{\rm vir}$ to determine the core radius $r_{\rm c}$ of the soliton applying the core-halo relation introduced in [28],

$$r_{\rm c} = 1.6 \times \frac{1}{m_{22}} \left(\frac{M_{\rm vir}}{10^9 M_\odot} \right)^{-1/3} \mathrm{kpc}. \tag{6.2}$$

This relation has become contested in recent times, but we assume that it is a sensible estimate of core size in this initial investigation. Finally, we are free to choose the NFW scale radius between r_c and the virial radius and this choice does not significantly affect the dynamics of the halo.

For the sake of definiteness, we choose the dwarf galaxy Eridanus II as a template for the halo as it has been widely used to test ULDM. Eridanus II has a half-light radius $r_{1/2} = 300\,\mathrm{pc}$ [86] and half-light mass $M_{1/2} = 1.2 \times 10^7\, M_\odot$ [87]. According to Ref. [88], the half-light radius and the virial radius are related by $r_{1/2} \simeq 0.015\, r_{\rm vir}$, corresponding to $r_{\rm vir} = 20\,\mathrm{kpc}$ and $M_{\rm vir} = 4\pi/3 \times 200\, \bar{\rho}\, r_{\rm vir}^3 \simeq 3 \times 10^8\, M_\odot$. This results in the core radius $r_c \simeq 0.5$ kpc and we choose $r_s = 2\,\mathrm{kpc}$ for the scale radius.

We performed simulations with ULDM mass $m_{22} = 5$ and one, two, and four ULDM fields. Each field in the multifield simulations is initialised with the same radial eigenfunctions, but different random phases. The granules of the different fields are thus initially uncorrelated. We evolve this system through $\mathcal{O}(30)$ oscillation periods, or roughly 5 Gyr. Transients associated with the relaxation of the initial state roughly decay over the first three oscillations.

The ULDM densities in the plane $z = 0$ at $t = 1.6$ Gyr are shown in Figure 6.5. As the number of fields increases, the solitonic core retains its shape

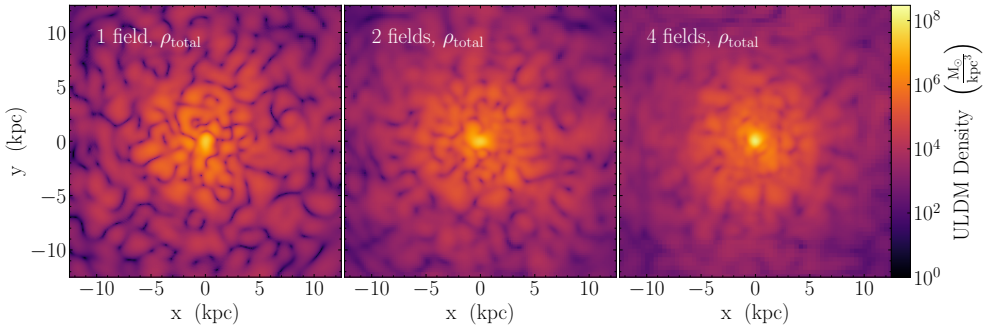

Figure 6.5: Total density around the centre of the halo for the simulations involving one field, two fields, and four fields. The total density becomes progressively smoother as the number of fields increases.

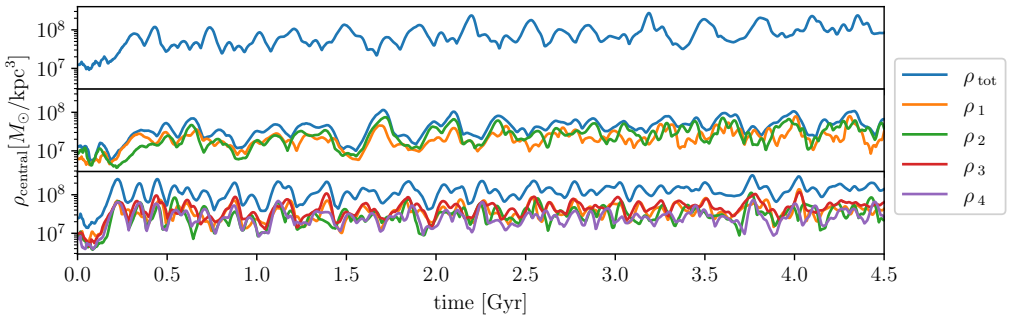

Figure 6.6: The density in the centre of the soliton for the simulations with only one field (top), two fields (middle), and four fields (bottom). We show densities of individual constituents ρ_i, as well as the total density $\rho_{\rm tot}$.

because there is a central overdensity in each of the constituent fields. At the same time, the granular overdensities in the surrounding halo are visibly smoothed out.

Figure 6.6 shows the evolution of the central density of the solitons over time. In all cases we see oscillations in the solitonic core [89, 83], along with an initial transient. In the multifield scenarios, the central oscillations in constituent fields become synchronised. This is presumably enabled by their mutual gravitational coupling.

The two-point correlation function for the equal-mass simulations is shown in Figure 6.7. It is calculated at an arbitrary time during the simu-

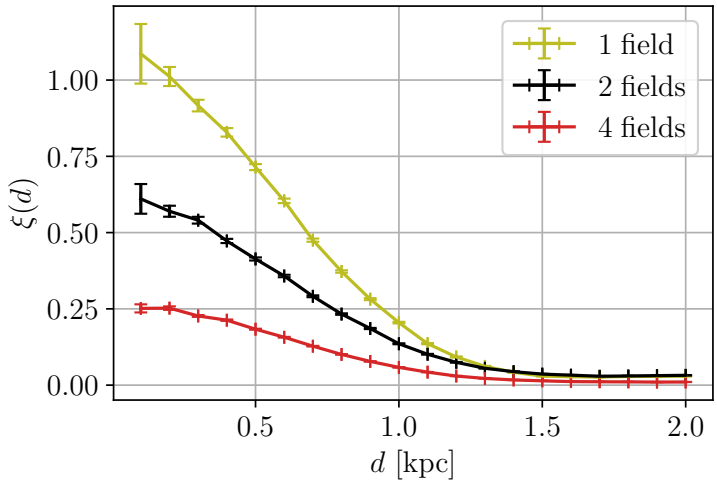

Figure 6.7: Two-point correlation function of the total overdensity for the three equal-mass simulations at an arbitrary time. We see that $\xi \sim 1/N$ and that the fields are fully uncorrelated at scales much larger than the de Broglie length.

lations. The value of $\xi(r)$ is close to zero for scales much larger than the de Broglie wavelength. Critically, $\xi(r)$ demonstrates a $1/N$ dependence, from which we can infer that the amplitude of the overdensity decreases in proportion to $\sqrt{N}$, i.e. in the multifield case $\delta(x) \to \delta(x)/\sqrt{N}$.

This scaling is also consistent with simulations of vector dark matter [90] which, without no self-interactions, has three independent components and interference is suppressed by $1/\sqrt{3}$, relative to the standard ULDM model.

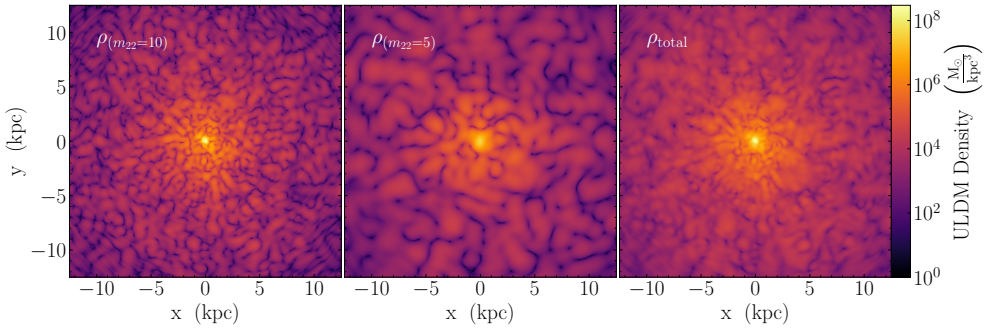

Figure 6.8: Densities of the two constituent fields in the two-field multi-mass scenario ($m_{22} = 10$ left and $m_{22} = 5$ center), as well as the total density (right).

6.4 Halos: Different Mass

We lastly examine a two-field scenario with $m_{22} = 10$ and $m_{22} = 5$. Figure 6.8 shows the density for both constituent fields and the total density at a representative time. The different de Broglie wavelengths of the fields are clearly visible and the combined density is again qualitatively smoother than either of the individual fields. This verifies that the suppression of small-scale structure seen in the equal-mass case carries over to the multi-mass scenario.

Clearly, such trends would break down in the limit of an extreme mass ratio – if one field has a de Broglie wavelength much larger than the others, it constitutes a smooth background relative to the structure present in the more massive fields. However, for mass differences of $\mathcal{O}(1)$, the qualitative dynamics do not appear to depend on whether we have strictly equal or merely similar masses.

Small moves, Ellie. Small moves.

Carl Sagan, *Contact*

7

Future Investigations

In this chapter, we sketch several lines of enquiry that are opened up by the numerical tools developed in this thesis, and provide avenues for future investigations.

7.1 Simulations with Dynamic Black Hole Mass

We saw in Chapter 3 how to estimate the accretion rate of axions by a black hole, and $\mathrm{PyUltraLight}$ has been built such that the particle mass (alongside its smoothing parameter r_P, for that matter) can change over time. The other end of the equation needs more attention – how should

the ULDM ψ react to the accretion process and lose the commensurate amount of amplitude / mass as accretion takes place?

Similar to the one used to enforce the dispersive sponge boundary condition, an imaginary potential term seems to be the answer. Chapter 5 of Ref. [67] employs an imaginary Gaussian potential to remove mass from a soliton in $\mathrm{PyUltraRound}$. There, assuming spherical symmetry and neglecting higher-order ULDM self-interaction, the equations of motion are

$$i\dot{\Psi}(r,t) = -\frac{1}{2}\frac{\partial^2\Psi(r,t)}{\partial r^2} + \left(\frac{V}{r} - \frac{M_{\mathsf{BH}}}{r} - iA\exp\left(-\frac{r^2}{2w^2}\right)\right)\Psi(r,t) \tag{7.1a}$$

$$\frac{\partial^2 V(r,t)}{\partial r^2} = 4\pi\frac{|\Psi(r,t)|^2}{r}, \tag{7.1b}$$

where we have introduced the variables $\Psi = r\psi$ and $V = r\Phi$, and the parameters A and w characterise the amplitude and width of the Gaussian, respectively. The ULDM density has a rate of change

$$\dot{\rho} = \frac{i}{2}\left(\Psi^*\frac{\partial^2\Psi}{\partial r^2} - \Psi\frac{\partial^2\Psi^*}{\partial r^2}\right) - 2A\exp\left(-\frac{r^2}{2w^2}\right)\rho. \tag{7.2}$$

Integrated over all space, we have the rate of mass loss,

$$\dot{M}_{\mathsf{ULDM}} = -8\pi A\int_0^\infty \mathrm{d}r\exp\left(\frac{-r^2}{2w^2}\right)\rho(r)r^2. \tag{7.3}$$

The main difficulty in the implementation of a 3D version of the framework above is again interpolation – as the particle moves between grid points, how can we make the imaginary potential fairly "felt" by ULDM data? Making the peak too narrow will lead to an underestimation of $\dot{\rho}$ due to sampling error, and making the peak too wide will compromise the assumption that accretion happens locally, at scales far smaller than the simulation grids. More testing is required to make this physically consistent. In general more research is required in establishing a viable parameter space over which black hole accretion is interesting and relevant.

7.2 Better Understanding Soliton-BH Systems

Recent work [91] explores the radial dynamical friction of a black hole around a ULDM soliton. It extends the content first shown in Section 5.7 and analyses the motion of a particle as it plunges radially through a soliton. A semi-analytic treatment of dynamical friction (and stone skipping modes) in this context is also being developed.

The eigenmode decomposition method discussed earlier requires a spherically symmetric potential whose centre coincides with the centre of mass of the soliton. When a black hole orbits the soliton in a near-circular orbit, however, it provides an external potential that is neither symmetric nor static, and this strains our assumptions in the current framework.

The problem is less severe when the point mass starts near the centre of the soliton, where orbital periods are short and the average position over long durations seem to smear out this misalignment. More work needs to be done to make this a robust tool for analysis.

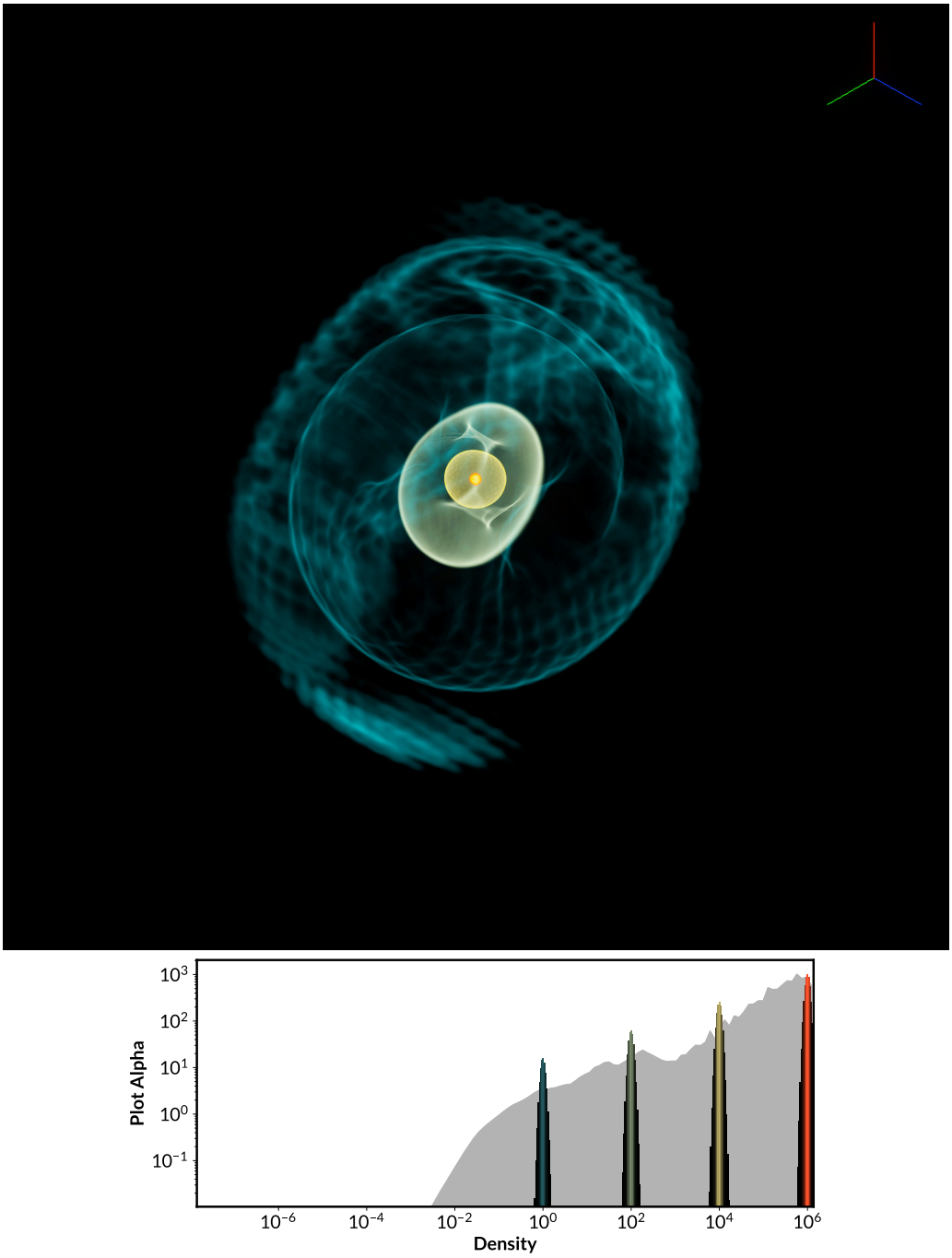

Figure 7.1: 3D render of a ULDM soliton after a massive particle has stirred it up, alongside the colour transfer function, which makes certain density values appear opaque.

7.3 ULDM, CDM, Baryons

Consider a two-field dark matter scenario where one kind of the constituent particles is massive and well-described by the standard collisionless CDM framework, while the other exhibits wave-like behaviour governed by the Schrödinger-Poisson equation. Furthermore, as Chapter 3 has been building up, we are also interested in the roles that baryonic matter plays in the cosmic structure history. This means that simulations with dark matter and baryonic matter combined will be the central focus of our future ULDM investigations.

$\mathrm{AxioNyx}$ was originally released with the capacity to simulate mixed FDM-CDM systems, and we have restored the ability (described in the original Nyx code) to simulate rudimentary baryonic physics, so a logical step is to simulate all three at once, and explore new parameter spaces such as the CDM/FDM ratio against more realistic models of galactic halos.

Our first effort is the investigation of the spherical collapse of a mixed Baryon-ULDM system. The initial conditions we picked for the first test run are comparable to the choice of Kendall et al. [92], which looked at pure ULDM halos, except we keep the initial overdensity spherical. It follows a Gaussian,

$$\rho_0(\mathbf{x}) = \rho_0 \left(1 + \delta \exp\left(-\frac{r^2}{r_{\mathsf{Ch}}^2}\right)\right), \tag{7.4}$$

where ρ_0 is the background density, δ is the amplitude of the overdensity, and r_{Ch} is a character radius of the overdensity.

H_0 is set to 0, and so cosmic expansion is turned off. There are two parameters controlling the behaviour of the baryonic matter, which we assume to be purely hydrogen, γ, and f_B, the fraction of baryon density in the initial

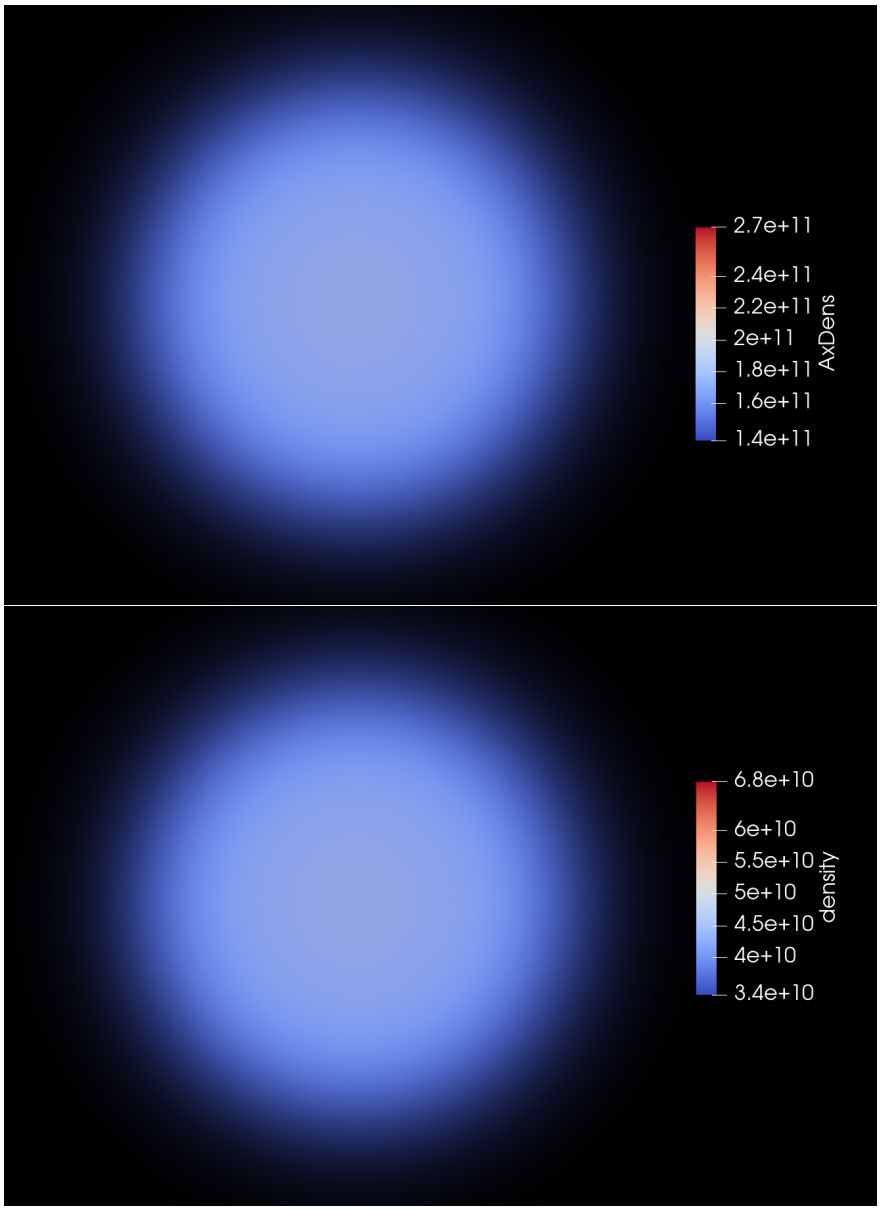

Figure 7.2: 3D visualisations of baryon and axion densities in the initial AxioNyx simulation grid.

overdense clump. The initial condition for such a run is sketched in Figure 7.2, where $\rho_{\text{ULDM}}/\rho_{\text{Baryon}} = 4$.

For the first simulation, we have plotted the spherically averaged densities for ULDM and baryons in Figure 7.3. As time passes, we see that the central densities of both ULDM and baryons increase dramatically, which

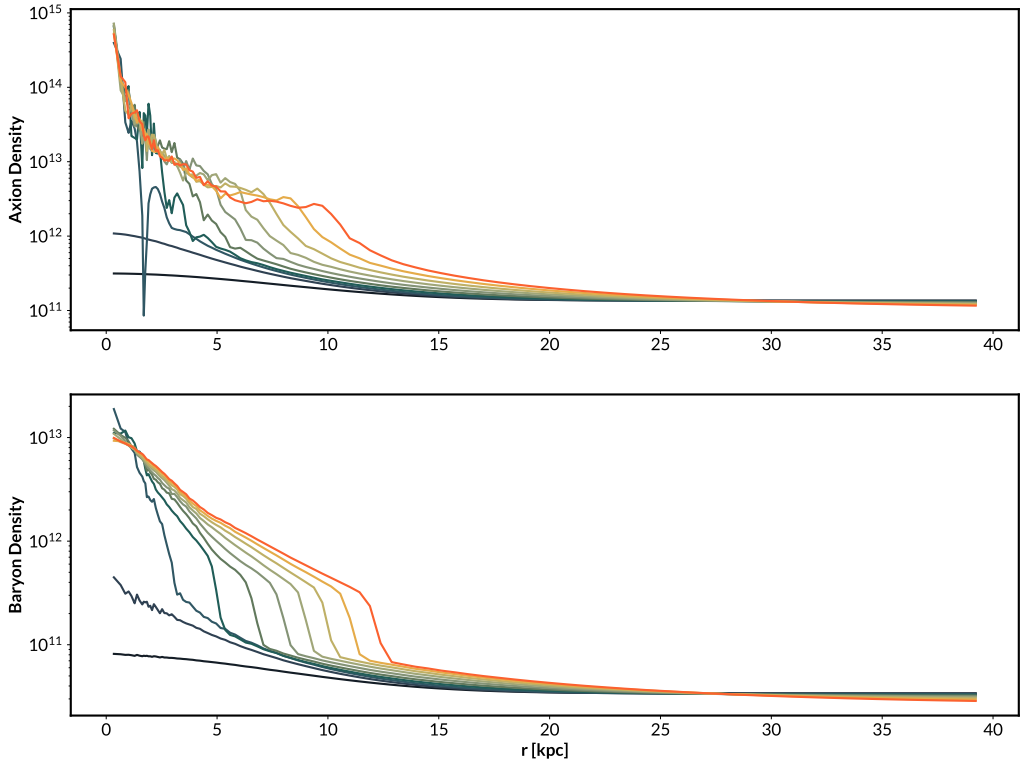

Figure 7.3: Radial density over time. Time runs from green to orange.

triggers higher and higher refinement levels within AxioNyx . The central density of the baryons quickly peak and a wave pushes materials outwards. This is reflected in the shape of the ULDM distribution as well, which now features a more pronounced “shoulder” as well as a sharper central peak than the standard ULDM soliton.

This is an compelling beginning to cosmological simulations that enrich the phenomenology of ULDM behaviour in dramatically more realistic galactic environments.

That the powerful play goes on, and you may contribute a verse.

Walt Whitman, *O Me! O Life!*

8

Summary

Ultralight dark matter consists a class of hypothetical particles that exist as quantum condensates in the current universe, governed by the Schrödinger-Poisson equations. ULDM has gained significant interest thanks to their elegance and ability to explain several apparent observational challenges to the standard ΛCDM cosmological model.

Extensions to and constraints on the ULDM model usually involve the mass of the ultralight axion (m_{A}), the strength of the non-gravitational self-interaction (if any), and the possibility that more than one axion fields exist that all interact gravitationally with each other.

The presence of ULDM in galactic halos can be roughly divided into two regions, the "core", which resembles a Schrödinger-Poisson soliton and is

roughly static between its self gravity and "quantum pressure", and the "skirt", which exhibits constant density fluctuations and wavelike interference effects on the order of the particles' de Broglie wavelengths.

In this thesis, we have presented the numerical methodology behind effective simulations of ULDM in astrophysical contexts through the extensively modified programs $\mathrm{PyUltraLight}$ and $\mathrm{AxioNyx}$. We also outlined some ways such simulations can interface with astrophysical systems that are more feasible to observe and test.

Chapter 5 reported simulations of the interaction between a compact object (black hole or globular cluster) with a distribution of ULDM. We focused on the lowest-order model where a massive particle (or tightly packed star cluster) orbited a ground state soliton in initially circular orbits. For the case of one particle orbiting the soliton, "stone-skipping" modes were one of the features identified, where under some conditions the orbital decay of the massive particle is impeded early on, and the rate of its inward migration is outstandingly low. This has prompted us to look into the language of eigenstates to model this system, given that such a mode may be evidence that the orbital motion and certain excitation modes are in resonance.

Chapter 6 was based on our next paper, which looked at the multi-field ULDM model. We looked into the qualitative behaviours of solitons and halos in various multifield setups, and, by comparing them with single-field counterparts, shed light on the possibility that multifield ULDM can relieve some tensions in the bounds on m_{A}, and provide a better fit with astrophysical observations.

One other integral aspect of this thesis is the pioneering of simulations that incorporate both ULDM and gas (baryonic) physics. The inclusion of

baryons, given their pivotal role in Cosmic history and the complexity they introduce across the scales, represents a significant advancement. This thesis marks a critical first step in this direction, showcasing the initial results from the AxioNyx runs in Section 7.3. These early runs lay a strong foundation for future research.

Bibliography

[1] Daniel Baumann. *Cosmology: Cambridge Part III Mathematical Tripos*. 2018.

[2] Steven Weinberg. *Cosmology*. 2008. isbn: 978-0-19-852682-7.

[3] Edward Harrison. *Cosmology: The Science of the Universe*. 2000. isbn: 978-0521661485.

[4] Dragan Huterer. *A Course in Cosmology: From Theory to Practice*. Cambridge University Press, 2023.

[5] A. A. Penzias and R. W. Wilson. "A Measurement of Excess Antenna Temperature at 4080 Mc/s." In: *ApJ* 142 (July 1965), pp. 419–421. doi: 10.1086/148307.

[6] N. Aghanim et al. "Planck 2018 results: VI. Cosmological parameters". In: *Astronomy and Astrophysics* 641 (Sept. 2020), A6. issn: 1432-0746. doi: 10.1051/0004-6361/201833910. url: http://dx.doi.org/10.1051/0004-6361/201833910.

[7] Edvige Corbelli and Paolo Salucci. “The extended rotation curve and the dark matter halo of M33”. In: *MNRAS* 311.2 (Jan. 2000), pp. 441–447. doi: 10.1046/j.1365-8711.2000.03075.x. arXiv: astro-ph/9909252 [astro-ph].

[8] W. Tucker et al. “1E 0657-56: A Contender for the Hottest Known Cluster of Galaxies”. In: *ApJ Letters* 496.1 (Mar. 1998), pp. L5–L8. doi: 10.1086/311234. arXiv: astro-ph/9801120 [astro-ph].

[9] Douglas Clowe, Anthony Gonzalez, and Maxim Markevitch. “Weak-Lensing Mass Reconstruction of the Interacting Cluster 1E 0657-558: Direct Evidence for the Existence of Dark Matter”. In: *ApJ* 604.2 (Apr. 2004), pp. 596–603. doi: 10.1086/381970. arXiv: astro-ph/0312273 [astro-ph].

[10] Max Tegmark et al. “Cosmological parameters from SDSS and WMAP”. In: *Phys. Rev. D* 69 (10 May 2004), p. 103501. doi: 10.1103/PhysRevD.69.103501. url: https://link.aps.org/doi/10.1103/PhysRevD.69.103501.

[11] Gianfranco Bertone and Tim M. P. Tait. “A new era in the search for dark matter”. In: *Nature* 562.7725 (2018), pp. 51–56. doi: 10.1038/s41586-018-0542-z. url: https://doi.org/10.1038/s41586-018-0542-z.

[12] E. Komatsu et al. “Five-Year Wilkinson Microwave Anisotropy Probe Observations: Cosmological Interpretation”. In: *ApJ Supplements* 180.2 (Feb. 2009), pp. 330–376. doi: 10.1088/0067-0049/180/2/330. arXiv: 0803.0547 [astro-ph].

[13] Beth A. Reid et al. “Cosmological constraints from the clustering of the Sloan Digital Sky Survey DR7 luminous red galaxies”. In: *MNRAS* 404.1 (May 2010), pp. 60–85. doi: 10.1111/j.1365-2966.2010.16276.x. arXiv: 0907.1659 [astro-ph.CO].

[14] Lars Hernquist et al. “The Lyman-Alpha Forest in the Cold Dark Matter Model”. In: *ApJ Letters* 457 (Feb. 1996), p. L51. doi: 10.1086/309899. arXiv: astro-ph/9509105 [astro-ph].

[15] Michael Kopp, Kyriakos Vattis, and Constantinos Skordis. “Solving the Vlasov equation in two spatial dimensions with the Schrödinger method”. In: *Phys. Rev. D* 96 (12 Dec. 2017), p. 123532. doi: 10.1103/PhysRevD.96.123532. url: https://link.aps.org/doi/10.1103/PhysRevD.96.123532.

[16] Julio F. Navarro, Carlos S. Frenk, and Simon D. M. White. “The Structure of Cold Dark Matter Halos”. In: *ApJ* 462 (May 1996), p. 563. doi: 10.1086/177173. arXiv: astro-ph/9508025 [astro-ph].

[17] Ricardo A. Flores and Joel R. Primack. “Observational and Theoretical Constraints on Singular Dark Matter Halos”. In: *ApJ Letters* 427 (May 1994), p. L1. doi: 10.1086/187350. arXiv: astro-ph/9402004 [astro-ph].

[18] Rohan P. Naidu et al. “Two Remarkably Luminous Galaxy Candidates at z $\approx$ 10-12 Revealed by JWST”. In: *ApJ Letters* 940.1, L14 (Nov. 2022), p. L14. doi: 10.3847/2041-8213/ac9b22. arXiv: 2207.09434 [astro-ph.GA].

[19] Mark Vogelsberger et al. “Cosmological simulations of galaxy formation”. In: *Nature Reviews Physics* 2.1 (Jan. 2020), pp. 42–66. doi: 10.1038/s42254-019-0127-2. arXiv: 1909.07976 [astro-ph.GA].

[20] Daniel Grin, David J. E. Marsh, and Renee Hlozek. *axionCAMB: Modification of the CAMB Boltzmann code*. Astrophysics Source Code Library, record ascl:2203.026. Mar. 2022. ascl: 2203.026.

[21] David J. E. Marsh and Ana-Roxana Pop. "Axion dark matter, solitons and the cusp-core problem". In: *M. Not. RAS* 451.3 (Aug. 2015), pp. 2479–2492. doi: 10.1093/mnras/stv1050. arXiv: 1502.03456 [astro-ph.CO].

[22] D. J. E. Marsh. "Axion cosmology". In: *Physics Reports* 643 (July 2016), pp. 1–79. doi: 10.1016/j.physrep.2016.06.005.

[23] Roberto D. Peccei. "The Strong CP Problem and Axions". In: *Axions*. Springer Berlin Heidelberg, 2008, pp. 3–17. isbn: 9783540735182. doi: 10.1007/978-3-540-73518-2_1. url: http://dx.doi.org/10.1007/978-3-540-73518-2_1.

[24] Thomas Mannel. "Theory and phenomenology of CP violation". In: *Nucl. Phys. B Proc. Suppl.* 167 (2007). Ed. by Guennadi Borisov et al., pp. 115–119. doi: 10.1016/j.nuclphysbps.2006.12.083.

[25] Lawrence M. Widrow and Nick Kaiser. "Using the Schroedinger Equation to Simulate Collisionless Matter". In: *ApJ* 416 (Oct. 1993), p. L71. issn: 0004-637X. doi: 10.1086/187073. url: http://adsabs.harvard.edu/doi/10.1086/187073.

[26] Alex Gough and Cora Uhlemann. "Making (dark matter) waves: Untangling wave interference for multi-streaming dark matter". In: *The Open Journal of Astrophysics* 5 (Sept. 8, 2022). doi: 10.21105/astro.2206.11918.

[27] Elisa G. M. Ferreira. "Ultra-Light Dark Matter". In: (2020). arXiv: 2005.03254. url: http://arxiv.org/abs/2005.03254.

[28] H.-Y. Schive, T. Chiueh, and T. Broadhurst. “Cosmic structure as the quantum interference of a coherent dark wave”. In: *Nature Physics* 10 (July 2014), pp. 496–499. doi: 10.1038/nphys2996. arXiv: 1406.6586.

[29] J. Luna Zagorac et al. “Schrodinger-Poisson solitons: Perturbation theory”. In: *Phys. Rev. D* 105 (10 May 2022), p. 103506. doi: 10.1103/PhysRevD.105.103506. url: https://link.aps.org/doi/10.1103/PhysRevD.105.103506.

[30] Hsi-Yu Schive, Tzihong Chiueh, and Tom Broadhurst. “Soliton Random Walk and the Cluster-Stripping Problem in Ultralight Dark Matter”. In: *Phys. Rev. Lett.* 124.20 (Dec. 2019), pp. 1–6. issn: 10797114. doi: 10.1103/PhysRevLett.124.201301. arXiv: 1912.09483. url: http://arxiv.org/abs/1912.09483%20http://dx.doi.org/10.1103/PhysRevLett.124.201301.

[31] J. Luna Zagorac et al. “Soliton formation and the core-halo mass relation: An eigenstate perspective”. In: *Phys. Rev. D* 107 (8 Apr. 2023), p. 083513. doi: 10.1103/PhysRevD.107.083513. url: https://link.aps.org/doi/10.1103/PhysRevD.107.083513.

[32] Mateja Gosenca et al. “Multifield ultralight dark matter”. In: *Phys. Rev. D* 107 (8 Apr. 2023), p. 083014. doi: 10.1103/PhysRevD.107.083014. url: https://link.aps.org/doi/10.1103/PhysRevD.107.083014.

[33] Tim Koorey. “Stone-Skipping Orbital Dynamics in Schrodinger-Poisson Solitons”. MA thesis. University of Auckland, 2023.

[34] Nathan Musoke, Shaun Hotchkiss, and Richard Easther. “Lighting the Dark: Evolution of the Postinflationary Universe”. In: *Phys. Rev. Lett.* 124.6 (2020), p. 061301. doi: 10.1103/PhysRevLett.124.061301. arXiv: 1909.11678 [astro-ph.CO].

[35] Jens C. Niemeyer and Richard Easther. “Inflaton Clusters and Inflaton Stars”. In: (Nov. 2019). arXiv: 1911.01661 [astro-ph.CO].

[36] Benedikt Eggemeier, Jens C. Niemeyer, and Richard Easther. “Formation of inflaton halos after inflation”. In: *Phys. Rev. D* 103.6 (2021), p. 063525. doi: 10.1103/PhysRevD.103.063525. arXiv: 2011.13333 [astro-ph.CO].

[37] S. Dimopoulos et al. “N-flation”. In: *JCAP* 08 (2008), p. 003. doi: 10.1088/1475-7516/2008/08/003. arXiv: hep-th/0507205.

[38] Richard Easther and Liam McAllister. “Random matrices and the spectrum of N-flation”. In: *JCAP* 05 (2006), p. 018. doi: 10.1088/1475-7516/2006/05/018. arXiv: hep-th/0512102.

[39] Mafalda Dias, Jonathan Frazer, and David Seery. “Computing observables in curved multifield models of inflation - A guide (with code) to the transport method”. In: *JCAP* 12 (2015), p. 030. doi: 10.1088/1475-7516/2015/12/030. arXiv: 1502.03125 [astro-ph.CO].

[40] S. Chandrasekhar. “Dynamical Friction. I. General Considerations: the Coefficient of Dynamical Friction.” In: *ApJ* 97 (Mar. 1943), p. 255. doi: 10.1086/144517.

[41] L. D. Landau and E. M. Lifshitz. *Course of theoretical physics III: Quantum mechanics, Non-relativistic theory (3rd ed.)* 1977.

[42] J. A. Krommes. “An introduction to the physics of the Coulomb logarithm, with emphasis on quantum-mechanical effects”. In: *Journal of Plasma Physics* 85.1 (2019), p. 925850101. doi: 10.1017/S0022377818001319.

[43] Yi Xie. “Dynamical friction of pulsars in globular clusters”. In: *Astrophysics and Space Science* 368.6 (2023), p. 51. doi: 10.1007/s10509-023-04208-z. url: https://doi.org/10.1007/s10509-023-04208-z.

[44] Paolo Pani. “Binary pulsars as dark-matter probes”. In: *Phys. Rev. D* 92 (12 Dec. 2015), p. 123530. doi: 10.1103/PhysRevD.92.123530. url: https://link.aps.org/doi/10.1103/PhysRevD.92.123530.

[45] Lachlan Lancaster et al. “Dynamical Friction in a Fuzzy Dark Matter Universe”. In: (Sept. 2019). doi: 10.1088/1475-7516/2020/01/001. arXiv: 1909.06381. url: http://arxiv.org/abs/1909.06381%20http://dx.doi.org/10.1088/1475-7516/2020/01/001.

[46] D. Lynden-Bell. “Galactic Nuclei as Collapsed Old Quasars”. In: *Nature* 223.5207 (1969), pp. 690–694. doi: 10.1038/223690a0. url: https://doi.org/10.1038/223690a0.

[47] W. G. Unruh. “Absorption cross section of small black holes”. In: *Phys. Rev. D* 14 (12 Dec. 1976), pp. 3251–3259. doi: 10.1103/PhysRevD.14.3251. url: https://link.aps.org/doi/10.1103/PhysRevD.14.3251.

[48] Katy Clough, Pedro G. Ferreira, and Macarena Lagos. “Growth of massive scalar hair around a Schwarzschild black hole”. In: *Phys. Rev. D* 100 (6 Sept. 2019), p. 063014. doi: 10.1103/PhysRevD.100.063014. url: https://link.aps.org/doi/10.1103/PhysRevD.100.063014.

[49] Lam Hui et al. “Black hole hair from scalar dark matter”. In: *Journal of Cosmology and Astroparticle Physics* 2019.6, 038 (June 2019), p. 038. doi: 10.1088/1475-7516/2019/06/038. arXiv: 1904.12803 [gr-qc].

[50] Jamie Bamber et al. “Growth of accretion driven scalar hair around Kerr black holes”. In: *Phys. Rev. D* 103.4 (2021), p. 044059. doi: 10.1103/PhysRevD.103.044059. arXiv: 2011.07870 [gr-qc].

[51] Lam Hui. “Wave Dark Matter”. In: *Annual Review of Astronomy and Astrophysics* 59.1 (2021), pp. 247–289. doi: 10.1146/annurev-astro-120920-010024. eprint: https://doi.org/10.1146/annurev-astro-120920-010024. url: https://doi.org/10.1146/annurev-astro-120920-010024.

[52] Ana A Avilez et al. “On the possibility that ultra-light boson haloes host and form supermassive black holes”. In: *MNRAS* 477.3 (Mar. 2018), pp. 3257–3272. doi: 10.1093/mnras/sty572. eprint: https://academic.oup.com/mnras/article-pdf/477/3/3257/24802679/sty572.pdf. url: https://doi.org/10.1093/mnras/sty572.

[53] Ya. B. Zel’Dovich. “Generation of Waves by a Rotating Body”. In: *Soviet Journal of Experimental and Theoretical Physics Letters* 14 (Aug. 1971), p. 180.

[54] Matthew J. Stott and David J. E. Marsh. “Black hole spin constraints on the mass spectrum and number of axionlike fields”. In: *Phys. Rev. D* 98 (8 Oct. 2018), p. 083006. doi: 10.1103/PhysRevD.98.083006. url: https://link.aps.org/doi/10.1103/PhysRevD.98.083006.

[55] Matt Visser. *The Kerr spacetime: A brief introduction*. 2008. arXiv: 0706.0622 [gr-qc].

[56] Giuseppe Ficarra, Paolo Pani, and Helvi Witek. “Impact of multiple modes on the black-hole superradiant instability”. In: *Phys. Rev. D* 99 (10 May 2019), p. 104019. doi: 10.1103/PhysRevD.99.104019. url: https://link.aps.org/doi/10.1103/PhysRevD.99.104019.

[57] Lam Hui et al. “Ultralight scalars as cosmological dark matter”. In: *Phys. Rev. D* 95.4 (2017). issn: 24700029. doi: 10.1103/PhysRevD.95.043541. arXiv: 1610.08297.

[58] Ben Bar-Or, Jean Baptiste Fouvry, and Scott Tremaine. “Relaxation in a fuzzy dark matter halo”. In: *arXiv* (2018). issn: 23318422. doi: 10.3847/1538-4357/aaf28c. arXiv: 1809.07673.

[59] Ann S. Almgren et al. “Nyx: A MASSIVELY PARALLEL AMR CODE FOR COMPUTATIONAL COSMOLOGY”. In: *ApJ* 765.1 (Feb. 2013), p. 39. doi: 10.1088/0004-637X/765/1/39. url: https://dx.doi.org/10.1088/0004-637X/765/1/39.

[60] Faber Edwards et al. “PyUltraLight: A pseudo-spectral solver for ultralight dark matter dynamics”. In: *J. Cosmol. Astropart. Phys.* 2018.10 (2018). issn: 14757516. doi: 10.1088/1475-7516/2018/10/027. arXiv: 1807.04037.

[61] Bodo Schwabe et al. “AxioNyx: Simulating Mixed Fuzzy and Cold Dark Matter”. In: (July 2020), pp. 1–10. arXiv: 2007.08256. url: http://arxiv.org/abs/2007.08256.

[62] Volker Springel, Naoki Yoshida, and Simon D. M. White. “GADGET: a code for collisionless and gasdynamical cosmological simulations”. In: *New Astronomy* 6.2 (Apr. 2001), pp. 79–117. doi: 10.1016/S1384-1076(01)00042-2. arXiv: astro-ph/0003162 [astro-ph].

[63] Greg L. Bryan et al. “ENZO: An Adaptive Mesh Refinement Code for Astrophysics”. In: *ApJ: Supplement* 211.2, 19 (Apr. 2014), p. 19. doi: 10.1088/0067-0049/211/2/19. arXiv: 1307.2265 [astro-ph.IM].

[64] R. Courant, K. Friedrichs, and H. Lewy. “Über die partiellen Differenzengleichungen der mathematischen Physik”. In: *Mathematische Annalen* 100.1 (Dec. 1928), pp. 32–74. doi: 10.1007/BF01448839. url: http://dx.doi.org/10.1007/BF01448839.

[65] Roger W. Hockney. “The potential calculation and some applications”. In: 1970. url: https://api.semanticscholar.org/CorpusID:117901330.

[66] H. C. Plummer. “On the Problem of Distribution in Globular Star Clusters: (Plate 8.)” In: *Mon. Not. R. Astron. Soc.* 71.5 (Mar. 1911), pp. 460–470. issn: 0035-8711. doi: 10.1093/mnras/71.5.460. url: https://ui.adsabs.harvard.edu/abs/1911MNRAS..71..460P/abstract.

[67] Ningyuan Lillian Guo. “Ultralight Dark Matter Dynamics with an Absorbing Black Hole”. MA thesis. University of Auckland, 2020.

[68] Noah Glennon et al. “Scalar dark matter vortex stabilization with black holes”. In: *Journal of Cosmology and Astroparticle Physics* 2023.7, 004 (July 2023), p. 004. doi: 10.1088/1475-7516/2023/07/004. arXiv: 2301.13220 [astro-ph.CO].

[69] Yourong Wang and J. Luna Zagorac. “Stochastic Gravitational Waves Background from ultralight dark matter Halos”. In preparation. 2024.

[70] M. Schwarzschild. “A numerical model for a triaxial stellar system in dynamical equilibrium.” In: *ApJ* 232 (Aug. 1979), pp. 236–247. doi: 10.1086/157282.

[71] Tomer D. Yavetz, Xinyu Li, and Lam Hui. “Construction of wave dark matter halos: Numerical algorithm and analytical constraints”. In: *Phys. Rev. D* 105.2 (2022), p. 023512. doi: 10.1103/PhysRevD.105.023512. arXiv: 2109.06125 [astro-ph.CO].

[72] P. J. E. Peebles. *The large-scale structure of the universe*. 1980.

[73] Marsha J. Berger and Joseph Oliger. “Adaptive Mesh Refinement for Hyperbolic Partial Differential Equations”. In: *Journal of Computational Physics* 53.3 (Mar. 1984), pp. 484–512. doi: 10.1016/0021-9991(84)90073-1.

[74] Yourong Wang and Richard Easther. “Dynamical friction from ultralight dark matter”. In: *Phys. Rev. D* 105 (6 Mar. 2022), p. 063523. doi: 10.1103/PhysRevD.105.063523. url: https://link.aps.org/doi/10.1103/PhysRevD.105.063523.

[75] Hsi-Yu Schive et al. “Understanding the Core-Halo Relation of Quantum Wave Dark Matter from 3D Simulations”. In: *Phys. Rev. Lett.* 113 (26 Dec. 2014), p. 261302. doi: 10.1103/PhysRevLett.113.261302. url: https://link.aps.org/doi/10.1103/PhysRevLett.113.261302.

[76] Thomas Helfer et al. “Black hole formation from axion stars”. In: *Journal of Cosmology and Astroparticle Physics* 2017.03 (Mar. 2017), pp. 055–055. issn: 1475-7516. doi: 10.1088/1475-7516/2017/03/055. url: http://dx.doi.org/10.1088/1475-7516/2017/03/055.

[77] Keir K Rogers and Hiranya V Peiris. “Strong bound on canonical ultra-light axion dark matter from the Lyman-alpha forest”. In: (2020), pp. 1–9. arXiv: arXiv:2007.12705v2.

[78] Dhruba Dutta Chowdhury et al. “On the Random Motion of Nuclear Objects in a Fuzzy Dark Matter Halo”. In: *ApJ* 916.1 (July 2021), p. 27. issn: 1538-4357. doi: 10.3847/1538-4357/ac043f. url: http://dx.doi.org/10.3847/1538-4357/ac043f.

[79] Lorenzo Annulli, Vitor Cardoso, and Rodrigo Vicente. “Response of ultralight dark matter to supermassive black holes and binaries”. In: *Phys. Rev. D* 102.6 (2020), p. 063022. doi: 10.1103/PhysRevD.102.063022. arXiv: 2009.00012 [gr-qc].

[80] Sarah Burke-Spolaor et al. “The Astrophysics of Nanohertz Gravitational Waves”. In: *Astron. Astrophys. Rev.* 27.1 (2019), p. 5. doi: 10.1007/s00159-019-0115-7. arXiv: 1811.08826 [astro-ph.HE].

[81] Adeela Afzal et al. “The NANOGrav 15 yr Data Set: Search for Signals from New Physics”. In: *ApJ Letters* 951.1, L11 (July 2023), p. L11. doi: 10.3847/2041-8213/acdc91. arXiv: 2306.16219 [astro-ph.HE].

[82] Pau Amaro-Seoane et al. “Laser Interferometer Space Antenna”. In: (Feb. 2017). arXiv: 1702.00786 [astro-ph.IM].

[83] F. Siddhartha Guzmán and L. Arturo Ureña-López. “Evolution of the Schrödinger-Newton system for a self-gravitating scalar field”. In: *Phys. Rev. D* 69 (12 June 2004), p. 124033. doi: 10.1103/PhysRevD.69.124033. url: https://link.aps.org/doi/10.1103/PhysRevD.69.124033.

[84] Sverre J. Aarseth and William C. Saslaw. “Virial Mass Determinations of Bound and Unstable Groups of Galaxies.” In: *ApJ* 172 (Feb. 1972), p. 17. doi: 10.1086/151324.

[85] Xinyu Li, Lam Hui, and Tomer D. Yavetz. “Oscillations and random walk of the soliton core in a fuzzy dark matter halo”. In: *Phys. Rev. D* 103.2, 023508 (Jan. 2021), p. 023508. doi: 10.1103/PhysRevD.103.023508. arXiv: 2011.11416 [astro-ph.CO].

[86] D. Crnojević et al. “Deep Imaging of Eridanus II and Its Lone Star Cluster”. In: *ApJ Letters* 824.1, L14 (June 2016), p. L14. doi: 10.3847/2041-8205/824/1/L14. arXiv: 1604.08590 [astro-ph.GA].

[87] T. S. Li et al. “Farthest Neighbor: The Distant Milky Way Satellite Eridanus II”. In: *Astrophys. J.* 838.1 (2017), p. 8. doi: 10.3847/1538-4357/aa6113. arXiv: 1611.05052 [astro-ph.GA].

[88] Andrey V. Kravtsov. “The size - virial radius relation of galaxies”. In: *Astrophys. J. Lett.* 764 (2013), p. L31. doi: 10.1088/2041-8205/764/2/L31. arXiv: 1212.2980 [astro-ph.CO].

[89] J. Veltmaat, J. C. Niemeyer, and B. Schwabe. “Formation and structure of ultralight bosonic dark matter halos”. In: *Phys. Rev. D* 98.4 (Aug. 2018). doi: 10.1103/physrevd.98.043509.

[90] Mustafa A. Amin et al. “Small-scale structure in vector dark matter”. In: *JCAP* 08.08 (2022), p. 014. doi: 10.1088/1475-7516/2022/08/014. arXiv: 2203.11935 [astro-ph.CO].

[91] Russell Boey et al. “Dynamical friction and black holes in ultralight dark matter solitons”. In: *Phys. Rev. D* 109 (10 May 2024), p. 103526. doi: 10.1103/PhysRevD.109.103526. url: https://link.aps.org/doi/10.1103/PhysRevD.109.103526.

[92] Emily Kendall, Mateja Gosenca, and Richard Easther. “Aspherical ULDM collapse: variation in the core–halo mass relation”. In: *MNRAS* 526.1 (Sept. 2023), pp. 1046–1056. issn: 0035-8711. doi: 10.1093/mnras/stad2733. eprint: https://academic.oup.com/mnras/article-pdf/526/1/1046/51780312/stad2733.pdf. url: https://doi.org/10.1093/mnras/stad2733.